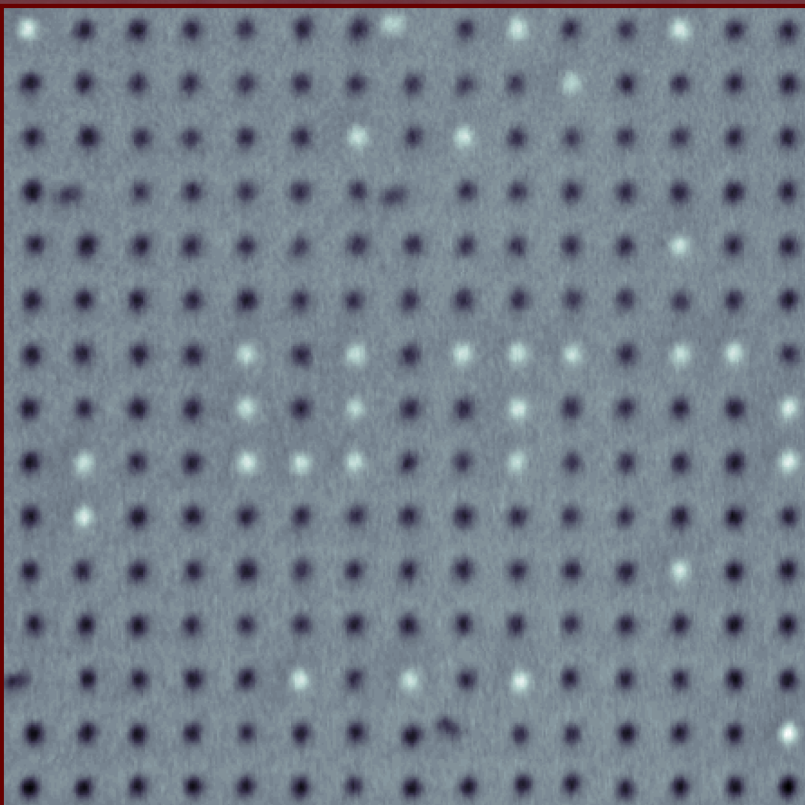


# Magnetic interactions in 2D and 3D arrays



Laurens Alink

**Graduation committee**

Prof. dr. P.M.G. Apers  
Prof. dr. ir. L. Abelmann  
Dr. ir. M.P. de Jong  
Prof. dr. Th.H.M. Rasing  
Prof. dr. T. Thomson  
Prof. dr. ir. H.J.W. Zandvliet

University of Twente (chairman and secretary)  
University of Twente (promotor)  
University of Twente  
Radboud University, the Netherlands  
The University of Manchester, United Kingdom  
University of Twente

**Paranymphs**

Joël Geerlings  
Kodai Hatakeyama



# UNIVERSITY OF TWENTE.

The research presented in this dissertation was carried out at the Transducers Science & Technology group at the MESA<sup>+</sup> Institute for Nanotechnology at the University of Twente, Enschede, the Netherlands. This research is supported by the Dutch Technology Foundation STW, which is part of the Netherlands Organisation for Scientific Research (NWO) and partly funded by the Ministry of Economic Affairs (project number 10540).

*Cover design inspired by Jeroen de Vries' dissertation. The nanoscale graffiti ("UT") was made by magnetic force microscope artist Martin Siekman. The self-assembly process of submillimeter-sized cubes has been photographed by silicon particle paparazzo Auke Been.*

Printed by Gildeprint, Enschede, the Netherlands  
Copyright © Laurens Alink, Enschede, the Netherlands, 2016.  
ISBN 978-90-365-4117-6  
DOI [10.3990/1.9789036541176](https://doi.org/10.3990/1.9789036541176)

# MAGNETIC INTERACTIONS IN 2D AND 3D ARRAYS

## DISSERTATION

to obtain  
the degree of doctor at the University of Twente,  
on the authority of the rector magnificus,  
prof. dr. H. Brinksma,  
on account of the decision of the graduation committee,  
to be publicly defended  
on Wednesday, 11 May 2016 at 12:45

by

**Laurens Alink**

born on 27 November 1982,  
in Hengelo (O), the Netherlands

This dissertation is approved by the promotor,

Prof. dr. ir. L. Abelmann University of Twente

# Contents

|  |           |
|--|-----------|
| <b>Contents</b>  | <b>i</b>  |
| <b>1 Introduction</b>  | <b>1</b>  |
| 1.1 Magnetostatic interactions . . . . .   | 1         |
| 1.1.1 Magnetostatic interactions in this thesis . . . . .                                  | 2         |
| 1.2 2D arrays of patterned magnetic islands . . . . .                                      | 2         |
| 1.2.1 Bit patterned media . . . . .  | 2         |
| 1.2.2 2D recording . . . . .   | 3         |
| 1.2.3 Alternative technologies . . . . .   | 4         |
| 1.3 Self-assembling arrays . . . . .   | 5         |
| 1.4 Outline of thesis . . . . .  | 6         |
| <b>2 Determination of bit patterned media noise based on island perimeter fluctuations</b> | <b>9</b>  |
| 2.1 Introduction . . . . .   | 9         |
| 2.2 Theory of shape fluctuation modeling . . . . .   | 10        |
| 2.3 Experimental method and simulation procedure . . . . .                                 | 13        |
| 2.3.1 Fabrication of patterned media . . . . .   | 13        |
| 2.3.2 SEM imaging . . . . .  | 14        |
| 2.3.3 Simulation of perimeters . . . . .   | 14        |
| 2.4 Results . . . . .  | 15        |
| 2.5 Discussion . . . . .   | 16        |
| 2.6 Conclusions . . . . .  | 17        |
| 2.7 Acknowledgment . . . . .   | 18        |
| <b>3 A simple two-dimensional coding scheme for bit patterned media</b>                    | <b>19</b> |
| 3.1 Introduction . . . . .   | 19        |
| 3.2 Theory: read back signal . . . . .   | 20        |
| 3.3 The simple coding scheme . . . . .   | 22        |
| 3.4 Simulation results and discussion . . . . .  | 23        |
| 3.5 Conclusions . . . . .  | 25        |
| 3.6 Acknowledgment . . . . .   | 26        |

|   |           |
|---|-----------|
| <b>4 Correct interpretation of tapping/liftmode MFM images of patterned magnetic islands by topography correction</b> | <b>27</b> |
| 4.1 Introduction . . . . .  | 27        |
| 4.2 Theory . . . . .  | 31        |
| 4.2.1 Magnetic force gradients . . . . .  | 31        |
| 4.2.2 Non-magnetic force gradients . . . . .  | 32        |
| 4.2.3 Liftmode correction theory . . . . .  | 35        |
| 4.2.4 Simulation of the liftmode correction . . . . .   | 37        |
| 4.3 Experimental . . . . .  | 42        |
| 4.3.1 Sample . . . . .  | 42        |
| 4.3.2 Magnetic force microscopy . . . . .   | 42        |
| 4.3.3 Preliminary corrections . . . . .   | 43        |
| 4.4 Results and discussion . . . . .  | 43        |
| 4.4.1 Non-magnetic forces . . . . .   | 43        |
| 4.4.2 Liftmode correction . . . . .   | 46        |
| 4.4.3 Discussion . . . . .  | 49        |
| 4.5 Conclusions . . . . .   | 50        |
| 4.6 Acknowledgment . . . . .  | 51        |
| <b>5 Angular dependence of the switching fields of individual Co/Pt islands in a patterned array</b>                  | <b>53</b> |
| 5.1 Introduction . . . . .  | 53        |
| 5.2 Theory . . . . .  | 56        |
| 5.2.1 Reversal mechanisms . . . . .   | 56        |
| 5.2.2 Shape of switching fields . . . . .   | 58        |
| 5.2.3 Intrinsic switching fields . . . . .  | 59        |
| 5.3 Methods . . . . .   | 59        |
| 5.3.1 Sample fabrication and properties . . . . .   | 59        |
| 5.3.2 Magnetic force microscope . . . . .   | 60        |
| 5.3.3 Measurement procedure . . . . .   | 60        |
| 5.3.4 Fitting procedure . . . . .   | 60        |
| 5.4 Results and discussion . . . . .  | 61        |
| 5.4.1 Determination of switching fields . . . . .   | 61        |
| 5.4.2 Switching field distributions . . . . .   | 62        |
| 5.4.3 Individual islands . . . . .  | 65        |
| 5.4.4 Discussion . . . . .  | 66        |
| 5.5 Conclusions . . . . .   | 68        |
| 5.6 Acknowledgment . . . . .  | 68        |
| <b>6 Tip coating thickness dependence of tip-sample interactions in magnetic force microscopy on patterned arrays</b> | <b>69</b> |
| 6.1 Introduction . . . . .  | 69        |
| 6.2 Theory . . . . .  | 72        |
| 6.2.1 Tip and sample model . . . . .  | 72        |
| 6.2.2 Simulation theory and method . . . . .  | 72        |

|          |  |            |
|----------|--|------------|
| 6.2.3    | Simulation results . . . . .   | 74         |
| 6.3      | Experiment . . . . .   | 76         |
| 6.3.1    | Side-coated MFM tips . . . . .   | 76         |
| 6.3.2    | Patterned arrays . . . . .   | 77         |
| 6.3.3    | Experimental procedures and methods . . . . .  | 78         |
| 6.4      | Results and discussion . . . . .   | 81         |
| 6.4.1    | Read back . . . . .  | 81         |
| 6.4.2    | Write field . . . . .  | 81         |
| 6.4.3    | Undesired tip-sample interactions . . . . .  | 84         |
| 6.4.4    | Discussion . . . . .   | 85         |
| 6.5      | Conclusions . . . . .  | 87         |
| 6.6      | Acknowledgment . . . . .   | 89         |
| <b>7</b> | <b>Simulating 3D self-assembly of shape modified particles using magnetic dipolar forces</b> | <b>91</b>  |
| 7.1      | Introduction . . . . .   | 91         |
| 7.2      | Self-assembly experiment . . . . .   | 92         |
| 7.2.1    | Experimental setup . . . . .   | 92         |
| 7.2.2    | Video analysis . . . . .   | 93         |
| 7.3      | Simulation theory and procedure . . . . .  | 94         |
| 7.3.1    | Magnetostatic energy of dipoles . . . . .  | 94         |
| 7.3.2    | Energy minimization procedure . . . . .  | 96         |
| 7.4      | Results and discussion . . . . .   | 96         |
| 7.4.1    | Energy barriers . . . . .  | 97         |
| 7.4.2    | Experimental verification . . . . .  | 99         |
| 7.4.3    | Shape modifications . . . . .  | 99         |
| 7.5      | Conclusions . . . . .  | 102        |
| 7.6      | Acknowledgment . . . . .   | 103        |
| <b>8</b> | <b>Using magnetic levitation for 2D and 3D self-assembly of cubic silicon macroparticles</b> | <b>105</b> |
| 8.1      | Introduction . . . . .   | 105        |
| 8.2      | Experimental . . . . .   | 107        |
| 8.3      | Results and discussion . . . . .   | 109        |
| 8.3.1    | Levitation of single macrocubes . . . . .  | 109        |
| 8.3.2    | Two-dimensional self-assembly . . . . .  | 110        |
| 8.3.3    | Three-dimensional self-assembly . . . . .  | 112        |
| 8.4      | Conclusions . . . . .  | 114        |
| 8.5      | Acknowledgment . . . . .   | 116        |
| <b>9</b> | <b>Conclusions and recommendations</b>   | <b>117</b> |
| 9.1      | Patterned 2D arrays of islands . . . . .   | 117        |
| 9.2      | Self-assembled 2D and 3D arrays of particles . . . . .                                       | 119        |

|  |            |
|--|------------|
| <b>Appendices</b>                                  | <b>121</b> |
| <b>A Detection of island perimeters</b>            | <b>123</b> |
| A.1 Edge model and fitting procedure . . . . .     | 123        |
| A.2 improving the centers of the islands . . . . . | 123        |
| <b>B Method for 2D coding simulations</b>          | <b>125</b> |
| <b>C MFM sensitivity modeling and estimation</b>   | <b>127</b> |
| <b>D Magnetostatic energy of two cylinders</b>     | <b>129</b> |
| <b>E Diamagnetic levitation</b>                    | <b>131</b> |
| E.1 Diamagnetic levitation . . . . .               | 131        |
| E.2 Energy of assembly . . . . .                   | 132        |
| E.3 Perspective transformation . . . . .           | 134        |
| <b>Bibliography</b>                                | <b>136</b> |
| <b>Abstract</b>                                    | <b>154</b> |
| <b>Samenvatting</b>                                | <b>156</b> |
| <b>Dankjewels</b>                                  | <b>160</b> |
| <b>Publications</b>                                | <b>162</b> |

# Chapter 1

## Introduction

### 1.1 Magnetostatic interactions

Surely many of us have been encountering magnetic interactions from a young age. For instance, when magnets connect the wagons of our toy trains. I believe this cannot but trigger a desire to understand at least some of their physics.

The interactions result in forces. We can easily feel the forces between magnets of a few millimeter in size. Magnets interact over some distance, and the forces get stronger when the magnetic bodies come closer. With some handling or fumbling, it is rapidly found out which sides of the magnets interact attractively, and which repulsively. It is common knowledge that (iron) paperclips, screws, and refrigerator doors become magnets when a (permanent) magnet is near. These objects demagnetize when the magnet is removed. Clearly, magnetostatic interactions can cause a change in magnetization within bodies, and this happens almost instantly. We also know that the interactions are mediated by magnetic fields. The best known example is of course the magnetic field of the Earth turning compass needles towards the north. One only has to imagine a space filled with compass needles to visualize this vector field.

A lot of physics is thus learned from those every day experiences. Clearly, the time scales of the magnetization states of magnets range from instantly to permanently. The scales of the interactions range from huge (earths) to little (toys). And, even to tiny (bits) for those who appreciate digital data storage.

This intuition is at the heart of the magnetic force microscope (MFM), in its operation principle as well as in the interpretation of the images it produces. Magnetic force microscopy allows us to look at nanoscale magnets as small as  $\approx 10\text{ nm}$  in size. In an MFM [Abelmann, 2010], a magnetized tip is held (or shaken) near a magnetic sample. This allows us to determine the forces (or their gradients) by measuring the motion (or oscillation) of the tip. The MFM scans the tip over the surface of the sample, building an image of the magnetic forces. Pixels are colored more black or more white whenever the forces are respectively more strongly attractive or repulsive. Since we know magnetic bodies, we can

make an educated guess where the north and south poles of the sample must be situated. This makes an MFM a direct and flexible tool to investigate magnetic samples at the micro- and nanometer scale, and indispensable among more quantitative measurement devices based on *e.g.* optical or electronic effects.

Besides this, our experience is directly useful for systems that involve millimeter-sized magnets. Exciting ideas exist to let particles assemble by themselves [Whitesides and Grzybowski, 2002]. Magnetic interaction are excellently suited to investigate self-assembly of large scale prototypes of micro systems [Ilievski et al., 2011a; Shetye et al., 2008].

Magnetostatic interactions are not a fundamental force of nature; magnetism cannot be understood fully without considering dynamic and quantum interactions. Still, there is room for a quasi-static exploration in the paradigm of micromagnetism [Brown, 1963] and macro scale magnetic interactions.

### 1.1.1 Magnetostatic interactions in this thesis

This thesis is about magnetostatic interactions in arrays. The primary focus is on 2D arrays of patterned magnetic islands [de Vries, 2013; Murillo Vallejo, 2006], which are prototypical hard disk drive (HDD) recording media. I have researched the interaction involved in reading and writing such media, theoretically by means of modeling and simulations, and experimentally using magnetic force microscopy. In addition, I have investigated magnetostatic interactions for their use in the self-assembly of millimeter-sized particles into 2D and 3D arrays. The study of such large scale prototypes is aimed at the fabrication of 3D electronics, like 3D memories [Abelmann et al., 2010]. Besides possible applications in data storage, the two subjects have a common ground in the mathematical modeling of the interactions.

The next two sections briefly introduce the technological backgrounds of the patterned and self-assembled arrays. The specific issues addressed, and an outline of this thesis, are given in the section concluding this chapter.

## 1.2 2D arrays of patterned magnetic islands

The demand for more storage capacity requires recording media (*i.e.* HDD disks) with ever increasing areal bit density, and thus ever smaller bit sizes. Scaling down the dimensions of the media and head is however hampered by physical limitations (*e.g.* the ‘superparamagnetic limit’) [Moser et al., 2002]. To circumvent these limitations, new recording strategies are needed. Patterned island arrays and 2D recording schemes are promising solutions. However, there are also alternative technologies.

### 1.2.1 Bit patterned media

Conventional HDD recording uses granular media (see figure 1.1.a). To store a single bit of information, 10 to 100 grains about 5–10 nm in size, are magnetized

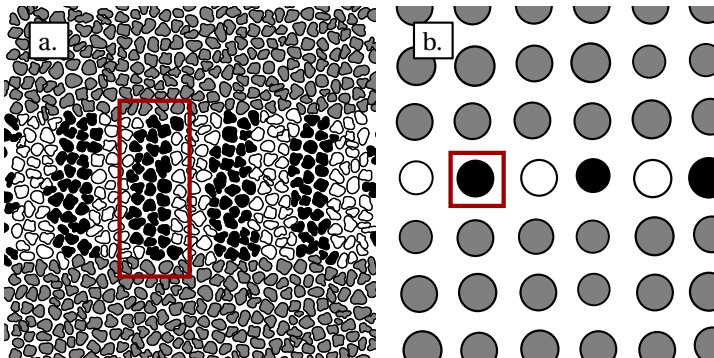


**FIGURE 1.1 – Illustration of a (a) granular media and (b) bit patterned media (BPM).** In granular media a collection of  $\sim 10\text{ nm}$  sized grains (white and black for the “1” and “0” bits in a track) defines a bit (e.g. red box). The random shapes (gray areas) and positions of the grains result in irregularly shaped bits, which cause noise in the read back signal (“media noise”). In BPM, a bit is stored in a single island that is larger and well defined by lithography. However, island size and position fluctuations (“jitter”), or a variation in island shape (as we will see in chapter 2), are sources of media noise in BPM.

in the same direction, either up or down. The grains are magnetically isolated (*i.e.* exchange decoupled), so they switch their magnetization individually when written and must be stable on their own account. There are two options to increase the areal bit density. One is by reducing the number of grains per bit. This will however result in more irregular shaped bits, causing excessive noise (“media noise”) in the read back signal. The other option is by reducing the size of the grains. However, this reduces the stability of the grains against thermal fields; a too small grain behaves superparamagnetically, having a magnetization that randomly fluctuates along with the thermal field.

From this media perspective, a solution is bit patterned media (BPM) recording [White, 1997], see figure 1.1 b. In this scheme, the bits are stored in islands defined by (lithographic) patterning. The better defined shape and larger volume of the islands, compared to that of a single grain, resolves both the media noise and stability issues. It seems natural to pattern islands in a regular structure, like the square patterned 2D arrays investigated in this thesis. Such 2D arrays have the advantage that the positions (or ‘phases’) of the bits within a track are synchronized among tracks. Read back strategies with multitrack detection in 2D recording schemes could exploit this phase synchronization.

### 1.2.2 2D recording

From a head perspective, issues in both reading and writing require a transition from conventional 1D to multitrack, 2D, recording schemes. The critical

dimensions concerning the head are the widths of the read and write elements, and also the head to media spacing. The widths cannot be reduced at the same pace as the track to track spacing, while maintaining a sufficient signal to noise ratio and write field gradient. The relatively large widths results in (more and unacceptable) cross-talk, both in reading and writing.

In read back, the cross-talk (or inter symbol interference (ISI)) is the magnetic field of nearby bits sensed by the head. Most significant are the bits in adjacent tracks; this is a source of random noise in conventional single track (1D) detection. Signal processing schemes that use the read back of multiple tracks, can handle the 2D ISI better [Nabavi and Vijaya Kumar, 2007]. For this, it is essential to have phase synchronization between tracks [Chan et al., 2012].

In writing, the magnetic field of the relatively wide head will overwrite bits in adjacent tracks. The ‘shingled writing’ [Wood et al., 2009] scheme accepts this. In this recording strategy, blocks of partially overlapping tracks are written as a single 2D unit of data. Due to the overlap, the final track width is reduced.

### 1.2.3 Alternative technologies

Bit patterned media evades the superparamagnetic limit, however the fabricating of the media is challenging [Terris and Thomson, 2005]. Also, writing at predefined island locations is new and problematic [Richter et al., 2006]. An alternative scheme is energy (*e.g.* heat or microwave) assisted magnetic recording. In this strategy, grains sizes are reduced. To ensure thermal stability, new materials (*e.g.* FePt) are being investigated that make grains harder to switch. As a result however, the write field of the head is insufficient to write those strong grains, and needs assistance of an additional energy source. In heat assisted magnetic recording (HAMR) [Kryder et al., 2008], a laser supplies this energy in the form of heat. HAMR is currently implemented, and postpones the introduction of BPM (which is projected for the year 2023 \*). When implemented, BPM recording will probably be combined with HAMR as those technologies are complementary.

Another alternative recording scheme, competing with BPM recording, is ‘two dimensional magnetic recording’ (TDMR) [Wood et al., 2009]. In this strategy, signal processing provides the solution to media noise and ISI. In this scheme, ideally each single grain holds a bit. The excessive media noise and ISI is handled by raster scanning the media (a bit like in MFM). Coding handles the uncertainty in the position and size of the grains/bits. Excitingly,  $> 0.7$  bits per grain could in theory be stored [Wood et al., 2009]. The TDMR strategy does not require new media technology to be developed, which is an advantage over BPM.

With these techniques, there seems material-wise no physical limitation to engineer media with up to  $100 \text{ Tb in}^{-2}$  density [Kryder et al., 2008] (currently the density is about  $1 \text{ Tb in}^{-2}$ ). Note however, that even at a historically small 20 %

---

\*According to the “2016 ASTC Technology Roadmap” [ASTC].

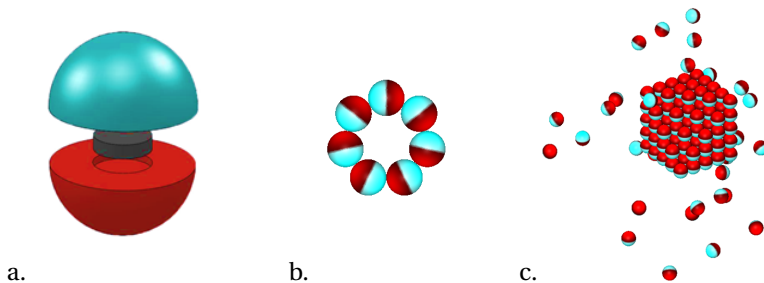


**FIGURE 1.2 – We investigate the self-assembly of millimeter-sized 3D printed particles equipped with a magnet; (a) shows the magnet and printed capsule (with a blue north and red south pole). Typically, such dipolar particles assemble in a 2D flux closing configuration i.e. a ring (b). Self-assembly of a 3D array (c) is desirable; in chapter 7 we research 3D self-assembly starting with 3–4 particle configurations.**

annual grow rate in areal density [Fontana et al., 2012], this huge  $100 \text{ Tb in}^{-2}$  is reached in 25 years. It is up to economics to decide whether HDDs will attain its physically ultimate density, or that, for instance, solid state memory will take over.

### 1.3 Self-assembling arrays

Historically, the areal density of non volatile semiconductor based memory doubles every 2 years (41 % annually), by scaling down the size of transistors <sup>†</sup>. For the storage elements [ITRS, 2013], which are NAND-Flash transistors in solid state drives (SSD), a  $(24 \text{ nm})^2$  size is the projected minimum area (this corresponding to  $1.1 \text{ Tb in}^{-2}$ ). This density could be attained already in the year 2018. To further increase the capacity, 3D structures are being fabricated in which layers of transistors are stacked vertically at acceptable costs. However, to keep up scaling, the number of layers should increase exponentially. Ensuring good quality over the layers, from bottom to top, is a major concern.

Self-assembly offers the possibility to access the vertical dimension in fabrication as easily as conventional planar dimensions. In a self-assembly process, particles in a container spontaneously organize into a (desired) configuration, with possibly some help of external agitation or manipulation that is not directed at particles individually. Useful structures may result from a careful design of the particles, environment and external forces [Elwenspoek et al., 2010]. Desirably, the particles form a 3D array of storage elements, and also provide

---

<sup>†</sup>The International Technology Roadmap for Semiconductors publishes detailed roadmaps for the (near) future of semiconductor applications, e.g. [ITRS, 2013]

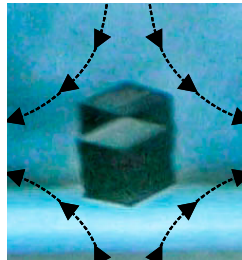


**FIGURE 1.3 – Photograph of two diamagnetically levitated silicon particles in a paramagnetic liquid. An applied magnetic field (arrows) magnetizes the liquid attractively and the particle repulsively, forcing the particles against gravity to a low field region (in the center). In chapter 8 we explore levitated particle clusters and their self-assembly in 2D and 3D arrays.**

the wiring to access the elements, for instance as in a 3 wire cross point structure [Abelmann et al., 2010]. This is not an easy task. Encouragingly, structures with various functions have been self-assembled [Mastrangeli et al., 2009], also based on magnetic interactions.

Strong permanent (e.g. ‘neodymium’ (NdFeB)) magnets enable the research of self-assembly at an easy accessible, millimeter scale (see the approaches in figures 1.2 and 1.3). The forces are strong enough to levitate particles in a paramagnetic liquid [Mirica et al., 2011]. Moreover, the interactions of particles equipped with magnets, are strong enough to result in binding [Boncheva et al., 2005].

## 1.4 Outline of thesis

The first chapters (chapters 2–6) concern magnetostatic interactions in the imaging (or reading) and switching (or writing) of 2D patterned island arrays. Chapters 7–8 are about the magnetostatic interactions as driving and binding force in self-assembly.

Chapter 2 presents a model for the media noise caused by the fluctuating shapes of the patterned islands. The fluctuations result from the finite resolution of the patterning process. The shapes fluctuations are determined and their effect on read back is theoretically investigated.

In chapter 3, a 2D code that avoids 2D-ISI is presented and tested in simulations. Such coding could aid in the correct detection of bits, possibly reducing the need for complex signal processing.

Chapter 4 is about the distortions in MFM read back and their corrections. The distortions are due to the topography of the island arrays, and the liftmode MFM operation.

Chapter 5 reports the MFM investigation of switching fields and reversal mechanisms of islands in globally applied fields. Fluctuations from island to islands cause a distribution in switching field. For patterned  $\approx 100\text{ nm}$  sized islands, the reversal mechanisms are not completely understood.

The interaction of the local stray field of the tip and the islands is investigated in chapter 6. The effect of tip coating thickness is probed using the read back and switching fields of patterned arrays. Desirably, the field of the tip has sufficient strength to manipulate (*i.e.* write) islands.

In chapter 7, the preferred configurations involving 3–4 self-assembling particles with magnetic dipole moments are investigated in simulations. Such small assemblies are important as they form the seeds for larger assemblies. Typically, dipolar particles assemble in 2D configurations, but this could be different for particles with a non-spherical shape.

Chapter 8 is about magnetic levitation with anisotropic (cubic) millimeter-sized silicon particles. Magnetostatic interactions are used to suspend the particles and to force the particles together. The target structures are 2D and 3D arrays. Templating and tuning of the hydrophilicity of the particles are investigated to improve the quality of the arrays.

Chapter 9 states the conclusions and recommendations of this thesis.



## Chapter 2

# Determination of bit patterned media noise based on island perimeter fluctuations

### Abstract

This chapter is based on [Alink et al., 2012] \*. We measured the fluctuation in shape of magnetic islands in bit patterned media fabricated by laser interference lithography. This fluctuation can be accurately described by a model based on a Fourier series expansion of the perimeter of the islands. The model can be easily linked to amplitude and jitter noise. We show that the amplitude and jitter noise are in principle correlated, and the jitter noise increases with increasing island area. The correlation is small for media prepared by laser interference lithography, but expected to gain importance for high density bit patterned media.

### 2.1 Introduction

Bit patterned media (BPM) have been proposed as an alternative to granular media to overcome the superparamagnetic limit in hard disk drive (HDD) recording [White, 1997]. An accurate model for media noise in BPM is needed in order to develop coding and detection schemes. In granular media, media noise is mainly caused by poorly defined transitions between bits. This cause is absent in BPM recording. In BPM, media noise is caused by variations in the lithographic patterning process. There are two sources of noise. Due to the limited resolution of the lithography process, the patterned islands will have jagged edges [Nair and Richard, 1998]. As a result, the shape of the islands fluctuates, which causes fluctuations in both the size and position (*i.e.* center of mass) of

---

\*This work is published in Alink L., Groenland J.P.J., De Vries J., Abelmann L., 2012 “Determination of bit patterned media noise based on island perimeter fluctuations” *IEEE Trans. Magn.* **48**, p. 4574.

the island. Secondly, the islands may be randomly translated, as is, for instance, the case in self-assembled media [Nabavi et al., 2009], leading to fluctuations in position as well.

The noise analysis of bit patterned media has received increased attention during the last years. For BPM patterned by electron-beam lithography, fluctuations in the positions and sizes of the islands were obtained in [Nutter et al., 2008]. In both [Aziz et al., 2002] and [Nutter et al., 2008], approximate Gaussian distributions were found. In [Nutter et al., 2008], the standard deviations of these distributions increased as the island size decreased, indicating that media noise will be severe when recording at high areal densities. In [Nabavi et al., 2009] a scanning electron microscopy (SEM) image of a self-assembled mask was used to determine the position and size fluctuations. The correlation in the position and the correlation in the size of the islands were characterized and modeled. Simulations showed improved bit error rates for detectors that were designed to handle such correlations.

Despite these observations, it is still common practice to model island position and size fluctuations by two uncorrelated Gaussian distributions (*e.g.* [Nutter et al., 2008]). This is physically incorrect. In the first place, the distribution cannot be Gaussian, because for most fabrication processes the islands will never overlap. This is sometimes taken into account by using a rather arbitrarily truncated distribution [Ntokas et al., 2007]. Secondly, the position and size fluctuations caused by shape fluctuations are expected to be correlated.

In this chapter, a new model for media noise in BPM is proposed, which is based on island perimeter fluctuations. This model intrinsically incorporates the correlation between position and size fluctuations. We tested this model on patterned media prepared by laser interference lithography (LIL) [Haast et al., 1998]. BPM fabricated by LIL form excellent test media because the interference patterns have perfect positioning [Luttge et al., 2007]. Random translations, such as in self-assembled or e-beam generated media, are therefore absent, and the fluctuations in the position of the islands are caused by shape fluctuations only.

The model is presented and analyzed in section 2.2. The methods used for BPM fabrication, image processing, and simulations are briefly discussed in section 2.3. The results of experiment and the simulations are presented in section 2.4. These results are discussed in section 2.5 and our conclusions are summarized in section 2.6.

## 2.2 Theory of shape fluctuation modeling

We consider islands that are patterned into a magnetic layer with uniform thickness  $t_s$ . We assume uniform sidewall profiles (*e.g.* constant slopes over the radii of the islands). We define the perimeter of an island by the contour that encircles the island at height  $t_s/2$  from the bottom surface. The fluctuations in shape of such islands are characterized by fluctuations in their perimeters. The

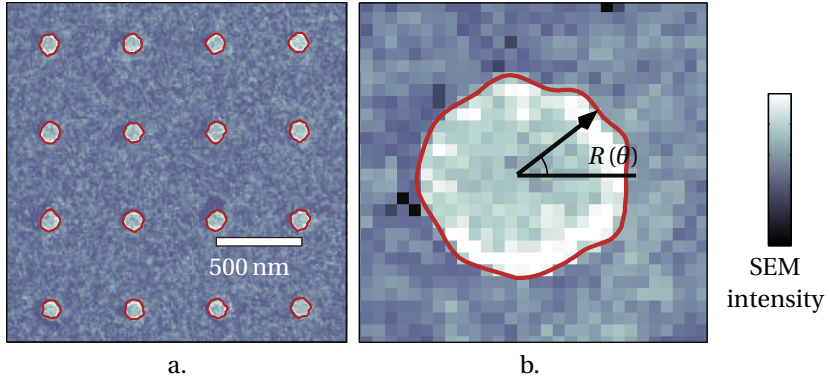


FIGURE 2.1 – (a) SEM image of Co/Pt multilayer islands with 55 nm radius spaced by 500 nm produced by laser interference lithography. (b) one single island showing the function  $R(\theta)$  that describes its perimeter (red contour).

distance from the center of an island to a point on its perimeter can be represented by a function of angle  $R(\theta)$ , as shown in figure 2.1.b. Note that for very irregular islands, the perimeter might not be a single-valued function of  $\theta$ . However, the islands in figure 2.1.a have smooth shapes, and the perimeters can be represented by their Fourier series

$$R(\theta) = \sum_{n=-\infty}^{\infty} c_n \exp(i\theta n). \quad (2.1)$$

Note that  $c_n$  and  $c_{-n}$  are complex conjugate pairs because  $R(\theta)$  is real. The Fourier coefficients are defined by

$$c_n \equiv \frac{1}{2\pi} \int_0^{2\pi} R(\theta) \exp(-i\theta n) d\theta. \quad (2.2)$$

We may characterize the fluctuations in the shape by the fluctuations in the coefficients  $c_n$ . We therefore consider the power spectrum of  $R(\theta)$ , which is defined as the Fourier series of the periodic auto-correlation of  $R(\theta)$  [Haykin, 1989]. In terms of the Fourier components, the power spectrum is given by the variance in  $|c_n|$ ,

$$S_n = \langle |c_n - \langle c_n \rangle|^2 \rangle, \quad (2.3)$$

where  $\langle \cdot \rangle$  denotes the mean. For islands that have on average a circular shape, the mean of  $c_0$  is the mean island radius,  $R_0$ , and the other coefficients have zero mean. Since  $S_{-n} = S_n$ , only the positive components and  $S_0$  need to be considered.

The power spectrum characterizes the shape fluctuations if: (I) There is no correlation between the  $c_n, c_{-n}$  pairs. This is a reasonable assumption if the

patterning process does not favor a certain shape for the islands (*i.e.* is isotropic in the plane of the media). (II) The distribution of  $c_n$  and  $c_{-n}$  is given by the variance in  $|c_n|$ . For small fluctuations in  $R(\theta)$  compared to the nominal island radius,  $R_0$ , we expect the fluctuations to be approximately Gaussian distributed and described by the variance. If the fluctuations are large, the distribution of  $c_n$  cannot be Gaussian, but may still be characterized by the variance.

The shape of an island depends on the resolution of the patterning process. This resolution is limited by the resolution of the mask (*e.g.* the photoresist pattern) that is transferred into the recording layer <sup>†</sup>. We assume that no high frequency components are significantly present in the perimeters of the islands and that most of the noise power is contained in the first components of the spectrum. In that case, only a few components of the power spectrum are needed to characterize the shape fluctuations.

To analyze the effect of shape fluctuations on the HDD read back signal, we can, to first order, use the far-field approximation for the island's magnetic field. In this approximation, we may consider an island as a single magnetic dipole. For an island with a uniform magnetization, the dipole's magnetic moment is determined by the volume of the island, which is proportional to the island's area. The position of the dipole is given by the island's center of mass. As a result, the read back signal of a flux sensor which is scanning such an island (*i.e.* a dipole), is a pulse which is positioned at the center of mass with an amplitude proportional to the island's area.

The read back signal is the average of the magnetic field over an area of the order of the bit size. Because of the averaging, the fluctuations in the area and center of mass of the islands are first approximations for respectively the amplitude and position jitter in the read back signal. We derive expressions for the fluctuations in the area and center of mass in terms of the Fourier coefficients in (2.1). For simplicity we consider islands with vertical sidewalls.

The area ( $A$ ) of an island follows from Parseval's theorem,

$$A = \int_0^{2\pi} \int_0^{R(\theta)} r dr d\theta \quad (2.4)$$

$$= \frac{1}{2} \int_0^{2\pi} R(\theta)^2 d\theta = \pi \sum_{n=-\infty}^{\infty} |c_n|^2. \quad (2.5)$$

An approximation using only  $c_0$  and  $c_1$  is

$$A \approx \pi (c_0^2 + 2|c_1|^2). \quad (2.6)$$

---

<sup>†</sup>Also the pattern transfer could result in smoother island edges [Constantoudis et al., 2009]

The coordinates  $(x_c, y_c)$  of the center of mass are given by

$$x_c = \frac{1}{3A} \int_0^{2\pi} R(\theta)^3 \cos(\theta) d\theta \quad (2.7)$$

$$y_c = \frac{1}{3A} \int_0^{2\pi} R(\theta)^3 \sin(\theta) d\theta. \quad (2.8)$$

The expectation for the position of the center of mass of an island is  $\langle x_c \rangle = \langle y_c \rangle = 0$ . To analyze the fluctuations in the center of mass, we consider its distance from the origin

$$r_c = \sqrt{x_c^2 + y_c^2} = \left| \frac{1}{3A} \int_0^{2\pi} R(\theta)^3 \exp(-i\theta) d\theta \right|. \quad (2.9)$$

On substituting (2.1) for  $R(\theta)$  in (2.9), an expression for  $r_c$  in terms of the coefficients is obtained,

$$r_c = \left| \frac{2\pi}{3A} \sum_{\text{all } \{k,l,m\} \in \{k+l+m=1\}} c_k c_l c_m \right|. \quad (2.10)$$

The term  $(c_0 c_0 c_1)$  occurs three times in the sum. This is the dominating term in case the fluctuations are small ( $c_0 \gg c_n$  for  $n > 0$ ). Therefore, an approximate expression for the center of mass is given by

$$r_c \approx \frac{2\pi}{A} c_0^2 |c_1|. \quad (2.11)$$

Due to the presence of  $A$  in (2.10), it appears that under our assumptions the fluctuation in area and in the center of mass of an island are correlated. Substituting the approximation for the area in (2.6) into (2.11), the fluctuation in the center of mass can be expressed as a function of  $A$  and  $c_1$  only:

$$r_c \approx 2 |c_1| - \frac{4\pi |c_1|^3}{A}. \quad (2.12)$$

The expectation of  $r_c$  depends on  $A$ . Therefore the fluctuation in the center of mass and the area are indeed correlated. With increasing area, the fluctuation in the center of mass increases, saturating at a maximum of  $2|c_1|$  for very large areas. A similar correlation between the position and amplitude jitter caused by shape fluctuations is expected for the read back in an HDD.

## 2.3 Experimental method and simulation procedure

### 2.3.1 Fabrication of patterned media

To fabricate the base layer for the BPM, a Pt seed was sputtered onto a thermally oxidized  $\text{SiO}_2$  layer. On top of the seed layer, a  $[\text{Co}(0.4 \text{ nm})/\text{Pt}(1 \text{ nm})] \times 5$

multilayer and a 2 nm Pt capping layer were sputtered. The base layer is similar to the base layer in [Delalande et al., 2012]. The layer was patterned by LIL using a bottom anti-reflective coating (BARC) below the photoresist to reduce the influence of standing waves caused by reflection from the metallic layer. The photoresist was transferred into the BARC and magnetic multilayer by a subsequent O<sub>2</sub> plasma and Ar etch, respectively. After transferring the pattern, the BARC was removed, although we cannot exclude the possibility that some BARC residue may remain on top of the islands. Details of the LIL patterning are given in [de Vries, 2013].

The resulting BPM has a 500 nm bit period, with a nominal island radius of  $R_0 = 55$  nm. The nominal area is therefore  $A_0 = \pi R_0^2 = 9.5 \times 10^3$  (nm)<sup>2</sup>.

### 2.3.2 SEM imaging

The islands were imaged using an SEM (FEI NovaLab600, SE mode, 10 kV). As a result, the resolution of the SEM image is 6.25 nm per pixel. For most of the islands, the SEM image showed a clear contrast between the top of the islands and the background. The transition between top and background intensities followed an approximately arctangent shape.

The perimeters of 330 islands were detected by image processing (see Appendix A). The centers of the islands were coarsely detected by low pass filtering and peak detection. Twenty points were fitted to the perimeter of each island, using an arctangent sidewall profile. After detecting the perimeters, the coarse positions of the islands were updated in an iterative process. In each iteration, the centers of the islands were set to the center according to the centers of its eight nearest neighbors. Islands that were not updated (*i.e.* islands near the edge and near badly detected islands) were not considered in the next iteration. The centers of the islands settled down after eight iterations.

With these centers, a discrete representation of  $R(\theta)$  is obtained. The coefficients  $c_n$  are obtained for each island via a discrete Fourier transform. The power spectrum is obtained using (2.3).

### 2.3.3 Simulation of perimeters

Using the obtained power spectrum, the island perimeters were simulated. We started by simulating the shape of  $10^5$  islands by sampling the real and imaginary parts of  $c_n$  from a Gaussian distribution with variance  $S_n/2$ . The negative components are set by  $c_{-n} = \overline{c_n}$ , where  $\cdot$  denotes the complex conjugate. The coefficient  $c_0$  is real, and therefore sampled from a Gaussian distribution with variance  $S_0$ . A discrete representation of an island's perimeter is obtained via a discrete inverse Fourier transform. A smooth contour that approximates a continuous  $R(\theta)$ , as the contour shown in figure 2.1.b, results after interpolation.

We subsequently obtained the distribution of the fluctuations in the area and center of mass of the simulated islands via (2.5) and (2.10), respectively.

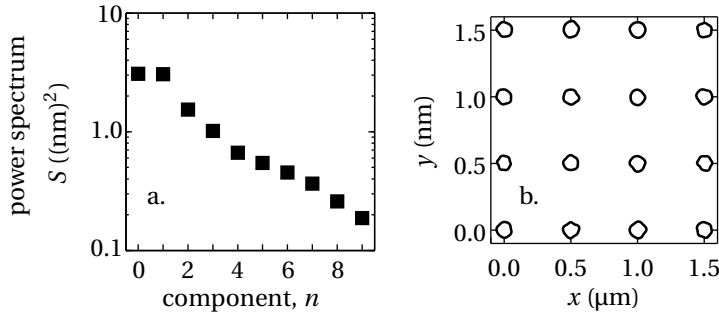


FIGURE 2.2 – (a) Power spectrum  $S_n$  showing the variance of Fourier component  $c_n$  of the perimeter  $R(\theta)$ , determined from the SEM image in figure 2.1. (b) Simulated perimeters using the first 7 frequency components ( $0 \leq n \leq 6$ ) of the power spectrum.

## 2.4 Results

Figure 2.1.a shows 16 islands in the SEM image and their detected perimeters. The power spectrum resulting from these perimeters is given in figure 2.2.a. The spectrum shows a decreasing amplitude for higher component number  $n$ . The first 7 components contain 90% of the total noise power. Using these 7 components, we simulated the perimeters in figure 2.2.b. The simulated perimeters indeed have realistic shapes compared to the islands in figure 2.1.

The distributions of the detected areas and centers of mass for 330 islands are given in figure 2.3. Also shown are the distributions resulting from the simulations using the power spectrum in figure 2.2, taking all components into account. The simulated distributions have standard deviations that are in good agreement with those obtained using the measured spectrum. Simulations using only the first 7 components of the spectrum resulted in nearly identical distributions, with standard deviations also within 2 % of those obtained using the measured spectrum.

The correlation between the fluctuations in the center of mass and area were found to be small for the power spectrum of the detected perimeters. We therefore increased the power in the fluctuations by increasing the magnitude of all components in the spectrum by a constant factor. This is similar to reducing the nominal area of the islands by this factor, while keeping the noise power at the same level. This scaling of the media noise is optimistic compared to the increase in media noise for smaller islands that is observed in [Nutter et al., 2008]. Concerning the shape of the spectrum, we expect that at some point the higher frequency components will be attenuated for increasingly smaller islands, because of the limited resolution of the photoresist. A detailed description of the scaling of the power spectrum is, however, not available. We use

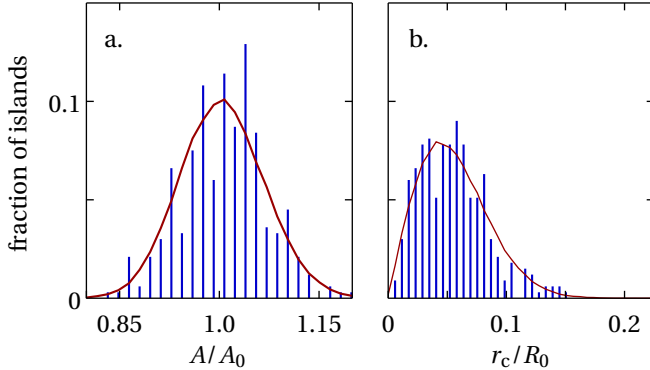


FIGURE 2.3 – *Histograms of the area (a), center of mass (b), according to the detected perimeters in the SEM (blue bars) and simulated perimeters (red lines) with the power spectrum in figure 2.2. The standard deviations are  $0.030R_0$  and  $0.063A_0$  for the detected center of mass and area, respectively. The standard deviations of the simulated distributions are within 2% of those of the measured distributions.*

the simple model of constant noise power as a starting point to investigate the effect of shape fluctuations at higher areal densities.

Figure 2.4.a shows the histogram for a noise power increased by a factor of ten. The correlation becomes very clear when we plot the expectation for the position  $r_c$  as a function of the area  $A$ , see figure 2.4.b. For an uncorrelated relation, the line would be horizontal. Figure 2.4.b confirms equation (2.11), indeed the expectation for the center of mass increases with increasing island area. From the figure, we observe that for a  $\pm 15\%$  variation in island size, the expectation for the center of mass varies by 1.3% of  $R_0$ .

## 2.5 Discussion

The simulated distributions show that the power spectrum characterizes the fluctuations in the shape of the islands in LIL patterned media. According to the theoretical analysis, we expect a correlation between the center of mass and the area of the islands. For the measured islands, the fluctuations in the shape are small (compared to  $R_0$ ) and the simulations show no clear correlation. However, we can reveal the correlation if the fluctuations in shape are increased by boosting the power spectrum. In [Nutter et al., 2008] it was found that island size and position jitter increases for smaller islands. We therefore expect that the fluctuations in island shape will increase with areal density. From the simulations with the boosted power spectrum, we may expect correlated media noise in recording at high areal densities.

The presented model can easily be extended to higher density BPM, such

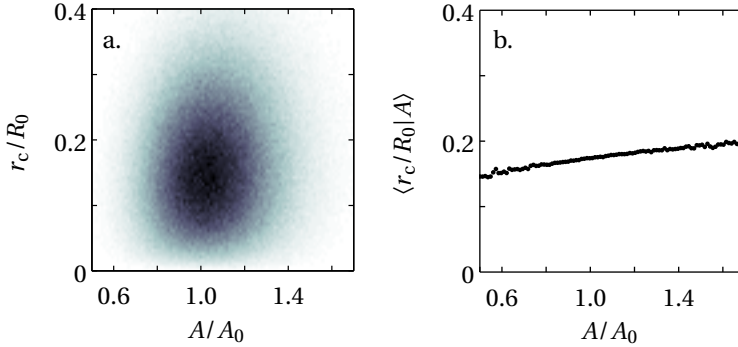


FIGURE 2.4 – (a) 2D histogram of the fluctuations in center of mass ( $r_c$ ) and island area ( $A$ ) resulting from the simulation of  $10^5$  islands, generated using a power spectrum with magnitude 10 times greater than the spectrum in figure 2.2. Darker colors correspond to more islands. (b) Simulated conditional expectation for  $r_c$  given  $A$ . The graph clearly shows that an increase in area ( $A$ ) is accompanied by an increase in position jitter ( $r_c$ ).

as prepared by e-beam lithography masks and nano-imprint or self-assembly. The only requirement is that the fabrication method is isotropic in the plane of the film.

## 2.6 Conclusions

The fluctuation of the perimeter of magnetic islands in bit patterned media were measured, and we modeled these fluctuations by a Fourier series. We showed that the fluctuations can be accurately approximated by using only a limited number of components of the Fourier power spectrum. The first 7 components contain 90% of the noise power. Simulated islands using these components have realistic shapes. Moreover, the distributions of the fluctuation in position and size of the simulated islands have standard deviations which are within 2% of those obtained from the distributions of the measured islands.

From the new model we conclude that the fluctuations in area and position of the islands, which are conventionally used in noise analysis, are correlated. The fluctuation in the position of an island increases with the island's area. For the laser interference lithography fabricated media investigated, the correlation is difficult to observe. If the noise spectrum is increased by a factor of 10 however, we could reveal that the expected value for the position of the island fluctuates by 1.3% of the island's radius for fluctuations in its area of  $\pm 15\%$ .

We therefore believe that the model presented here is more accurate and provides a better representation of physical reality than standard models which use uncorrelated Gaussian distributions for amplitude and jitter noise in bit

patterned media.

## **2.7 Acknowledgment**

I and my colleagues would like to thank M. Siekman and H. van Wolferen for technical assistance, M. Delalande for fabricating the BPM, and X. Shao for discussions.

This research is supported by the Dutch Technology Foundation STW, applied science division of NWO and the technology program of the Ministry of Economic Affairs.

## Chapter 3

# A simple two-dimensional coding scheme for bit patterned media

### Abstract

This chapter is based on [Shao et al., 2011] \*, in which I contributed in the modeling of the channel. We present a simple code to combat the two-dimensional inter-symbol interference (2D-ISI) effect that occurs in data storage on magnetic bit patterned media. Whether the ISI effect is constructive or destructive depends on the surrounding bits. Therefore, we propose a simple 2D coding scheme to mitigate the ISI effect. With this 2D coding scheme in square patterned media, every 2-by-3 array has one redundant bit which has the opposite or same value of one of its adjacent bits. Compared to the 2D coding scheme in [Groenland and Abelmann, 2007] under the condition of the same areal density, the proposed 2D coding scheme increases the allowable bit-position jitter in square patterned media by 1 % at a BER of  $10^{-4}$ ; while it allows the effective storage capacity to be increased by around 5.5 %.

### 3.1 Introduction

Thermal stability places a fundamental limit on the possible increase in areal density for magnetic recording. To increase the capacity of hard disk drives (HDD) beyond the superparamagnetic limit, one feasible approach is to use bit patterned media [Abelmann, 2010]. On such media, magnetic islands (or dots) are defined by patterning and located at known positions. Each island stores one bit. This is in contrast to conventional media, where multiple, randomly positioned grains are needed to store a single bit. The switch from conventional to bit patterned media requires fundamental changes in fabrication [Terris and

---

\*This work is published in Shao X., Alink L., Groenland J.P.J., Abelmann L., Slump C.H., 2011 “A simple two-dimensional coding scheme for bit patterned media” *IEEE Trans. Magn.* **47**, p. 2559.

[Thomson, 2005](#). In order to achieve ultra-high storage densities, it is advantageous if the dot period (*i.e.* the distance between the center of an island and the center of its closest neighbor island) is small in both the along track and across track direction. Therefore, HDD recording and the problem of ISI becomes two-dimensional [[Wood et al., 2009](#)].

The ISI effect can be constructive and destructive, which is determined by the read back pulse form (*e.g.* with or without overshoot), and the value of its surrounding bits. This chapter is about a read back pulse with overshoot, *i.e.* with negative going signal at the side tails of the pulse, as shown in figure 3.1. Due to the overshoot, the signal of the center bit is boosted if *e.g.* the “1” bit is surrounded by “0” bits (*i.e.* the best case); while the signal of the center bit is much reduced if *e.g.* all “1” bits are stored in a 3-by-3 array (*i.e.* the worst case). In the worst case, the signal of the target bit is so small that jitter or medium noise can easily lead to detection errors and unreliable recovery of the stored data.

The destructive ISI effect can be mitigated by the Viterbi equalization and detection algorithm. However, the Viterbi algorithm is characterized by its high complexity, especially in the 2D-ISI case [[Keskinoz, 2008](#)]. If the destructive effect of ISI can be avoided, it is not necessary to use the Viterbi or other equalization algorithms. In such a case, the recording system can be implemented at a relatively low complexity. In [[Groenland and Abelmann, 2007](#)], we proposed a 2D coding scheme which is specially designed to avoid the worst case ISI (as shown in figure 3.2). The basic idea of this 2D coding scheme is to place a “1” and “0” (corresponding to respectively up and down magnetized islands) in fixed positions at every 3-by-3 array. In this chapter, we call this 2D coding scheme the 7/9 coding scheme. Comparing to the no-coding case, this type of 2D coding achieves a significant gain in terms of bit error rate (BER) by taking a redundancy of 2/9. However, this coding scheme has a drawback that the redundant bits have no error correction ability if we apply the simplest threshold detection. Therefore, we propose another simple coding scheme which has lower redundancy and better performance than this coding scheme.

In this chapter a simple 2D coding scheme for bit patterned media is proposed. First (section 3.2), we briefly depict the read back pulse, which is used to evaluate the performance of the 2D coding scheme. Then (section 3.3), we explain how the proposed 2D coding scheme is designed for square patterned media and hexagonal patterned media, respectively. In section 3.4, we analyze the performance of this coding scheme in the simulation. The chapter ends with a discussion of results.

## 3.2 Theory: read back signal

To avoid experimental complications, we have chosen to validate the 2D coding techniques proposed here on a magnetic force microscopy (MFM) platform [[Thomson et al., 2007](#)] in future experiments. Therefore our read back pulse

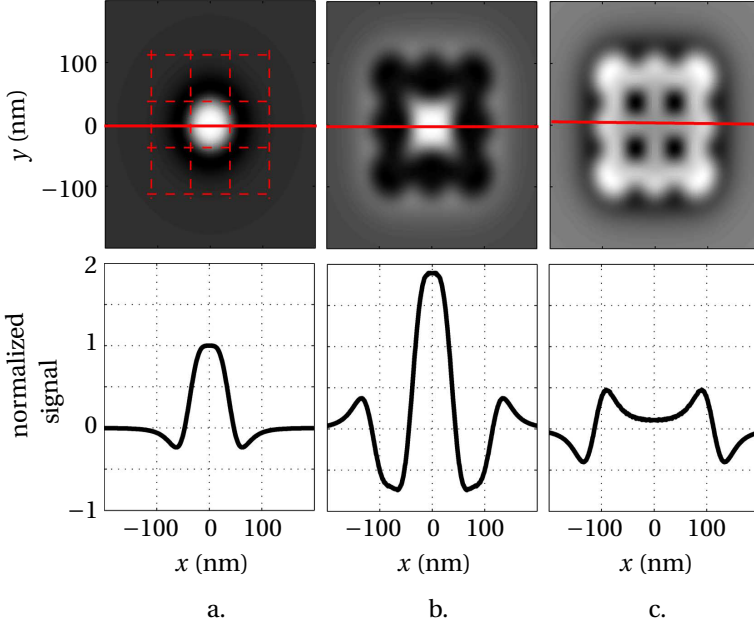


FIGURE 3.1 – The simulated MFM images (top) and the selected and normalized MFM readout signal curves (bottom). The read back signal is simulated according to [Abelmann, 2010] and based on the parameters in table 3.1. (a) A single dot. (b) The best case, e.g. the “1” bit is surrounded by all “0” bits. (c) The worst case, e.g. the “1” bit is surrounded by all “1” bits.

model is based on MFM image formation [Abelmann, 2010], rather than the read back model for a single pole head in a hard disk system. The main difference between these models is that the MFM signal is proportional to the second derivative of the magnetic stray field with respect to the vertical direction, whereas the single pole head would generate a signal proportional to the field. This difference will not affect the major conclusions with respect to the efficiency of the codes.

The tip of the MFM probe is modeled as a uniformly magnetized bar (the dimensions are given in table 3.1). The dots are modeled as uniformly magnetized cylinders, ordered in a square or hexagonal pattern. Figure 3.1.a shows the MFM response of a single dot. The overshoot that is present in the pulse, can result in constructive or destructive ISI (e.g. figures 3.1.b and 3.1.c, respectively). The worst case occurs when all dots in a 3-by-3 array have the same value. In such a case, bits can be easily detected in error. Therefore, we propose a simple 2D coding scheme to avoid the worst ISI effect, which will be explained in the next section.

TABLE 3.1 – *Geometric parameters of the bar shaped tip and cylindrical islands as used in simulations*

| parameter                     | value (nm) |
|-------------------------------|------------|
| tip thickness, $t$            | 75         |
| tip width, $w$                | 75         |
| tip height, $L$               | 1000       |
| island diameter, $D$          | 37.5       |
| island period, $\Lambda = 2D$ | 75         |
| island thickness, $t_s$       | 10         |
| tip-sample distance, $z$      | 25         |

### 3.3 The simple coding scheme

The simple 2D coding scheme we propose, is designed to combat the 2D-ISI effect. Because the ISI effect is dependent on the read back pulse form (*e.g.* with or without overshoot) and the surrounding bits, different pulse forms and different types of patterned media (*e.g.* square patterned media or hexagonal patterned media) require different coding designs. This section explains the proposed 2D coding scheme for square and hexagonal patterned media, where the MFM based recording channel with overshoot is assumed.

The proposed 2D coding scheme for square patterned media is depicted in figure 3.2. In this figure, the white dots are used to store the information bits and the black dots are the parity check bits of one of their adjacent bits. In this way, the worst case of all “1”’s or “0”’s in a 3-by-3 array can be avoided. Besides, the redundant bits have an error-correction capability since they are the parity check bits of some information bits. As mentioned earlier, the previously developed 7/9 2D coding scheme avoids the worst case by putting a “1” and “0” in fixed places, where the added bits do not contain any information from the stored data. The proposed coding scheme is expected to have better performance than the 7/9 coding scheme, as the added bits are parity bits. Furthermore, the proposed 2D coding scheme has a code rate of 5/6, which allows the storage capacity to be increased by around 5.5 % comparing to the 7/9 2D coding scheme.

The proposed 2D coding scheme can be easily extended to hexagonal patterned media as shown in figure 3.3. Similar to figure 3.2, the white dots are used to hold the information bits and the black dots are the parity check bits of one of their adjacent bits. As seen in figure 3.3, we do not have any “1” surrounded by all “1”’s or any “0” surrounded by “0”’s. For hexagonal patterned media, the code rate is decreased to 3/4.

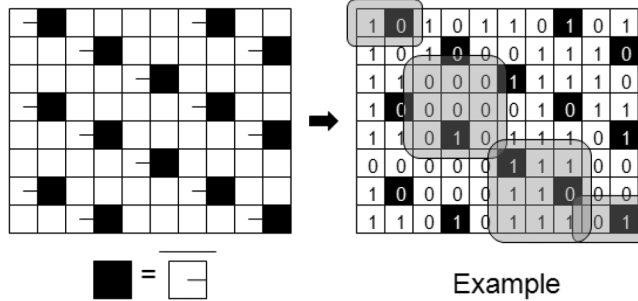


FIGURE 3.2 – The proposed 2D coding at the code rate of 5/6 for square patterned media and the recording channel with overshoot. The white dots are used to store the information bits and the black dots are the parity check bits of one of their adjacent bits. In the example with coded data, worst case ISI patterns do not occur (e.g. highlighted  $3 \times 3$  squares) due to the parity bits (e.g. small highlighted areas).

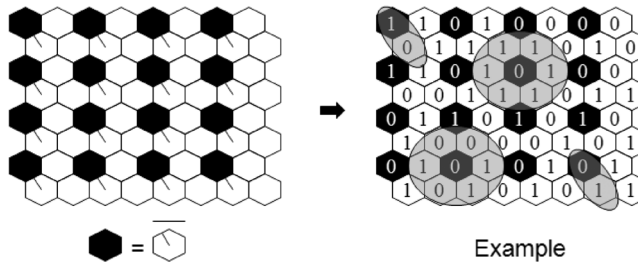


FIGURE 3.3 – The proposed 2D coding at the code rate of 3/4 for hexagonal patterned media and the recording channel with overshoot. The white dots are used to store the information bits and the black dots are the parity check bits of one of their adjacent bits. In the example with coded data, worst case ISI patterns do not occur (e.g. highlighted circles) due to the parity bits (e.g. small highlighted areas).

### 3.4 Simulation results and discussion

The performance of the proposed 2D coding scheme is evaluated in the simulation. The simulation procedure is described in Appendix B. We do not use any equalization algorithm. The Viterbi algorithm would provide the optimal solution with a superior performance at the expense however of an increased detector complexity [Burkhardt, 1989]. In a 2D-ISI channel with size  $N$  by  $N$ , the complexity of the 2D Viterbi detection algorithm increases exponentially with

$N^2$  which makes the 2D Viterbi scheme impractical [Keskinoz, 2008]. Therefore, we use the simple threshold detection algorithm to decode the readout signal in the simulation. The use of this simple detector will give us an upper bound on the improvements that can be achieved by this new 2D coding scheme. More complex detection algorithms could be applied, provided that their complexity remains sufficiently low, such as low complexity Viterbi or BCJR algorithms [Wu and Cioffi, 2001]. For each simulation point, more than 15 million bits are transmitted over the 2D ISI channel with overshoot (*e.g.* figure 3.1.a). Moreover, we only assume bit-position jitter noise in the simulation, as jitter noise is the dominant noise in patterned media [Aziz et al., 2002]. In this chapter, jitter noise is assumed to be uniformly distributed in the range of  $[-J, J]$ , where  $J = \text{jitter factor} \times \Lambda$  with  $\Lambda$  the dot period.

We compare three scenarios in the simulation. In the first scenario, Scenario I, we do not use any coding scheme to combat the ISI effect. Scenario II, the 7/9 2D coding scheme from [Groenland and Abelmann, 2007] is adopted to mitigate the 2D-ISI destructive effect. Scenario III, our simple 2D coding scheme is applied to avoid the worst-case 2D-ISI effect. For hexagonal patterned media, we only compare Scenario I and III as the 2D coding scheme in [Groenland and Abelmann, 2007] is only proposed for square patterned media.

For square patterned media, three scenarios are compared under the condition of the same areal density. The choice to fix the areal bit density is due to the fact that the fabrication process of the bit patterned media determines the smallest available dot period. This is essentially different from the situation of recording on continuous media. With the same areal density, the three scenarios use the same read back pulse which is simulated based on parameters in table 3.1. The three scenarios have different effective areal density, which is the number of information bits that can be stored per unit area. Scenario I has the maximum effective areal density (*i.e.*  $115 \text{ Gb in}^{-2}$ ) followed by Scenario III (*i.e.*  $115 \times (5/6) \approx 96 \text{ Gb in}^{-2}$ ); and Scenario II has the least effective areal density (*i.e.*  $115 \times (7/9) \approx 89 \text{ Gb in}^{-2}$ ). Figure 3.4 shows the simulation results for the worst case (*i.e.* storing all “1” bits) and the regular case (*i.e.* storing random bits). As we can see from figure 3.4, the proposed 2D coding scheme has a significant coding gain in the worst case comparing to Scenario I and Scenario II (*i.e.* allowing us 6 % more jitter at a BER of  $10^{-4}$ ). For the regular case, the proposed 2D coding scheme has better immunity to jitter noise than the coding scheme from [Groenland and Abelmann, 2007] (*i.e.* Scenario II), which allows us 1 % extra jitter at a BER of  $10^{-4}$ .

For hexagonal patterned media, we only compare Scenario I with Scenario III. The code rate of Scenario III is decreased to 3/4, so it has an effective areal density of  $86 \text{ Gb in}^{-2}$ . Simulation results show that Scenario I (*i.e.* no coding) can not reach the target BER (*i.e.*  $10^{-4}$ ) even in the case of no jitter noise, but Scenario III allows a jitter factor of 18 % at a BER of  $10^{-4}$ .

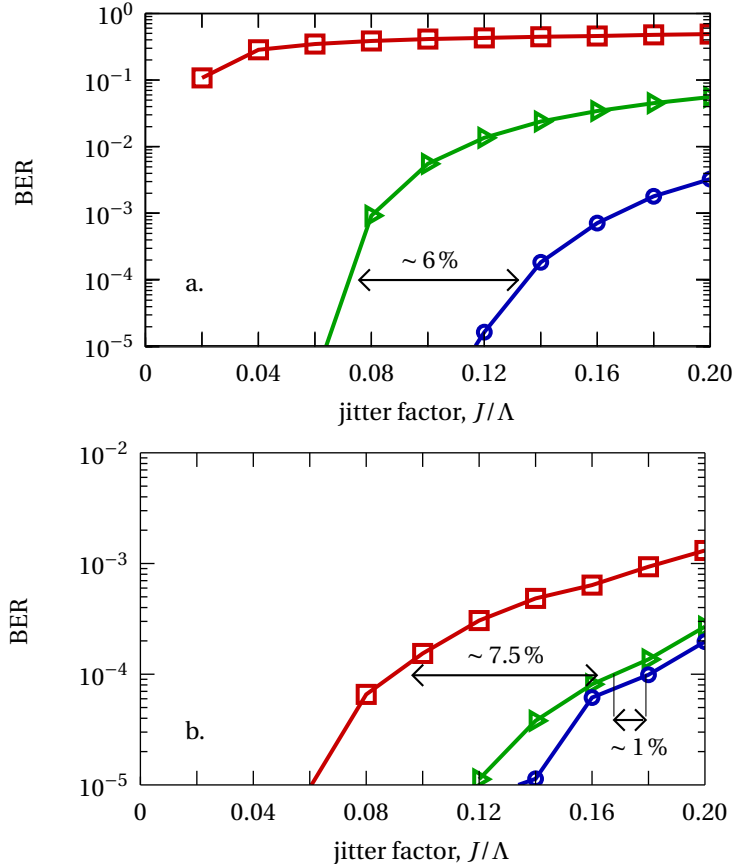


FIGURE 3.4 – Bit error rate (BER) versus bit position jitter factor of (a) the worst case by storing all “1” bits and (b) the regular case by storing random bits in square patterned media. The no coding case (Scenario I, red squares) results in large errors, especially in the worst case scenario. The 7/9 code of (Scenario II, green triangles) improves the BER; this code allows about 7.5 % more jitter at target BER =  $10^{-4}$ . The new 5/6 code (Scenario III, blue circles) is effective against the worst case patterns as it allows 6 % more jitter than the 7/9 code (in a), and 1 % in (b). The codes are compared under the condition of the same areal density.

### 3.5 Conclusions

In this chapter, a simple 2D coding scheme is proposed to combat the 2D-ISI effect that exists in bit patterned media. The basic idea of the proposed 2D coding scheme is to avoid the most destructive 2D-ISI effect which easily causes bit errors. In such a case, the signal can be decoded by algorithms which scale

more beneficial with code word length than the Viterbi detector. In the case of a simple threshold detector, we find that compared to the 7/9 2D coding scheme in square patterned media, our simple 5/6 2D coding scheme allows the bit-position jitter noise to be increased by 1 % at a BER of  $10^{-4}$ ; while it increases the effective storage capacity by around 5.5 %. With respect to the no coding case, a jitter factor of 8.5 % is allowed by the proposed 5/6 2D coding scheme. In hexagonal patterned media, the no coding case can not give us a BER of  $10^{-4}$ , even in the case without any jitter noise but our proposed 2D coding scheme allows a jitter factor of 18 % to reach this target BER.

### **3.6 Acknowledgment**

This research was supported by the Dutch Technology Foundation STW, applied science division of NWO and the technology program of the Ministry of Economic Affairs.

## Chapter 4

# Correct interpretation of tapping/liftmode MFM images of patterned magnetic islands by topography correction

### Abstract

The work described in this chapter has been done together with Hans Groenland and Leon Abelmann. We test an offline method to correct for topographic crosstalk in magnetic force microscopy (MFM) images acquired in 'liftmode', caused by variations in scan height. First, non-magnetic (e.g. electrostatic) contributions are removed via a deconvolution method. Second, a constant height MFM signal is computed from the liftmode data, by exploiting their mathematical relation. We apply the correction to experimental and simulated MFM images, acquired in two different modes. Correcting height variations properly reduces the difference between these modes by about 50%, compared to the case in which scan height variations are naively neglected. The method is useful to separate the true magnetic signal from topographic distortions.

### 4.1 Introduction

Liftmode [Giles et al., 1993] is the most popular mode of operation in ambient magnetic force microscopy (MFM) [Zhu, 2005a]. In liftmode, the separation between MFM tip and sample is kept fixed during the scanline that acquires the magnetic signal, see the tip trajectory in figure 4.1. The technique is commonly used to compensate for slow tip-sample distance changes (drift), for instance due to temperature variation. In addition, topographic cross-talk is suppressed by keeping non-magnetic forces between tip and sample more constant.

Despite the constant tip-sample separation, imaging in liftmode may still result in topographic distortion, especially on samples with significant variations in topography, for instance due to patterning. First, the tip and sample interact over an extended area ('lateral averaging' [Ziegler and Stemmer, 2011]). Thus, the tip is not only sensitive to the closest tip-sample separation, but also to local variations in the samples properties (*e.g.* topography). Second, the magnetic signal itself is measured at a varying scan height. This hinders the correct interpretation of MFM contrasts around topographic features [Chiolero and Allia, 2012; Göddenhenrich et al., 1990; Raşa et al., 2002]. Moreover, image processing [Chiolero et al., 2008, 2010; Panchumarthy et al., 2013; Takekuma et al., 2002; Yu et al., 2003], such as filtering or averaging [Chiolero and Allia, 2012; Chiolero et al., 2010; Rastei et al., 2006], on liftmode MFM images may corrupt the entire MFM data with topography. In this chapter, we investigate the effects of these scan height variations and their cancellation via offline corrections.

Typical samples with a non-flat topography are nano- or micrometer sized magnetic particles and patterned thin-film elements. These find applications in data storage, magneto-logic and (*bio*-)sensing [Stamps et al., 2014]. Via MFM, their magnetic configuration can be observed and manipulated [Amos et al., 2012]. These capabilities make MFM a useful tool to characterize prototype bit patterned media (BPM), a key technology to extend hard disk drive (HDD) recording to higher areal densities [McDaniel, 2012]. For HDD recording on BPM, as well on conventional granular media, the MFM signal may be used to determine media noises [Arnett et al., 1999; Bai et al., 2004; Glijer et al., 1996; Jiang and Guo, 2009] or even to mimic HDD read back signals after appropriate filtering [Vellekoop et al., 1999]. Imaging such nanometer sized particles at sufficient resolution, however, requires extremely small scan heights (10 nm or below) [Li et al., 2014; Piramanayagam et al., 2012]. This leads to stronger non-magnetic interactions [Yacoot and Koenders, 2008].

To extract the purely magnetic signal from MFM data, these non-magnetic forces must be canceled or avoided. Jaafar and co-workers have investigated a method in which electrical forces are nulled by combining MFM and Kelvin probe force microscopy [Jaafar et al., 2011]. The method is useful if the sample shows variations in electrical potential; these cannot be canceled by a DC tip-sample voltage. However, it does not cancel Van der Waals forces and is thus limited to scan heights where these forces are small (> 10 nm) [Porthun et al., 1998]. Another online cancellation method is switching magnetization MFM (SM-MFM)[Cambel et al., 2013]. In this method the sample is imaged twice, with alternating magnetization states of the tip. Subsequent subtraction of the two images effectively cancels all non-magnetic contributions. The *in-situ* switching of the tip [Cambel et al., 2011, 2013] requires a clever designed low coercivity tip. Ex-situ switching [Zhong et al., 2008] overcomes these requirements, but needs careful alignment of the MFM images and reproducible MFM settings.

Alternatively, signals may be offline corrected via an on/off method. The non-magnetic signal is measured in a region of the sample where the magnetic

signal is negligible (off). For this ‘3D MFM’ modes are employed. In these modes, the MFM signal is not acquired conventionally as a function of the lateral position ( $x-y$ ), but as function of the perpendicular direction  $z$  (or other parameters). The non-magnetic contribution can subsequently be canceled in regions with stray field (on), by subtracting the non-magnetic signal at the scan height concerned [Schäffer et al., 2003]. On/off methods have been used extensively to separate forces in non-contact AFM [Sweetman and Stannard, 2014] \*.

A similar method employs two MFM signals with identical topographic contributions, but magnetic contributions of opposite polarity. Subtracting the signals will effectively cancel the non-magnetic forces. We will call this the  $-1/+1$  method. The MFM signals must originate from (topographically) identical features, magnetized in opposite directions (e.g. magnetic islands or wires that are magnetized ‘up’ and ‘down’, or the alternating bits on recording media [Jaafar et al., 2008; Passeri et al., 2014]).

However, these offline methods do not take the lateral averaging effect into account. As a result, the methods are only valid in regions with identical (e.g. flat) topography.

The magnetic signal dependence on scan-height variations are governed by  $\exp(-kz)$ , the exponential decay of the stray field with height,  $z$ . This decay is wavelength ( $2\pi/k$ ) dependent and known as ‘Wallace spacing loss’ in HDD recording theory [Vellekoop et al., 1998; Wallace, 1951]. This relation was used to compare MFM images of a flat sample at different constant scan heights [Van Schendel et al., 2000]. The MFM signal at a larger scan height was successfully calculated from an MFM image taken at a smaller scan height. Similarly, the real space Green’s function representation of  $\exp(-kz)$  was tested in [Yongsunthon et al., 2002].

The  $\exp(-kz)$  transfer function may also be used to compute images at lower scan height [Che et al., 1993] or, ultimately, to infer the magnetic state of the sample or tip from the MFM data [Van Schendel et al., 2000; Vock et al., 2011]. However, this boosts high frequency noise [Saito et al., 1999]. Besides this, the magnetization is not unique; inferring the magnetization of the sample from the MFM signal cannot be done without assumptions on the samples magnetic state [Rawlings and Durkan, 2013; Vellekoop et al., 1998]. By comparing MFM images at different scan heights, no such assumptions are needed.

Our approach to correct for topographic crosstalk is to deconvolute the tip response, using a  $-1/+1$  method to extract non-magnetic forces. The convolution model takes the lateral averaging into account. We expect non-magnetic forces due to the different tip and sample materials, resulting in contact potential differences and electrostatic attraction. Subsequently, we correct the magnetic signal for scan height variations via the  $\exp(-kz)$  transfer function,

---

\*In fact, MFM and AFM, but also electrostatic force microscopy (EFM) [Gil et al., 2003] and frequency modulated Kelvin probe microscopy [Ziegler and Stemmer, 2011] measure force gradients. Therefore correction methods can be exchanged between these fields.

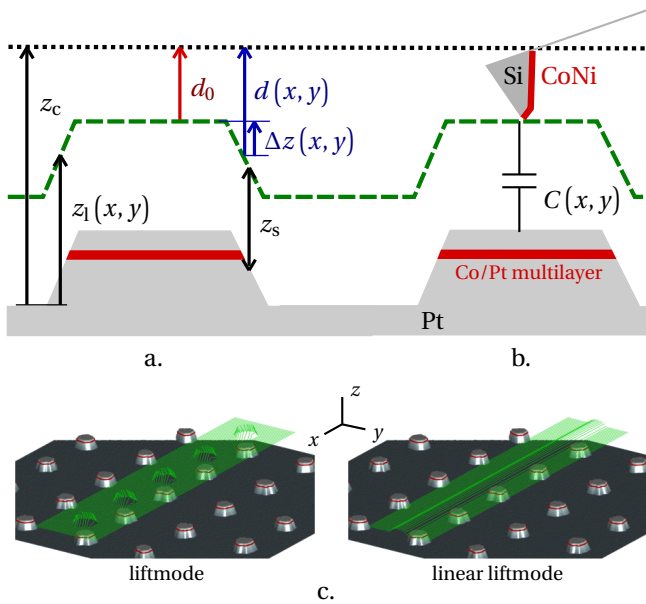


FIGURE 4.1 – (a) In liftmode the tip-sample separation ( $z_s$ ) is kept constant, resulting in a variable scan height ( $z_l(x, y)$ ) with respect to the plane of the substrate (as well as the magnetic Co/Pt multilayer (red bars)). We correct topographic distortion due to variations in scan height ( $\Delta z(x, y)$ ) by computing the MFM signal at a constant height  $z_c$  from the liftmode data. We compare the proper correction over  $d(x, y) = d_0 + \Delta z(x, y)$  to a naive correction over  $d_0$ , which neglects the variations in scan height. (b) Before correcting for scan height variations, we cancel topographic crosstalk due to non-magnetic forces, e.g. as a result of variations in tip-sample capacitance  $C(x, y)$ . (c) We correct and compare liftmode and linear liftmode MFM images of a patterned array; both their tip trajectories have a varying scan height (green lines).

to a larger constant scan height. To test the correction we applied it to images of a patterned array of islands taken in liftmode and *linear* liftmode. To show its significance, we compare the proper correction to a ‘naive’ correction, in which the scan height variations are neglected. Figure 4.1 explains the correction principles.

Liftmode is a two pass technique. The sample is raster scanned. For each scan line (in the fast scan direction,  $x$ ) the topography of the sample is obtained in the first pass, via tapping mode AFM. In the second pass, the tip is lifted to a certain height and the tip position is modulated to follow the topography, keeping the tip-sample separation constant. See figure 4.1(a).

*Linear* liftmode is similar to liftmode, except that a linear fit to the acquired topography is fed back in the MFM-pass to modulate the scan height, rather than the exact topography. This will only correct for a linear slope of the sample, unavoidable due to mounting of the sample. As a result, the average tip-sample distance is kept constant for each fast scan line. Still, variations in scan height do exist along the slow scan ( $y$ ) direction.

The outline of this chapter is as follows. Section 4.2 discusses the theory of the MFM signal (4.2.1), non-magnetic correction (4.2.2) and liftmode correction (4.2.3). Concerning the non-magnetic correction, we discuss their origin, the main contributor (*i.e.* electrostatic forces) and correction model. We assess the accuracy of the liftmode correction via simulations (4.2.4). Subsequently we describe the experimental methods in section 4.3. Results of non-magnetic and liftmode corrections are presented and discussed in section 4.4. We state our conclusions in section 4.5.

## 4.2 Theory

### 4.2.1 Magnetic force gradients

The magnetostatic energy of the tip and sample combination can be written as a convolution between the effective magnetic charge density [Hug et al., 1998; Porthun et al., 1998],  $\sigma_{m,\text{eff}}$ , and the magnetic scalar potential of the tip,  $\Phi$ , at the surface of the sample [Nutter et al., 2004]. The energy is most conveniently expressed in the Fourier domain [Hug et al., 1998]

$$U_m(\mathbf{k}, z) = \overline{\sigma_{m,\text{eff}}(\mathbf{k})\Phi(\mathbf{k}, z)} \quad (4.1)$$

$$= \overline{\sigma_{m,\text{eff}}(\mathbf{k})}\Phi_0(\mathbf{k}) \exp(-|\mathbf{k}|z), \quad (4.2)$$

with  $\mathbf{k} = (k_x, k_y) \rightleftharpoons \mathbf{x} = (x, y)$  respectively the wave vector and spatial coordinate representation of the lateral position of the tip; the overbar  $\overline{\phantom{x}}$  denotes complex conjugation. Here,  $\Phi_0$  is the tip potential in the horizontal plane at the apex of the tip (similar to the ‘ABS potential’ in hard disk recording theory [Nutter et al., 2004]) and  $z$  the separation between tip (apex) and sample. Clearly, the spatial derivatives of this energy (*i.e.* forces and force gradients) will have the same exponential dependence on  $z$  for their spectral components.

For a perpendicular magnetization of the sample, uniform over its thickness,  $t_s$ , and saturated at  $M_s$ ,  $\sigma_{m,\text{eff}}(\mathbf{k}) = \sigma_m(\mathbf{k})[1 - \exp(-|\mathbf{k}|t_s)]$ , with  $\sigma_m(\mathbf{x}) \in \{\pm M_s, 0\}$ .

In the dynamic operation mode with the cantilever driven at a fixed frequency near its resonance, the phase shift of the cantilever oscillation is approximately [Abelmann et al., 2010]

$$\Delta\phi(\mathbf{k}) = -\frac{Q}{c} \cdot F'(\mathbf{k}), \quad (4.3)$$

with

$$F'(\mathbf{k}) = -\frac{\partial^2 U_m(\mathbf{k}, z)}{\partial z^2} \quad (4.4)$$

$$= -\sigma_{m,\text{eff}}(\mathbf{k}) \Phi_0(\mathbf{k}) |\mathbf{k}|^2 \exp(-|\mathbf{k}|z). \quad (4.5)$$

This phase shift is the MFM signal. The cantilever is modeled as a second order mass-spring system and  $Q$  and  $c$  are its quality factor and spring constant, respectively. The ‘force gradient’,  $F'$ , is the derivative of the force in the direction of the motion of the cantilever, assumed to be along the  $z$ -axis. The approximations in (4.3)–(4.5), hold for small phase shifts and small oscillation amplitudes.

For larger amplitudes, the time averaged force on the cantilever should be taken into account [Giessibl, 1997]. Assuming a sinusoidal motion of the cantilever with amplitude  $a$ , the  $\exp(-|\mathbf{k}|z)$ -dependence results in an effective force gradient [Dürig, 1999; Sader and Jarvis, 2004]

$$F'_{\text{eff}} = -\frac{\partial U_m(\mathbf{k}, z)}{\partial z} \cdot \frac{2i}{a} J_1(i a |\mathbf{k}|) \quad (4.6)$$

$$= -\frac{\partial U_m(\mathbf{k}, z)}{\partial z} \cdot \text{ATF}, \quad (4.7)$$

where we call ATF the amplitude transfer function [Vellekoop et al., 1999];  $J_1$  is a Bessel function of the first kind [Abramowitz and Stegun, 1972] and  $i$  the imaginary unit. The ATF takes into account the  $z$ -derivative as well as the effective smaller tip-sample separation. Indeed,  $\lim_{a \rightarrow 0} \text{ATF} = -|\mathbf{k}|$  turns (4.7) into (4.5).

In this paper, we consider the small amplitude limit only. Interestingly though, variations in amplitude could theoretically be corrected via the ATF in the same way we compute constant height signals from MFM liftmode signals via  $\exp(-kz)$ . Prior to such corrections however, force gradients of non-magnetic origin should be avoided or canceled.

## 4.2.2 Non-magnetic force gradients

### 4.2.2.A Origins

Non-magnetic interactions [Yacoot and Koenders, 2008] that vary with tip-sample distance cause topographic cross-talk. We refer to all force gradients as non-magnetic, except for the hard ferromagnetic interaction in (4.2) *i.e.* the interaction between bodies with rigid, saturated magnetization not susceptible to a field. For typical 20 nm to 100 nm scan-heights, electrostatic forces are the main contributor [Porthun et al., 1998; Saint Jean et al., 1999; Yu et al., 2004] and dominate Van der Waals forces [Jaafar et al., 2011]. These conservative interactions <sup>†</sup> corrupt the MFM signal via their attractive force gradients. These add directly to  $F'$  in (4.3).

---

<sup>†</sup>Here we crudely regard ‘even’ interactions as conservative and ‘odd’ as dissipative forces [Sader et al., 2005]

Besides this, dissipative forces modulate the MFM signal by reducing the quality factor of the resonance, in turn affecting the oscillation amplitude of the cantilever as well as the phase sensitivity (4.3)[Whangbo et al., 1998]. As a result, position dependent dissipation will appear as a varying force gradient signal. Dissipative forces are mainly due to air damping [Sader, 1998], which depends on tip-sample separation [Proksch et al., 1999; Schäffer et al., 2003]. Magnetic dissipation via eddy currents [Hoffmann et al., 1998] or switching of the tip or sample through minor hysteresis loops [Proksch et al., 1999] are expected to have smaller effects.

Similarly, soft magnetic interactions (*i.e.* variations in magnetization of the tip and sample due to each other's stray fields) depend on scan height and may cause distortion of the MFM signal [Alekseev et al., 2014]. Proper calibration of the tip may be used to adjust for this [Weis et al., 2008]. This is not considered in this work, as we expect our sample and tip to have sufficient crystalline and shape anisotropy, respectively. Further, a non-flat response of the piezo driver may add distortion [Proksch and Kalinin, 2010].

These non-magnetic forces that modulate the signal and vary with scan height hinder comparison of MFM signals acquired at different scan heights. Their only remedy is careful tip calibration. The additive force gradients of conservative interactions can be canceled by subtraction, provided they are well estimated. Since the dominant conservative force is the electrostatic force, it is discussed in more detail below first. Subsequently, the correction for non-magnetic forces (in general) is discussed.

#### 4.2.2.B Electrostatic force gradients

We obtain the force gradients due to electrostatic energy,  $U_e$ , of the capacitive tip-sample structure, via

$$U_e = \frac{1}{2} C(\mathbf{x}) V^2 \quad (4.8)$$

$$\frac{\partial F_e}{\partial z} = -\frac{\partial^2 U_e}{\partial z^2} = -\frac{1}{2} \frac{\partial^2 C(\mathbf{x})}{\partial z^2} V^2, \quad (4.9)$$

where  $C$  is the position dependent capacitance, and  $V = \Delta\varphi + V_{\text{tip}}$  the potential difference between tip and sample, *i.e.* the sum of the difference in contact potentials between tip and sample ( $\Delta\varphi = \varphi_{\text{tip}} - \varphi_{\text{sample}}$ ) and applied tip-sample voltage.

The contact potentials are determined by the work functions of the tip and sample materials [Sze and Ng, 2007]. Values are 5.7 V for Pt, about 5 V for Co and Ni [Lide, 1995], and about 4.1 V for n-type Si (0.01 Ω cm) according to calculations [Sze and Ng, 2007]. These values result in  $\Delta\varphi \approx 1.6$  V and  $\Delta\varphi \approx 0.7$  V for the Si and CoNi layers of the tip and Pt sample, respectively. The quoted energies are however indications, since the work functions depend on preparation of surfaces of the tip and sample (*e.g.* crystal orientation, oxidation) [Allen and Gobeli, 1962]. Besides this, the ‘effective  $V$ ’ depends on the detailed shape of

the apex of the coated tip, as this shape determines whether more Si or CoNi is exposed to the sample.

An off-line correction is needed to compare MFM signals taken at different scan heights, because (I)  $V_{\text{tip}}$  cannot simultaneously cancel  $V$  for both the Si and CoNi sides of the tip, so some force gradients will always remain for side coated MFM tips. (II) In general, the capacitance does not depend on  $z$  via the transfer function  $\exp(-|\mathbf{k}| z)$  (in contrast to interactions between immobile charges). Consequently, liftmode correction does not ‘correct’ such capacitive force gradients to the capacitive force gradients at a constant height. (III)  $C$  is sensitive to the laterally averaged tip-sample distance [Ziegler and Stemmer, 2011]. This is not constant even in liftmode operation.

Alternatively, coating the tip with a thin layer of Pt cancels the electrostatic forces, at the cost of a slightly larger magnetic tip-sample distance. Nevertheless, lateral variations in  $\Delta\varphi$  or contributions of the other non-magnetic forces still need an offline correction.

#### 4.2.2.C Correction for non-magnetic forces

The electrostatic interaction, as well as Van der Waals forces [Argento and French, 1996], are well modeled by an interaction potential integrated over the volume of the tip and sample. For approximately flat samples [Gómez-Moñivas et al., 2000; Ziegler and Stemmer, 2011], the interaction is a convolution between a tip response function (determined by the tip geometry and tip-sample distance) and the geometry (*e.g.* topography, potential) of the sample [Cohen et al., 2013].

Here we consider such a convolution model for non-magnetic force gradients ( $F'_{\text{nm}}$ ). We assume a fixed tip response function ( $h_{\text{nm}}$ ) that is invariant with scan height. The relevant geometry of the sample is its topography ( $z_t$ ), as we assume other properties to be uniform. The scan height dependence is taken into account, to first order, by a term directly proportional to the scan height variations (via  $c_{\text{nm}}$ ). This yields

$$F'_{\text{nm}}(\mathbf{x}) = \left[ h_{\text{nm}} * z_t \right](\mathbf{x}) + c_{\text{nm}} \Delta z(\mathbf{x}), \quad (4.10)$$

where  $*$  denotes 2D-convolution. In discrete form, the response function and signals are images/matrices. Deconvolution of  $h_{\text{nm}}$  and  $c_{\text{nm}}$  in (4.10) requires, besides the experimental scan height, estimates of the topography and non-magnetic force gradients.

The topography equals the AFM image,  $z_t(\mathbf{x}) = \Delta z(\mathbf{x})$ , if we neglect tip convolution effects [Yacoot and Koenders, 2008]. We model noise in the AFM image as additive white Gaussian noise (AWGN) and take its power from the noise floor of its frequency spectrum. Although very small ( $\sigma_{\text{AFM, AWGN}} \approx 0.1 \text{ nm}$ ), neglecting the noise floor results in excessive high frequency noise in the deconvoluted  $h_{\text{nm}}$ . Alternatively, limiting the bandwidth of  $F'_{\text{nm}}$  could suppress high frequency noise as well.

The non-magnetic force gradients are discriminated from the MFM signal, using a  $+1/-1$  method. The islands on our sample are identically patterned,

and randomly magnetized, either up or down. So, on average, the repulsive (*i.e.* up,  $\uparrow$ ) and attractive (*i.e.* down,  $\downarrow$ ) magnetic pulses have equal magnitude. Summing the average up and down pulse effectively cancels the magnetic signal and results the average non-magnetic signal,

$$\langle F'_{\text{nm}}(\mathbf{x}) \rangle = \frac{1}{2} \left( \frac{1}{P_\uparrow} \sum_{p=1}^{P_\uparrow} S_{\uparrow,p}(\mathbf{x}) + \frac{1}{P_\downarrow} \sum_{p=1}^{P_\downarrow} S_{\downarrow,p}(\mathbf{x}) \right). \quad (4.11)$$

Here  $P_\uparrow/P_\downarrow$  are the number of up/down pulses and  $S_p$  are  $N_{\text{nm}} \times N_{\text{nm}}$  sub-images (*i.e.* windows) around the centers of the islands. The AFM data is averaged similarly and deconvolution is performed on the averaged images. This averaging does not affect the result due to linearity of the convolution operation.

Finally, we deconvolute  $h_{\text{nm}}$  and  $c_{\text{nm}}$  via mean square error minimization. This method uses the familiar auto and cross correlations estimates of MFM, AFM and noise signals [Van der Heijden, 1994]. Reconstructing and subtracting  $F'_{\text{nm}}$  from the MFM image completes the correction for non-magnetic forces.

### 4.2.3 Liftmode correction theory

In this section we discuss the liftmode correction in theory, which we will investigate further by means of simulation in the next section (4.2.4).

#### 4.2.3.A The liftmode correction

According to (4.5), the liftmode signal,  $S_l$ , is related to a constant height signal,  $S_c$ , via an inverse Fourier transform

$$S_l(\mathbf{x}) = \frac{1}{4\pi^2} \int S_c(\mathbf{k}) \exp(|\mathbf{k}| d(\mathbf{x}) + i\mathbf{k} \cdot \mathbf{x}) d^2\mathbf{k} \quad (4.12)$$

$$= \frac{1}{4\pi^2} \int S_c(\mathbf{k}) g(\mathbf{k}, \mathbf{x}) d^2\mathbf{k}, \quad (4.13)$$

where  $d(\mathbf{x}) = z_c - z_l(\mathbf{x})$  the difference between the constant and liftmode scan height (as in figure 4.1). For positive  $d$ , which we consider here, the integral exists if  $S_c$  is band limited. In practice, MFM images have finite resolution and finite size. Therefore, we approximate (4.13) by the discrete transform, as

$$S_l(\mathbf{x}_n) \approx \frac{\Delta k^2}{4\pi^2} \sum_{m=1}^{N \times N} S_c(\mathbf{k}_m) \exp(|\mathbf{k}_m| d(\mathbf{x}_n) + i\mathbf{k}_m \cdot \mathbf{x}_n), \quad (4.14)$$

where  $S_l(\mathbf{x}_n)$ ,  $d(\mathbf{x}_n)$  and  $S_c(\mathbf{k}_m)$  are the discrete signals (pixel values) at coordinates  $\mathbf{x}_n = (x, y)_n$  and  $\mathbf{k}_m = (k_x, k_y)_m$  in real space and Fourier space, respectively. For square images of size  $N \times N$  and equal sampling distance,  $\Delta x$ , along  $x$  and  $y$ , the wave vectors are separated by  $\Delta k = 2\pi / (N\Delta x)$ . We denote the sets of involved pixels by  $\mathcal{D}_x$  and  $\mathcal{D}_k$ . The latter are the wave numbers periodic with  $N\Delta x$ , *i.e.* the size of the window.

Rewriting (4.14) in matrix form gives,

$$\mathbf{S}_l = \mathbf{G}_1 \cdot \mathbf{S}_c. \quad (4.15)$$

Here the  $(N \times N)^2$  elements of  $\mathbf{G}_1$  are  $g_{n,m} \propto \exp(|\mathbf{k}_m| d(\mathbf{x}_n) + i\mathbf{k}_m \cdot \mathbf{x}_n)$ . The constant height signal is straightforwardly obtained via matrix division.

We implemented the liftmode correction in MATLAB [Mathworks, 2010], simply via  $\mathbf{S}_c = \mathbf{G}_1 \setminus \mathbf{S}_l$ . However, due to memory constraints, the correction cannot be applied on an MFM image as a whole. Therefore, we correct images using multiple smaller rectangular sub-images, or windows. In practice, a feasible window size is  $N = 69$  pixels. This window size corresponds to  $1.3\Lambda$ , for our patterned sample (figure 4.2) and experimental sampling distance.

Unfortunately though, computation errors may result, due to the finite window size and the periodic boundary conditions imposed by the Fourier series. In particular, poor estimates of the DC-level and other low frequency components are expected, since these depend on the polarity of the MFM signal (*i.e.* MFM pulses of the islands) in the window. Therefore, we consider an extended window.

#### 4.2.3.B Extended window

We improve the liftmode correction by enlarging the correction window, using an approximate solution for distant pixels: For pixels in the extended part, *i.e.*  $\mathbf{x} \notin \mathcal{D}_x$ , the variation in scan height is neglected.

The continuous equation (4.13) becomes

$$S_l(\mathbf{x}) = \frac{1}{4\pi^2} \int S_c(\mathbf{k}) g(\mathbf{k}, \mathbf{x}) d^2\mathbf{k} \quad (4.16)$$

with

$$g(\mathbf{k}, \mathbf{x}) = \begin{cases} \exp(|\mathbf{k}| d(\mathbf{x}) + i\mathbf{k} \cdot \mathbf{x}) & \text{if } \mathbf{x} \in \mathcal{D}_x \\ \exp(|\mathbf{k}| d_0 + i\mathbf{k} \cdot \mathbf{x}) & \text{if } \mathbf{x} \notin \mathcal{D}_x \end{cases} \quad (4.17)$$

For the naive correction distance we take  $d_0 = d(\mathbf{x}_0)$  where  $\mathbf{x}_0$  is above an island (figure 4.1). The matrix representation of (4.16) is

$$\mathbf{S}_l = \mathbf{G} \cdot \mathbf{S}_c. \quad (4.18)$$

Here,  $\mathbf{G}$  has size  $qN \times qN$ , with  $q$  an odd integer. We arrange its elements in a convenient form:

$$\mathbf{S}_l = \begin{matrix} \mathbf{x} \in \mathcal{D}_x \\ \mathbf{x} \notin \mathcal{D}_x \end{matrix} \downarrow \left[ \begin{array}{cc} \xrightarrow{\mathbf{k} \in \mathcal{D}_k} & \xrightarrow{\mathbf{k} \notin \mathcal{D}_k} \\ \mathbf{G}_1 & \mathbf{G}_2 \\ \mathbf{G}_3 & \mathbf{G}_4 \end{array} \right] \mathbf{S}_c. \quad (4.19)$$

Now, submatrices  $\mathbf{G}_1, \mathbf{G}_2$  account for the proper  $z$ -dependence and  $\mathbf{G}_3, \mathbf{G}_4$  for the approximation. Further  $\mathbf{G}_1, \mathbf{G}_3$  and  $\mathbf{G}_2, \mathbf{G}_4$  concern respectively  $\mathbf{k} \in \mathcal{D}_k$  and  $\mathbf{k} \notin \mathcal{D}_k$ . In this form,  $\mathbf{G}_1$  is the same matrix as in (4.15).

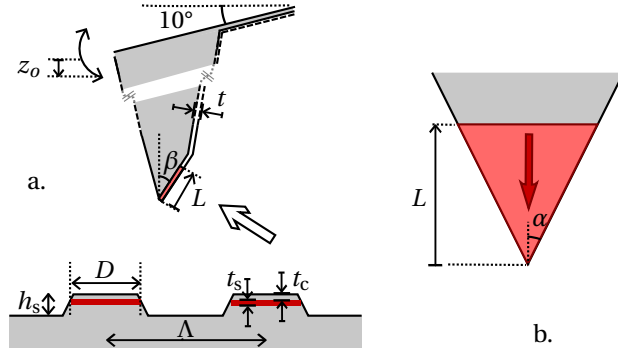


FIGURE 4.2 – *Simulation geometry of tip and sample (a); (b) shows the apex of the tip as viewed from arrow in (a); the active part of the magnetic coating of the tip (red triangle) is modeled as a triangular prism. Symbols indicate media and tip dimensions; these are explained in section 4.2.4.A.*

Briefly, the inverse of the matrix can be written in terms of the sub-matrices, of which only submatrices  $\mathbf{G}_1$  and  $\mathbf{G}_4$  need to be inverted [Zhang, 2005]. The latter is large, however its inverse can be calculated using FFTs. This holds also for  $\mathbf{G}_3$ . Applying  $\mathbf{G}_2$  on a vector is equivalent to computing a variable liftmode signal from a constant height signal, as in (4.13) (taking into account only  $\mathbf{k} \notin \mathcal{D}_k$  and discarding  $\mathbf{x} \notin \mathcal{D}_x$ ). This is similar to simulating the liftmode signal from an effective charge distribution, which method is described below.

The extended window should result in an improved estimate for low frequencies. These frequencies are hardly affected by the liftmode ( $\exp(|\mathbf{k}| d_0) \approx 1$ ), so neglecting the variation in scan-height is not expected to yield large error.

#### 4.2.4 Simulation of the liftmode correction

The remaining part of the theory section concerns simulations of the liftmode correction. The accuracy of the correction is investigated, and the naive and proper correction (see figure 4.1.a) are compared (section 4.2.4.B), using an extended window with  $q = 9$ . The effect of the extension factor  $q$  is investigated in 4.2.4.C. Care is taken to simulate realistic MFM images (section 4.2.4.A), therefore parameters and dimensions are chosen close to experimental values.

##### 4.2.4.A Simulation method

**Media** The sample (see figure 4.2) consists of an array of islands with  $\Lambda = 500$  nm periodicity. Topographically, the islands are on average truncated cones, with  $h_s = 15$  nm height, and 55 nm/80 nm radius at the top/bottom. The patterned magnetic layer is on average cylindrical, with nominal radius  $D/2 = 60$  nm and thickness  $t_s = 5$  nm. The top face of this layer is situated  $t_c = 3$  nm

below the surface of the island. The islands have fluctuating shapes, which are modeled by variations in the islands perimeter according to its experimentally obtained power spectrum in figure 2.2. These shape fluctuations affect both the topographic and magnetic geometries.

The liftmode trajectory  $z_l(\mathbf{x})$  is obtained by adding the nominal scan height ( $z_s$ ) to the AFM image, plus a  $z_o = a = 20\text{ nm}$  offset. This offset is due to the cantilever amplitude in the AFM tapping pass (*i.e.* the ‘setpoint’).

**Tip** The magnetic coating of the tip apex is modeled as a triangular prism [Van Schendel et al., 2000] with a  $t = 35\text{ nm}$  thickness,  $L = 800\text{ nm}$  height and  $\alpha = 22.5^\circ$  tip angle, defining its sharpness (see figure 4.2). The value of  $L$  was chosen such that any further enlargement has negligible effect on the MFM signal. The magnetization is uniform and directed in the plane of the coating, *i.e.* the easy axis according to shape anisotropy.

This prism is tilted by an  $\beta = 14^\circ$  in  $(x, z)$ -plane, corresponding to a  $10^\circ$  mounting angle and the specific angle of the coated plane near the apex of the tip. A 20 nm shift in the  $x$ -position of the magnetic layer accounts for the distance between the uncoated front and coated back faces of the tip. As a result, the MFM pulses are slightly asymmetric in the fast scan direction and shifted [Yu et al., 2003] in respect to the topography (AFM image), as observed in experiments.

**MFM signal** The MFM signal is simulated by evaluating (4.3);  $\Phi_0(\mathbf{k})$  is computed via analytic formulas for uniformly magnetized polyhedra [Wilton et al., 1984] and numerical FFT. Filling the shapes of the islands uniformly with either  $-M_s$  or  $+M_s$  and subsequent numerical FFT results in  $\sigma_m(\mathbf{k})$ . The force derivatives are converted to phase shift using  $Q = 400$  and  $c = 42\text{ N m}^{-1}$ . Finally, the liftmode signal follows from interpolation of constant height MFM images (at 1 nm resolution) to variable scan height,  $z_l(\mathbf{x})$ . This signal is down-sampled to a  $5\mu\text{m}/512 \approx 9.8\text{ nm/pixel}$  resolution, to mimic experimental resolutions. The tip and sample have saturation magnetizations of  $M_{s,\text{tip}} = 1100\text{ kA m}^{-1}$  and  $M_s = 800\text{ kA m}^{-1}$  respectively.

**Error to signal ratio** To compare computations errors that occur in the frequency band that contains MFM signal (*i.e.* the ‘in-band’ errors), we define an error to signal ratio (ESR) as the quotient of pulse amplitudes that result after matched filtering [Haykin, 1989], according to

$$y_c(\mathbf{x}_n) = [S_c * S_{\text{mf}}](\mathbf{x}_n) \quad (4.20)$$

$$y(\mathbf{x}_n) = [\tilde{S} * S_{\text{mf}}](\mathbf{x}_n) \quad (4.21)$$

$$\epsilon(\mathbf{x}_n) = y(\mathbf{x}_n) - y_c(\mathbf{x}_n) \quad (4.22)$$

$$\text{ESR} = \frac{1}{P} \sum_{m=1}^P \left| \frac{\epsilon(\mathbf{x}_n)}{y_c(\mathbf{x}_n)} \right| \Big|_{\mathbf{x}_n=\mathbf{x}_m}. \quad (4.23)$$

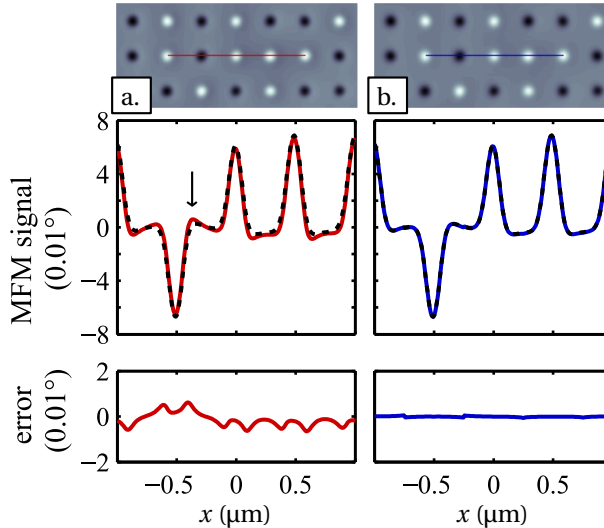


FIGURE 4.3 – Simulated naive (a) and proper (b) liftmode corrections. An MFM image at  $z_s = 40\text{ nm}$  is corrected to a constant height  $z_c = 70\text{ nm}$  image (top images). Scan lines are compared to the exact constant-height signal (black dashed lines). The naive correction (red lines) results in errors at the overshoot (arrow) of the pulses. The proper correction (blue lines) shows only small step-like computation errors (bottom).

Here  $\tilde{S}$  is the liftmode corrected signal *i.e.* the estimate of  $S_c$ . The matched filter,  $S_{mf}$ , is constructed from the signal of a perfectly cylindrical island, simulated at the scan height concerned. Amplitudes are taken at the central pixels,  $x_m$ , of the  $P$  islands.

#### 4.2.4.B Results of simulation: proper versus naive correction

We generated arrays of islands and simulated AFM and corresponding MFM liftmode ( $z_s = 20\text{ nm} + z_o$ ) and constant height ( $z_c = 70\text{ nm}$ ) images. The liftmode images are corrected using extended windows (extension factor  $q = 9$ ) around the center of each island.

Figure 4.3 shows the corrected MFM signals and constant height signal as reference. The pulses in these signals have realistic shapes (for instance, a positive main peak with negative side-peaks *i.e.* overshoot) and magnitudes ( $0.06^\circ$ ). Comparing correction methods, the naive correction overestimates the overshoot. This is not a surprise, since the overshoot is located at the edge of the island, where the naive correction assumes a too small correction distance ( $d_0 < d(\mathbf{x})$ ). This results in less attenuation of the signal. In contrast, the proper correction does reproduce the constant height signal. Its error signal shows

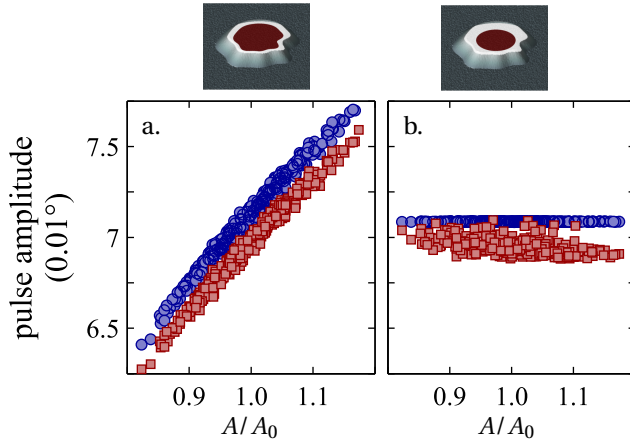


**FIGURE 4.4 – Simulated pulse amplitudes resulting from proper (blue circles) and naive (red squares) liftmode corrections ( $z_s = 40 \text{ nm}$ ,  $d_0 = 40 \text{ nm}$ , no noise) versus normalized island area. In (a) the magnetic layer has same fluctuations in shape as the island, in (b) the magnetic layer is cylindrical (e.g. top images). In (a) both corrections show an increase in amplitude with island area. In (b) the naive correction shows a decreasing amplitude for larger island areas, whereas the proper correction correctly results in a constant amplitude.**

only small steps in-between pulses. These are attributed to the limited size of the correction window, as we verified that smaller correction windows lead to larger error.

The need for a proper correction is illustrated in figure 4.4. It compares the pulse amplitudes in simulated MFM images of single islands after proper and naive liftmode correction, for two types of islands. In figure 4.4.a the magnetic layer has the same fluctuations in shape as the geometric island. Besides a small scatter, both corrections for this type of island show a similar dependence of the magnitude of MFM signal on the island's area. However, the naive correction result in smaller amplitudes. So, the overestimation of the overshoot, as in figure 4.3, also affects the pulse amplitude. In this example, the 6.5% fluctuation (standard deviation) in area results in 3.4% variation in amplitude.

In the second case (figure 4.4.b) the shape of the magnetic layer is perfectly cylindrical with constant radius  $R_0$ . The topographic shapes of the islands, which determine the simulated liftmode trajectories, have the same fluctuations as before. Such a perfect magnetic layer is physically unrealistic, however it is a simple example of a case in which the shape of the magnetic layer is decoupled from the topography of the island. Comparing corrections, the proper correction results correctly in a constant pulse amplitude, not depending on variations in area (*i.e.* shape) of the islands. For the naive correction, the amplitudes show a random scatter and, on average, decrease slightly with increasing

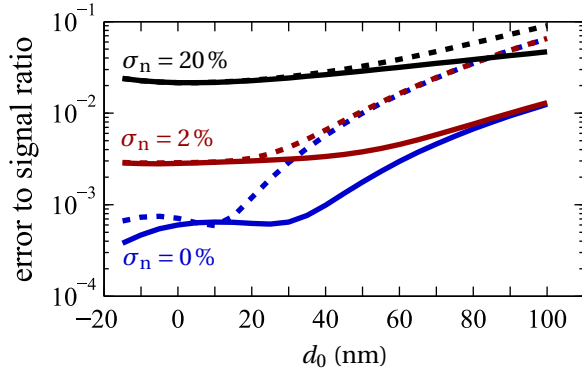


FIGURE 4.5 – Simulated error to signal ratio after a proper correction over distance  $d_0$ . Noisy MFM images simulated at  $z_s = 40$  nm are lifted over  $d_0$  without (dotted lines) and with (solid lines) extension of the correction window ( $q = 9$ ); pulse amplitudes are compared to the exact constant height signal after matched filtering. The AWGN  $\sigma_n$  is 0% (blue), 2% (red) and 20% (black) of the MFM pulse amplitude. The noiseless simulations show that computation errors occur for  $d_0 > 20$  nm if the window is not extended, which limits the error to signal ratio also in the AWGN cases. Using the extended window the computation errors are small for  $d_0 < 40$  nm. Overall, the liftmode correction is robust against noise in the bandwidth of the MFM signal: simulations with AWGN show similar computation errors as the noiseless simulations when above the  $\sigma_n$  noise floor, and even small errors for  $d_0 < 0$ .

area. The fluctuations in area now erroneously results in 0.6% variation in amplitude. Based on those amplitudes, a  $0.6/3.4 \cdot 100\% = 16\%$  relative error in (magnetic) area fluctuations would be falsely deduced comparing the slopes in figure 4.4.a and b. Although small, such an error in size jitter is readily significant in BPM recording systems [Nabavi et al., 2008] and must be avoided in media noise characterization.

#### 4.2.4.C Simulated error to signal ratio

The errors of the proper correction method are estimated using the error to signal ratio (ESR) that result after proper correction of liftmode images. A single MFM liftmode MFM image ( $10 \times 10$  islands) is simulated and corrected to various heights, over correction distance  $d_0$ . Additive white Gaussian noise (AWGN) is added to simulate cantilever and electronic noise that is always present in experimental MFM. The ESR is computed according to (4.23).

Figure 4.5 shows the ESR against correction distance. Clearly extending the window improves the ESR by a factor of about 5 for large  $d_0$ . We found only a slight improvement between window extension factors  $q = 3$  and  $q = 9$ . Fur-

ther reduction of the error must therefore be sought in larger proper correction windows,  $\mathcal{D}_x$ . The increase in error for larger  $d_0$  shows that the computation errors are made, as anticipated, in the low-frequency components, since these components become more prominent as  $d_0$  increases. In turn, high frequency noise increases for negative  $d_0$ , however, the in-band noise is not excessively boosted. Moreover, the ESR of the noisy simulations are tightly lower bounded by the ESR of the noiseless simulations, showing that the liftmode correction is robust against AWGN. Correction distances up to  $d_0 = 40\text{ nm}$  yield acceptable ESR < 0.1 % in the absence of noise.

## 4.3 Experimental

### 4.3.1 Sample

The magnetic layer was fabricated by sputter deposition of [Co(0.4 nm)/Pt(1 nm)]  $\times 5$  multilayer and 2 nm Pt cap onto a 30 nm Pt seed. The seed was sputtered onto thermally oxidized  $\text{SiO}_2$ . The layer was patterned by laser interference lithography [Luttge, 2009; de Vries et al., 2013]. A bottom anti-reflective coating (BARC) below the photoresist was used to reduce the influence of standing waves caused by reflection from the metallic layer. The photoresist was transferred into the BARC and magnetic multilayer by a subsequent  $\text{O}_2$  plasma and Ar etch, respectively. After transferring the pattern, the BARC was removed, although some BARC residue may remain on top of the islands. The patterned islands have a 14 nm height, 55 nm radius and 500 nm periodicity. This media was also investigated in chapter 2.

### 4.3.2 Magnetic force microscopy

#### 4.3.2.A MFM setup

The DI3100 (Digital Instruments) MFM was operated in liftmode and linear liftmode, at typically 20 nm and 60 nm lift height, respectively. Simultaneously with the MFM signal, the AFM signal was acquired in tapping mode. During linear liftmode also the scan heights were recorded, which showed a 6.5 nm variation between scan lines over and adjacent to the islands. Voltages between tip and grounded sample were supplied from an external source via the auxiliary input of the MFM.

Liftmode and linear liftmode images of  $5 \times 5\mu\text{m}$  at  $512 \times 512$  pix resolution were made alternatingly after a single approach. We did not correct MFM signals for nonlinearities due to ‘Bocek angle’ (*i.e.* distortion in the DI3100 lock-in amplifier) [Bocek, 2001], as the measured phase shifts were small. <sup>‡</sup>

---

<sup>‡</sup>The effect and correction of the Bocek angle are discussed in appendix C.

### 4.3.2.B Tip

Commercial micromachined, sharpened pyramidal shaped silicon (n-type,  $0.01\text{--}0.02 \Omega \text{ cm}$ ) AFM tips (SmartTip) were coated with  $\text{Co}_{\text{at.}80\%}\text{Ni}_{\text{at.}20\%}$  via evaporation. The tips were held under an angle during deposition, resulting in a 35 nm thick layer on the two back faces of the cantilever. The stiff cantilevers have  $c = 27 \text{ N m}^{-1}$  spring constant (though nominally  $42 \text{ N m}^{-1}$ ) and resonance frequencies around 320 kHz. Effective quality factors of about 446(70) (via  $Q_{\text{eff}} \equiv \partial\phi/\partial\omega|_{\omega=\omega_0} \cdot \omega_0/2\pi$ , see appendix C) with  $\phi$  and  $\omega_0/2\pi$  the phase respectively the resonance frequency of the cantilever) were found for approached tips at 40 nm to 100 nm nominal tip-sample distances.

### 4.3.3 Preliminary corrections

The raw MFM, AFM and scan-height images were corrected for a background signal and for tip positioning errors due piezo-scanner distortion and thermal drift.

The background was discriminated from the signal by masking the islands and pulses in respectively AFM and MFM images. Linear fits to this background were subtracted, in subsequently the fast and slow scan direction. A spurious signal ( $\sim 0.01^\circ$ ), due to optical interference between light reflected from the cantilever and sample, was removed by fitting and subtracting a sine function to each fast scan line.

The tip positioning errors were corrected in two steps, using AFM data. In both steps the signal is processed in a window around each island. In the first step, the positions of pixels are transformed via a 2D polynomial [Trawick et al., 2003], such that the AFM signal matches a reference image (in minimum mean squared error sense). This reference is an AFM image which has only small positioning errors. In the second step, the pixel positions of the reference AFM image are polynomially transformed to let the centers of the islands match to a fixed 2D grid with 500 nm period [Chiolerio et al., 2008]. The correction of the reference AFM image is applied to all AFM and MFM images. Local bivariate (*i.e.* 2D) 2nd-degree polynomials were used in both steps.

## 4.4 Results and discussion

In this section the correction of non-magnetic force gradients are discussed first, and thereafter the magnetic correction for scan height variations.

### 4.4.1 Non-magnetic forces

To measure the non-magnetic force gradients directly, we took non-contact images with a bare Si AFM tip, without any coating. Figure 4.6 shows sections of such images made in linear lift- ( $z = 30 \text{ nm}$ ) and liftmode ( $z = 20 \text{ nm}$ ) at various

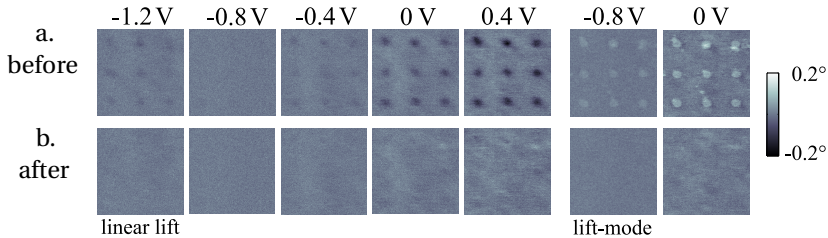


FIGURE 4.6 – Non-contact images of  $3 \times 3$  islands made with a non-magnetic Si AFM tip for various tip-sample voltages, before (a) and after (b) correction for non-magnetic force gradients. The MFM contrast is black in linear liftmode (as expected for attractive interactions), but paradoxically appears repulsive (white) in liftmode images. A  $-0.8\text{ V}$  tip-sample voltage suppresses the topographic cross-talk strongly (almost all MFM contrast vanishes, see also figure 4.7), but not entirely. Correction removes most of the signal, with some noisy MFM contrast remaining for large force gradients ( $V_{\text{tip}} \geq 0\text{ V}$ ).

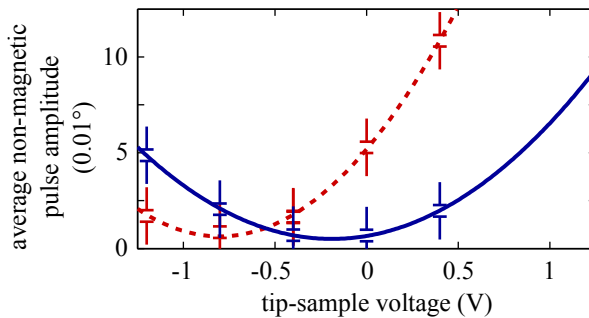


FIGURE 4.7 – Average amplitudes of the non-magnetic pulses in linear-mode MFM images made with an AFM tip at  $z = 30\text{ nm}$  (red, dashed line) and MFM at  $z = 40\text{ nm}$  (blue, solid line) tip versus tip-sample voltage. The quadratic fits (lines) through the data points show that  $-0.8\text{ V}$  and  $-0.2\text{ V}$  cancel the built-in voltages for AFM and MFM tips, respectively.

$V_{\text{tip}}$ . For small  $V_{\text{tip}}$  (decivolts) clearly observable signals were measured. The magnitude (several  $0.01^\circ$ ) is comparable to MFM signals of such islands.

As expected the linear lift images show attractive contrast. However, the force gradients in liftmode appear repulsive (*i.e.* white). This contrast inversion can be explained by variations in average tip-sample distance. Although the tip sample separation is constant, the tip-substrate distance (and so the average tip to sample distance) increases when the tip scans above an island. Because the tip-substrate distance increases, the tip-sample capacitance decreases, result-

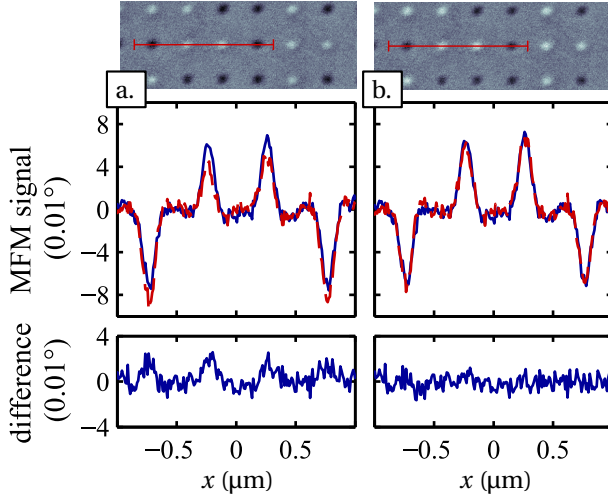


FIGURE 4.8 – Scan lines of MFM images made with  $V_{\text{tip}} = 0\text{ V}$  (blue, solid line) and  $-0.8\text{ V}$  (red, dashed), before (a) and after (b) correction for non-magnetic forces. The scan lines are averaged over the width of the pulses (11 lines). The correction results in up and down pulses with equal amplitude, and the difference (bottom) between the scan lines taken at different voltages shows no structure after correction. The MFM images for  $V_{\text{tip}} = -0.8\text{ V}$  (top) clearly show a reduction in black, attractive, contrast after correction.

ing in smaller attractive electrostatic forces. This reduction in attractive force gradient appears as a repulsive force gradient, as we take the signal when the tip is positioned above the substrate (not above the island) as reference. Clearly, the liftmode does not cancel topographic cross-talk if electrostatic forces are present.

A  $-0.8\text{ V}$  tip sample voltage suppresses most of the non-magnetic signal. This proves that the force-gradients are caused by a contact potential difference, as applying an increasing voltage to such a capacitive structure would always result in increasingly attractive interactions. The  $0.8\text{ V}$  is however significantly lower than the expected  $1.6\text{ V}$  contact potential difference between the doped Si and Pt. However, experimental deviations in work function from theoretical values have been observed before (e.g. [Allen and Gobeli, 1962]). More important, the non-magnetic signals in linear mode appear well suppressed by  $V_{\text{tip}}$ . In liftmode, however, we could not completely zero the force gradients. This indicates the presence of other non-magnetic forces.

Quantitative results are given in figure 4.7, which shows the non-magnetic pulse amplitude versus tip sample voltage. For an uncoated Si AFM tip, this pulse amplitude is the magnitude of the signal at  $30\text{ nm}$  above the center of the islands as measured in linear liftmode, averaged over 25 islands. For the MFM

tip the non-magnetic pulse amplitude resulted by averaging 27 up and 35 down pulses as in (4.11). The MFM tip measurements were taken at 40 nm in linear liftmode. The larger scan height results in a smaller capacitance, and therefore a shallower curve as compared to the AFM tip data.

As expected both curves are well fitted by a quadratic function ( $a(V_{\text{tip}} - V_0)^2 + c$ ) with constant  $c$  close to 0. The fits predict minimal force gradients for  $V_{\text{tip}} = -0.8 \text{ V}$  and  $V_{\text{tip}} = -0.2 \text{ V}$  for AFM and MFM tips, respectively. For both tips, the force gradients curves minima are not zero and cannot be completely suppressed by an applied tip-sample voltage. Possible causes could be position dependent damping, variations in work function due to BARC residue, or Van der Waals forces. Nevertheless, correcting the AFM-tip images (figure 4.6.a), for nonmagnetic forces (figure 4.6.b) shows that the force gradient can be well removed. Only for  $V_{\text{tip}} \geq 0$  some errors remain.

Similarly, we could correct MFM-tip data for non-magnetic forces, see figure 4.8. Here, the correction is applied to linear liftmode MFM images at different tip-sample voltages. Before correction, the non-magnetic forces are attractive in both images, but more attractive for  $V_{\text{tip}} = -0.8 \text{ V}$ . This results in larger amplitudes for negative (down) pulses. After correction, the signals are very similar, except for the noise, and have equal up and down pulse amplitudes as expected.

#### 4.4.2 Liftmode correction

The liftmode correction was applied to liftmode images taken at  $z = 20$  and  $40 \text{ nm}$ , and to linear liftmode images taken at  $z = 40$  and  $60 \text{ nm}$ . Prior to magnetic correction, the images were corrected for non-magnetic forces. All MFM signals were corrected to a constant  $z_c = 70 \text{ nm}$  scan height. We compare properly and naively corrected images, as was done for the simulations.

Figure 4.9 shows MFM signals after correction. As in the simulated case, the naive correction of the liftmode signal overestimates the overshoot in the pulses. The proper corrected signal reproduce well and are close to the properly corrected linear liftmode images. However, the corrected liftmode pulses show slightly smaller amplitudes. This might be caused by a smaller  $Q$  (and thus reduced phase-sensitivity) for the liftmode data, as it was taken at smaller scan-height than the linear liftmode data. A smaller scan-height reduces  $Q$  due to increased damping.

To quantify the difference between naive and proper correction, we compare pulse amplitudes in liftmode and linear liftmode images. Table 4.1 lists the average amplitude of filtered pulses after different correction steps. The pulse amplitudes are the amplitudes after applying a matched filter (derived from a simulated pulse, as in (4.23)). The amplitudes of up and down pulses are listed separately. The given  $\langle \sigma \rangle$ 's are the average standard deviation of the pulse amplitudes of individual islands. (Thus, caused by the noise in MFM images and not by the amplitude variations among islands.) Similarly,  $\langle \epsilon \rangle$  is the average standard deviation of the difference between corrected liftmode and linear liftmode pulses.

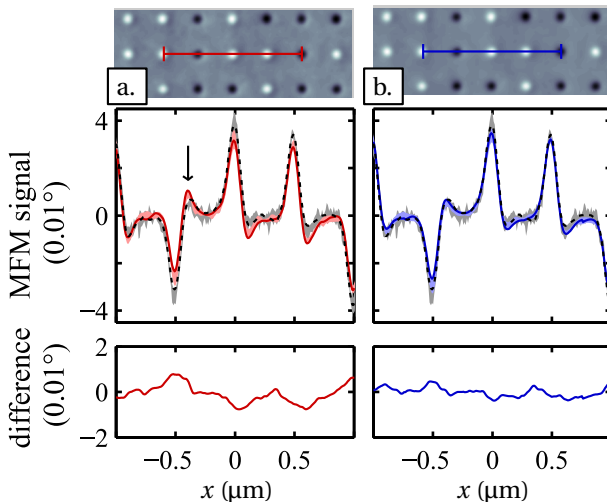


FIGURE 4.9 – Comparison of liftmode and linear mode signals, corrected to a constant height,  $z_c = 70\text{ nm}$ . The scan lines (center) are averaged over 25 lines, as indicated in the corrected MFM images (top). A naive correction (a, red solid line) results in large differences with the corrected linear mode signal (black dashed line) at the overshoot of the pulses (arrow). These differences are absent for the proper correction (b, solid blue line). The shaded areas represent the signal levels of 4 separate measurements and corrections, showing that the signals reproduce well and differences are within the noise for the proper correction.

| correction step                 | liftmode              |                               |                                 |                                   | linear lift         |                            |                                |                                  | $\langle e \rangle = \langle \sigma_{y-y_l} \rangle$ |
|---------------------------------|-----------------------|-------------------------------|---------------------------------|-----------------------------------|---------------------|----------------------------|--------------------------------|----------------------------------|--|
|                                 | $\langle y_l \rangle$ | $\langle \sigma_{yl} \rangle$ | $\langle y_{l\uparrow} \rangle$ | $\langle y_{l\downarrow} \rangle$ | $\langle y \rangle$ | $\langle \sigma_y \rangle$ | $\langle y_{\uparrow} \rangle$ | $\langle y_{\downarrow} \rangle$ |  |
| 1. background                   | 100                   | 6.5                           | 116                             | 74                                | 54                  | 3.6                        | 52                             | 56                               | n.a.   |
| 2. optical interference         | 100                   | <u>4.9</u>                    | 116                             | 74                                | 53                  | 2.7                        | 52                             | 56                               | n.a.   |
| 3. drift                        | <u>94</u>             | 4.8                           | 110                             | 69                                | 51                  | 2.6                        | 49                             | 53                               | n.a.   |
| 4. non-magnetic force gradients | 89                    | 4.7                           | <u>90</u>                       | <u>88</u>                         | 51                  | 2.6                        | 51                             | 51                               | n.a.   |
| 5.a naive liftmode              | <u>41</u>             | 2.5                           | 41                              | 40                                | 48                  | 2.4                        | 48                             | 48                               | <u>7.6</u>   |
| 5.b proper liftmode             | 45                    | 2.5                           | 45                              | 44                                | 47                  | 2.5                        | 47                             | 47                               | <u>4.1</u>   |

TABLE 4.1 – Average amplitudes  $\langle y \rangle$  and standard deviations  $\langle \sigma \rangle$  of the pulses in liftmode (subscript l) and linear liftmode images after each correction step and matched filtering. Subscripts  $\uparrow$  and  $\downarrow$  indicate respectively repulsive and attractive pulse amplitudes. The  $\langle e \rangle$  is the average of the squared difference between liftmode and linear liftmode pulse amplitudes. The signals are normalized to the amplitudes after background correction (100%). Noteworthy (underlined): Optical interference correction (step 2) reduces the variation in pulse amplitudes. The piezo drift correction (step 3) reduces the size of some islands near the start of the scan, resulting in a reduced amplitude but does not improve the deviation significantly. The non-magnetic forces correction (step 4) reduces the differences between up and down pulses for the liftmode images. The naive liftmode correction (step 5.a) results in small amplitudes, while the proper liftmode correction (step 5.b) results in amplitudes close to the proper corrected linear mode images, with a small error,  $e$ .

The table shows that the preliminary corrections are needed to make any sensible comparison between MFM images. The background varied typically over  $1^\circ$  and was corrected first (step 1). Optical interference, although hardly observable in the background corrected MFM signals, was clearly visible after the lowpass liftmode correction and matched filtering operations. Correction for this interference (step 2) reduces variance between measurements ( $\sigma_y$ ) significantly. The correction for piezo drift (step 3) reduces the size of some of the islands and as a consequence the pulse amplitudes after filtering. Surprisingly, the sigma is not altered, although we unmistakably observed such drift variations between measurements.

Correction for nonmagnetic forces (step 4) results in approximately equal up and down amplitudes, for both lift- and linear mode images. The  $\sigma$  is not affected, as expected, since the non-magnetic forces are structural errors, not varying between MFM images taken at equal scan height. As before, the sign of the non-magnetic forces is opposite for liftmode and linear liftmode images, and their magnitude is relatively smaller for linear liftmode images.

Liftmode corrections (step 5) of liftmode images result in smaller amplitudes for the naive correction compared to the proper correction. We also observed this in simulations. For linear liftmode image, there is only a small difference between proper and naive correction, because the scan height variations are relatively small. Amplitudes in corrected liftmode and linear liftmode images have almost equal standard deviations.

A smaller difference,  $\epsilon$ , between corrected liftmode and linear mode pulse amplitudes is found for the proper correction (step 5.b), compared to the naive correction (step 5.a). This is in accordance with simulations and the experimental scan lines in figure 4.9. For the proper and the naive correction,  $\epsilon$  is 9% and 16% of the corrected linear liftmode amplitude, respectively.

Overall, the comparison of naive and proper corrections show, as in simulations, that neglecting scan height variations lead to errors both in pulse amplitude and overshoot if filters are applied.

#### 4.4.3 Discussion

Imaging of patterned structures results in unwanted nonmagnetic force gradients both for liftmode and linear lift operation modes. The 2D convolution model is simple, yet effective in removing non-magnetic force gradients. However, it is only applicable for samples with islands that have identical magnetic features. For other samples, cancellation of non-magnetic forces needs accurate modeling and calibration or an SM-MFM imaging mode. We suspect that air-damping depends on scan-height, which modulates the MFM sensitivity through modulation of the quality factor of resonance. This effect may be corrected if the cantilever oscillation amplitude is measured during imaging [Whangbo et al., 1998].

The proper liftmode corrected signals compare well. However, many corrections are needed to compare signals at different scan heights. It is unclear

whether these corrections distort the MFM signal. Nevertheless, the resulting liftmode corrected signals reproduce well. The comparison could however benefit from an estimate of the errors introduced in the correction steps. Unfortunately, accurately estimating errors in the important low frequency (large wavelength) components requires imaging of very large sample areas.

Besides this, we showed that liftmode correction can be improved by taking into account larger windows. In our method, the size of the window is limited by the memory available in the simulation computer. Fortunately, there are other methods more suitable to solve large magnetostatic problems, such as the fast multipole method [Cheng et al., 1999]. Similarly to our extended window approach, this method relies on approximate solutions for distant pixels.

We found that the scan height variations cause errors mainly in the overshoot of the pulses, and occur at the edges (*i.e.* perimeters) of the islands. The errors are small compared to the pulse amplitudes, which are related to the size (*i.e.* area) of the islands. We therefore expect that relatively larger errors occur if the island size is reduced, as smaller islands have a larger perimeter/area ratio.

To extrapolate our findings to other patterned samples, we may consider our dimension normalized to the island radius. These are  $\Delta z = 0.27R$ ,  $z \approx 0.7R$ . Scaling down for instance to future patterned media with an areal density of  $10 \text{ Tb/in}^2$  ( $\Lambda = 8 \text{ nm}$ ,  $R=4 \text{ nm}$ ), equivalent scan height variations are  $1 \text{ nm}$  at  $3 \text{ nm}$  tip-sample distance. Such small tip-sample separations may be needed for imaging at sufficient resolution [Li et al., 2014; Piramanayagam et al., 2012]. An offline correction tool for such small variations in scan height is desirable for quantitative MFM on patterned structures.

## 4.5 Conclusions

We corrected tapping/liftmode MFM signals of a patterned array of magnetic islands to constant scan height signals, thus removing the topographic distortion due to variations in scan height. The corrected signals compare well with linear mode MFM images; the difference in pulse amplitudes is only 9%, which is about half of the 16% difference that results if the variation in scan height is naively neglected. In both experiment and simulation this naive correction leads to overestimation of the overshoot of the MFM pulses, and causes indeed topographic distortion in simulated pulse amplitudes.

Besides purely magnetic topographic distortion, work function differences between tip and sample cause observable non-magnetic force gradients. For an MFM tip, a  $-0.2 \text{ V}$  tip sample voltage partly suppresses these force gradients. By deconvolution of a non-magnetic tip response these force gradients were effectively removed, resulting in equal amplitudes between attractive and repulsive pulses.

The low-pass characteristic of the liftmode correction reduces the noise, but also the SNR for large  $d_0$ . Besides this, a computation error is caused by the limited number of pixels taken into account. Extension of the window using an

approximate solution for distant pixels reduces this error. Good error to signal ratios (0.1%) are obtained for correction distances up to  $d_0 = 40\text{ nm}$ .

The proper correction for scan height variations is necessary to extract the true magnetic signal from MFM images, and especially important in cases involving image processing and filtering, which otherwise would be corrupted by topography.

## 4.6 Acknowledgment

I and my colleagues would like to thank M. Siekman for technical assistance, and M. Delalande and J. de Vries for preparation of the sample. This research is supported by the Dutch Technology Foundation STW, applied science division of NWO and the technology program of the Ministry of Economic Affairs.



## Chapter 5

# Angular dependence of the switching fields of individual Co/Pt islands in a patterned array

### Abstract

I did the work described in this chapter together with Martin Siekman, Hans Groenland and Leon Abelmann. We report a remarkable difference in reversal mechanism among  $D = 70\text{ nm}$  magnetic Co/Pt-multilayer islands in an identically patterned (ion-milled) array, revealed by the angular dependent switching fields of individual islands measured using magnetic force microscopy. We find modes between coherent rotation and domain wall movement, which we quantify using modified Kondorsky functions. Most remarkable, weak islands (easy switchers) show reversal dominated by domain wall depinning, which gradually becomes more nucleation dominated for increasingly stronger islands. A two-step reversal process of nucleation and subsequent domain wall propagation explains this trend qualitatively.

### 5.1 Introduction

One of the biggest challenges in the application of patterned magnetic elements for data storage is to obtain a sufficiently small variation in switching fields between magnetic islands [Richter et al., 2006]. For bit patterned hard disk media [White, 1997] as well as magnetic random access memories (MRAM) [Parkin et al., 1999] care should be taken that weak islands are not accidentally reversed when neighboring strong islands are written.

There are several possible reasons behind broadening of the switching field distribution (SFD) of sub-micrometer-sized magnetic islands, such as defects, island size variations, stray and thermal fields [Lau and Shaw, 2011]. Different dominating switching mechanisms have been identified for different patterned

arrays [Belle et al., 2007; Shaw et al., 2008; Thiagarajah et al., 2014; Thomson et al., 2006]. In this chapter we show that in addition, identically patterned islands can have a distribution in their reversal mechanism.

Small magnetic elements are commonly patterned out of films with strong perpendicular anisotropy (*e.g.* CoPt, CoPd and FePt multilayers or alloys), to ensure their binary and stable magnetization. Good understanding of the reversal processes of such islands is essential in narrowing down the SFD, and has attracted ample research [Lau and Shaw, 2011].

The reversal of islands with dimensions several times the exchange length involves rotation of its magnetic moment via an incoherent mode. In this mode, first the magnetization of a small volume coherently rotates. Next, to attain complete reversal of the island, this nucleated domain expands via propagation of the domain wall *i.e.* the boundary between reversed and non-reversed volumes. The nucleation initiates at defects; regions where anisotropy is reduced or where the anisotropy axis is tilted from the preferred (perpendicular) axis.

Two types of defects can be distinguished. There will be intrinsic defects, readily present in the film before patterning. These intrinsic defects will be uniformly distributed over the interior of the islands after patterning. Next there might be extrinsic defects, resulting from an ion milling [Shaw et al., 2008] or ion irradiation [Hasegawa et al., 2008] process needed to magnetically isolate the islands. These extrinsic defects are typically located at the edges of the islands. Extrinsic defects can however be avoided by depositing the magnetic layer on a prepatterned substrate [Moritz et al., 2002]. Here a array of pillars, patterned before magnetic layer deposition, defines the geometry of the islands and ensures their magnetic isolation, as a result of shadowing effects.

The absence or presence of extrinsic edge defects yields two distinct switching behaviors [Shaw et al., 2008]. This allows us to roughly classify patterned arrays by their fabrication method (*i.e.* ‘prepatterned’ or ‘ion milled/irradiated’). Prepatterned islands typically have increasing switching fields for smaller islands [Thomson et al., 2006]. Nucleation dominates their reversal. Their SFD can be explained by intrinsic anisotropy defects [Shaw et al., 2010; Thomson et al., 2006]. On the contrary, ion-milled islands show different and less understood behavior, like smaller dependence on island size, and even smaller switching fields for sufficiently small islands [Belle et al., 2007; Lau et al., 2011; Shaw et al., 2008]. Depending on the demagnetization field [Mitsuzuka et al., 2007; Pfau et al., 2014] a damaged edge could nucleate readily at relatively low fields [Adam et al., 2012]. Instead of nucleation, domain wall propagation may dominate the reversal if the wall is hampered by pinning sites [Delalande et al., 2012; Lau et al., 2011].

The dominating switching mechanism could be derived from the energy barrier that inhibits switching. Nucleation and depinning barriers have distinct dependencies on the applied field. Experimentally, the barrier height is determined by the statistical fluctuations of the switching fields [Engelen et al., 2010; de Vries et al., 2013], or by the dependence of the switching fields on temperature [de Vries, 2013; Okamoto et al., 2008; Shaw et al., 2008] or applied

field duration [Adam et al., 2012; Mitsuzuka et al., 2007; Okamoto et al., 2008; Springer et al., 2011; Tudosa et al., 2012]. These experiments are all challenging and, on their own, possibly not decisive [Adam et al., 2012; Engelen et al., 2010; de Vries et al., 2013].

Alternatively, the dominating switching mechanism can be derived from the dependence of the switching field on the angle of the applied field with respect to the anisotropy axis. A Stoner-Wohlfarth (SW) [Stoner and Wohlfarth, 1948] angular dependence indicates nucleation dominated reversal, whereas a Kondorsky dependence [Kondorsky, 1940] hints at domain wall depinning dominated reversal. We discuss both mechanisms below (Section 5.2). Prepatterned islands typically have an SW dependence, although with a less pronounced minimum switching fields compared to ideal SW behaviour. Such shallow minima could possibly be explained by an anisotropy axis distribution [Hu et al., 2005b] or finite temperature [Saharan et al., 2011]. Ion milled media may exhibit even less pronounced minima [Delalande et al., 2012; Li et al., 2012; Pei et al., 2011; Shaw et al., 2008] and a more Kondorsky-like reversal modes. Pure Kondorsky reversal is observed for films or for islands in which nuclei were induced prior to switching [Delalande et al., 2012; Lau et al., 2011]. By introducing and depinning such pre-induced nuclei, the depinning and nucleation fields could be extracted. This suggests that different switching mechanism play a role for different angles of the applied field.

On a macroscopic scale (averaging over many nanoscale elements) switching fields and their distributions have been measured using vibrating sample magnetometry (VSM) [Coffey et al., 2002], magneto-optic Kerr effect (MOKE) [Hu et al., 2005a], superconducting quantum interference device (SQUID) magnetometry [Goll and Bublat, 2013] and the anomalous Hall effect (AHE) [Lau and Liu, 2012]. Island to island variations in angular dependence are however easily overlooked using these macroscopic methods. Yet, such variations likely exist. Defects in weak and strong islands (*i.e.* the islands that have respectively low and high switching fields in the distribution) were found to take different positions [Pfau et al., 2011]. This severely impacts the sensitivity of the defect to the applied field angle [Shaw et al., 2010]. Switching fields of individual islands can however be determined by microscopic AHE (by monitoring a few weak and strong islands in the distribution [Engelen et al., 2010; de Vries et al., 2013]), MOKE [Adam et al., 2012], x-ray holography [Pfau et al., 2011], magnetic force microscopy (MFM) [Li et al., 2011; Luo et al., 2008; Pei et al., 2011] and hard disk drive based setups [Springer et al., 2011].

Care must be taken to distinguish between intrinsic and extrinsic SFDs. The SFD is intrinsic if it is not influenced by the islands environment (*e.g.* not affected by dipole or exchange interactions [Thiyagarajah et al., 2014]). This is the case if there are large spacings between magnetically well isolated islands. Otherwise, a  $\Delta H(M, \Delta M)$  method [Berger et al., 2006; Hellwig et al., 2007] may be used to extract the intrinsic from an extrinsic SFD.

In this chapter, we investigate the switching mechanisms of individual islands in a single patterned array via the angular dependence of their intrinsic

switching field, measured by MFM. We report a remarkable difference in the angular dependent switching fields among islands and, moreover, a trend from domain wall propagation dominated to nucleation dominated switching from weak to strong islands. Thus far, such differences in switching mechanism have only been found for islands fabricated in different processes [Shaw et al., 2008; Thiagarajah et al., 2014] or with considerable variations in size [Kikuchi et al., 2008; Krone et al., 2011]. This effect can be explained qualitatively by a transition from nucleation field to depinning field dominated reversal, in-line with Refs [Delalande et al., 2012; Dittrich et al., 2005; Hu et al., 2005b; Lau et al., 2011].

Section 5.2 reviews the models for the angular dependence of the switching field. Section 5.3 describes our experimental methods. Results and their discussion are presented section 5.4 and conclusions in section 5.5.

## 5.2 Theory

We discuss the theoretical background on the reversal mechanisms of thin film elements (*i.e.* cylindrical islands) that are strongly exchange coupled and have perpendicular uniaxial crystalline anisotropy. Angle  $\theta$  is the applied field angle, where  $0^\circ$  denotes the direction perpendicular to the substrate of the sample. We discuss two simple models for the angular dependent switching field in the limiting cases of very small (Stoner-Wohlfarth) and large (Kondorsky) islands, and the intermediate situation.

### 5.2.1 Reversal mechanisms

#### 5.2.1.A Coherent rotation

Exchange coupling cause small islands to be in a single domain state, *i.e.* all magnetic moments (macro spins) point into the same direction. This single domain state is maintained during reversal; the moments rotate coherently. A theoretical particle for which the magnetic anisotropy is fully determined by its (first order) uniaxial crystalline anisotropy can be described by the Stoner-Wohlfarth model [Stoner and Wohlfarth, 1948]. The field needed to switch such a particle (without thermal assistance, *i.e.* at 0 K) varies with applied field angle according to

$$H_{\text{S,SW}}(\theta) = \frac{H_{\text{S}}(0^\circ)}{\left[\cos^{\frac{2}{3}}(\theta) + \sin^{\frac{2}{3}}(\theta)\right]^{\frac{3}{2}}}. \quad (5.1)$$

Here  $H_{\text{S}}(0^\circ) = H_{\text{K}}$  is the anisotropy field, and  $\theta$  the angle between applied field and the easy axis of the particle. This angular dependent switching field has its minimum at  $\theta = 45^\circ$ . Magnetic islands behave as SW particles if their size is sufficiently small, *i.e.* with dimensions comparable to the exchange length [Hubert and Schäfer, 1998]. For our media, the exchange length is 4 nm [de Vries, 2013].

### 5.2.1.B Domain wall propagation

The other extreme in reversal is found in islands that are so large that they behave like a continuous thin film, typically  $> 5\text{ }\mu\text{m}$  [Hu et al., 2005b]. Such films typically have a domain structure at remanence. Magnetisation reversal in these films takes place via the growth of domains with the magnetization oriented parallel to the field. These domains consume the non-reversed, anti-parallel, domains via propagation of the domain walls. In the Kondorsky model [Kondorsky, 1940; Schumacher, 1991], domains are magnetized along easy axes, and are separated by ideal  $180^\circ$  domain walls. The force on the wall is proportional to the field component parallel to the easy axis, thus proportional to the cosine between the field and magnetization. Pinning sites may prohibit domain wall propagation. The force needed to overcome the pinning barriers results in an angular dependence of the switching field according to

$$H_{s,\text{Kondorsky}}(\theta) = \frac{H_s(0^\circ)}{\cos\theta}, \quad (5.2)$$

where  $H_s(0^\circ)$  is determined by the barrier height of the particular pinning in the film. This formula is known as the Kondorsky function.

### 5.2.1.C Nucleation and domain wall movement

The islands in this study are of intermediate size. They are too big to switch coherently, and too small to facilitate reversed domains at remanence. So, neither the SW nor the Kondorsky model describes their reversal entirely. Switching is believed to follow a two step process, resulting in a ‘mixed switching mechanism’. First a small domain nucleates by coherent rotation. Second, this domain grows via domain wall movement. If the nucleation field is large enough to overcome all pinning sites, the whole island switches at once. In that case, the nucleation field determines the switching field. If on the other hand a higher field is needed to overcome domain wall pinning, the depinning field sets the switching field. In case the field is not sufficient to overcome depinning, the nucleated domain may either collapse back to the initial, non-reversed, single domain state (and thus not switch at all) when the field is turned off, or remain in a multi- (*e.g.* two) domain state.

Because the two mechanisms have distinct angular dependencies, we expect  $H_s(\theta)$  to be determined by a combination of (5.1) and (5.2), whichever yields smallest  $H_s$ . Since depinning fields increase with  $\theta$ , we expect depinning to dominate at larger field angles. On the other hand, nucleation will most likely dominate at smaller angles. For nucleation, the minimum in the switching field will be near  $\theta = 45^\circ$ . The crossover angle between the two switching mechanisms depend on the exact nucleation and depinning fields and will vary between islands.

The discussion above concerns switching fields at 0 K, *i.e.* the fields reducing the energy barrier to zero, sufficient to switch an island without assistance

by thermal fluctuations. Our experiments are however conducted at room temperature with finite durations of the field pulses (1 s). This lowers the switching fields considerably from their 0 K value [de Vries, 2013]. Besides this, thermal fluctuations require that switching fields must in principle be treated as stochastic quantities. Nevertheless, we use the 0 K SW and Kondorsky models as a guide to qualitatively discriminate between dominating switching mechanisms.

### 5.2.2 Shape of switching fields

#### 5.2.2.A Angular dependence of individual islands

Schumacher [Schumacher, 1991] proposed a modification of the Kondorsky function which allows for angular dependencies that continuously vary between a domain wall depinning shaped function and a coherent rotation shaped function. The modification involves the ‘shape parameter’  $h$ . The modified Kondorsky function (presented here in a simpler form) is the solution for  $H_s$  to

$$\sin(\Psi) = \frac{H_s}{H_s(0^\circ)} h \sin(\theta) \quad (5.3)$$

$$\tan(\Psi) = \frac{h \tan(\theta)}{1 - (\Psi - \frac{\pi}{2}) h \tan(\theta)}. \quad (5.4)$$

In this set of equations,  $H_s(0^\circ)$  and  $h$  are (fitting) parameters. Solving (5.4) for angle  $\Psi$  (either graphically or numerically) and substituting its value in (5.3), yields  $H_s$  as a function of  $\theta$ . In the limit of  $h = 0$ , the modified Kondorsky function equals (5.2), the Kondorsky function. In the upper limit,  $h = 1$ , the modified Kondorsky function takes a SW like form, however, with a shallower minimum of  $0.60 \times H_s(0^\circ)$  at  $48.0^\circ$ , instead of  $0.5 \times H_s(0^\circ)$  at  $45^\circ$ .

The modification of Schumacher takes into account tilted magnetic moments in the domain wall propagation theory of Kondorsky. The shape parameter is related to magnetic properties of the film. However, in this thesis (which concerns patterned islands and not domain structures in thin films) the modified Kondorsky functions are used only to conveniently describe the shape of the angular dependence of the switching fields. We make no claims about the validity of Schumacher’s model concerning the switching of small islands.

#### 5.2.2.B SFD of an ensemble of islands

We present switching field distributions as cumulative distributions. Typically these distribution have asymmetric tails, *i.e.* more islands have switching fields below the mean of the distribution than above. Such behaviour is not adequately modeled by a normal distribution. A much better representation is obtained by a cumulative 3-parameter Weibull distribution [Weibull, 1951],

$$\Pr(H_s \leq H) = \begin{cases} 0 & \text{for } H \leq H_0, \\ 1 - \exp\left(-\left[\frac{H-H_0}{\eta}\right]^\beta\right) & \text{otherwise.} \end{cases} \quad (5.5)$$

The parameters  $\eta$ ,  $\beta$  and  $H_0$ , control respectively the scale, skewness (*i.e.* asymmetry) and location (*i.e.* onset) of the distribution. The median and 10%-to-90% width of the distribution are respectively  $H_{50\%} = \eta(\ln 2)^{1/\beta} + H_0$  and  $\Delta H = \eta \left[ (\ln 10)^{1/\beta} - (\ln 10/9)^{1/\beta} \right]$ . The distribution is nearly symmetric ( $H_{50\%} = \langle H \rangle$ ) for  $\beta = 3.4$ . This convenient distribution is however, to our knowledge, not directly related to the physics of the switching of islands and used only phenomenologically\*.

### 5.2.3 Intrinsic switching fields

Stray fields of neighboring islands may broaden the SFD. Based on the geometry of the islands and the saturation magnetization of the sample,  $M_s$ , we calculated the maximum stray field to be only  $0.2 \text{ kA m}^{-1}$ . This is the field for the worst case, DC magnetized, state of the sample. This is very small compared to the  $\sim 100 \text{ kA m}^{-1}$  width of our SFDs. So, dipolar broadening of the SFD is negligible *i.e.* the distributions we present are intrinsic SFDs.

## 5.3 Methods

### 5.3.1 Sample fabrication and properties

#### 5.3.1.A Fabrication

Details of the fabrication process can be found in [de Vries, 2013]. Briefly, the Co/Pt multilayer [Co(0.4 nm)- Pt(1 nm)] $\times 5$  stack capped by Pt(3 nm) was deposited on a Pt(30 nm) base layer on a SiO<sub>2</sub> seed via magnetron sputtering. A top and bottom anti-reflective-coating (BARC) and photoresist were spin coated for laser interference lithography. The developed pattern was transferred into the magnetic stack by O<sub>2</sub>-plasma and Ar ion etching. The resulting islands have a  $\Lambda = 300 \text{ nm}$  periodicity and on average  $D = 70 \text{ nm}$  diameter, although their shape fluctuates from island to island (see chapter 2).

Removal of BARC layer needed a mechanical strip. This was done by applying and peeling-off an adhesive foil. We found that accidentally some BARC remained, resulting in columnar like structures on top of the islands. This limited the minimum tip-sample distance in MFM imaging to about 100 nm. Besides this, some islands (see figure 5.1) are not at the their ideal lattice position. We expect those islands have resulted from broken-off photoresist and BARC layers during ion beam etching. This caused unintentionally masked and exposed areas.

---

\*Though, the distribution is related to weakest link statistics [Weibull, 1951] which is the essence of the switching model of Thomson *et al.* [Thomson et al., 2006]

### 5.3.1.B Magnetic properties

A saturation magnetization of  $M_s = 450 \text{ kA m}^{-1}$  and effective anisotropy constant of  $240 \text{ kJ m}^{-3}$  were determined using torque and vibrating sample magnetometry for a similar continuous film [de Vries, 2013].

### 5.3.2 Magnetic force microscope

A centimeter sized home-built vacuum MFM was used to image the sample. The MFM was situated in between the pole shoes of a water cooled electromagnet. The MFM can be rotated freely around its axis, which allowed us to apply fields at arbitrary angle.

Due to alignment errors, a small deviation in field angle is possible. We estimate the systematic uncertainty in field angle  $< 5^\circ$ . The relative error in the angle is negligible. We determined SFDs at  $0^\circ, 10^\circ, 30^\circ, 45^\circ, 60^\circ, 80^\circ$  and  $180^\circ$  field angles.

### 5.3.3 Measurement procedure

Direct current demagnetization (DCD) curves were measured at remanence using the in-field MFM. The sample was initially DC magnetized in a  $480 \text{ kA m}^{-1}$  field. Subsequently the field was ramped up in a stepwise fashion. Fields were applied for the duration of 1 s. Images were taken in between steps, with the field turned off.

The field was automatically controlled using a Gauss meter and feedback loop. The set fields were slowly approached to avoid a possible overshoot in field ( $< 1 \text{ kA m}^{-1}$ ). The same procedure to set the fields was used, so the field values and durations were identical for the SFD measurements at various angles.

Images were taken at  $512 \times 128$  (fast  $\times$  slow) resolution. Acquisition times were about 6 minutes per image, which is a good compromise between image quality and the practical feasible number of images (field steps) to take. The images presented here have been upsampled (*i.e.* interpolated) to obtain equal resolution in fast and slow scan direction. Prior to upsampling, the images were corrected for distortions due to piezo non-linearity and slow drifts in background.

Before imaging, the MFM tip was magnetized in a small  $12 \text{ kA m}^{-1}$  field. We did not observe any signs of this field, or the field of the tip, influencing the magnetization of the sample.

### 5.3.4 Fitting procedure

The  $h$  and  $H_s(0^\circ)$  parameters of the modified Kondorsky functions were fitted to the angular dependent switching fields of individual islands, using maximum likelihood estimation. This involves the conditional probability that  $H_s(\theta)$  (according to the model) given parameter  $h$  and  $H_s(0^\circ)$  falls into the bin (*i.e.* range

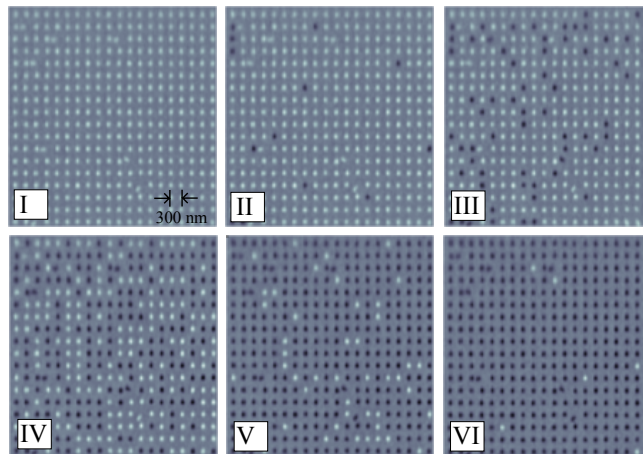


FIGURE 5.1 – MFM images used to determine the SFD by counting the number of reversed islands (*i.e.* black dots). In this series, fields are applied perpendicular to the sample ( $\theta = 0^\circ$ ). Example images (I-VI) are shown for fields from  $140 \text{ kA m}^{-1}$  to  $340 \text{ kA m}^{-1}$  in steps of  $40 \text{ kA m}^{-1}$ . Fields were turned off before acquisition of the images.

of fields between applied field steps) that was measured. We take (*e.g.* thermal) fluctuations in the switching field of an island into account via a normal distribution of  $H_s$  of the island, with  $\sigma = 3 \text{ kA m}^{-1}$ , around its mean value (justified below). As a result, this conditional probability, otherwise taking non-zero values only for the range of fields in the bin, is extended with tails, *i.e.* it includes the possibility that an island switches outside the bin to which its switching field on average belongs. A non-linear maximization routine in MATLAB [Mathworks, 2010] was used to find the parameters that yield the maximum likelihood.

## 5.4 Results and discussion

### 5.4.1 Determination of switching fields

Figure 5.1 shows example MFM images in a series taken at  $0^\circ$  field angle, *i.e.* perpendicular to the sample. In the applied field range the islands switch from all up to all down (*i.e.* white and black MFM signal, respectively). In this series of images there is a clear contrast between up and down islands, indicating all islands are in a single domain state.

At  $80^\circ$  angle of the applied field, however, some of the dots lose contrast, and show signs of white as well as black areas, see figure 5.2. We attribute this to multi-domain states, which are known to exist in islands of this material when the field is applied under large angles [Delalande et al., 2012]. The multi-domain states loose contrast due to the limited resolution of the MFM at this

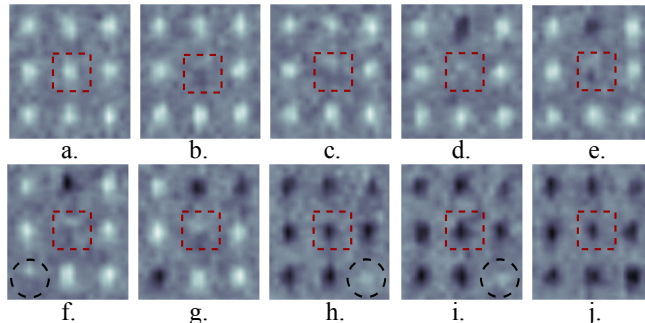


FIGURE 5.2 – Close ups of MFM images taken after applying fields with increasing strength at  $80^\circ$  field angle showing the existence of stable multi-domain states. The applied fields range from  $180 \text{ kA m}^{-1}$  (a) to  $360 \text{ kA m}^{-1}$  (j) in  $20 \text{ kA m}^{-1}$  steps. The central island (boxed) has varying MFM contrast; initially white (a) then gray (b-g) and finally black (h-j), corresponding to single, multi and reversed single domain states respectively. Similarly, other multi-domain states (encircled) are identified by their reduced MFM contrasts.

scan height. As a result, the resolution of the images is too low to determine the exact domain configuration. Moreover, it is possible that we misinterpreted single and multi-domain islands. However, we observed only a small number of islands in a multi-domain state, exclusively in the  $80^\circ$  series of measurements. Therefore, in the following we ignore possible errors made in the determination of the magnetic states of the islands.

Since the islands were imaged in remanence (*i.e.* at zero applied field), the multi-domain states are stable. The multi-domain states may ‘survive’ over several increments of the field before finally switching to the single domain state, see *e.g.* the central island in figure 5.2. However, the exact domain configurations may vary in between field steps, since the grayish contrast fluctuates. We take the field at which an island fully reverses to the saturated state as its switching field.

Besides this, because we observed multi-domain states at remanence, we can conclude that at least for some islands switching is dominated by domain wall depinning at large field angles.

#### 5.4.2 Switching field distributions

The cumulative SFDs in figure 5.3 were obtained by counting the number of up and down islands. In the  $80^\circ$  distribution also the occasional islands in multi-domain state (7%) were counted. These multi-domain islands vanish at high fields, so all islands end up in a single domain state. The resulting distributions are skewed: they are slightly asymmetric concerning their low and high field tails. We found that Weibull distributions fit well to these SFDs, although a little

TABLE 5.1 – Weibull parameters (5.5) fitted to SFDs in figure 5.3. The median ( $H_{50\%}$ ) is minimum at  $45^\circ$  and large at  $80^\circ$ . The 10%-to-90% width ( $\Delta H$ ) shows a similar trend, resulting in approximately constant relative widths. The  $\beta \approx 4.4$  means slight asymmetry. The uncertainties are confidence intervals (95 % confidence level).

| $\theta$   | $H_{50\%}$ (kA m $^{-1}$ ) | $\Delta H$ (kA m $^{-1}$ ) | $\Delta H/H_{50\%}$ | $\beta$  |
|------------|----------------------------|----------------------------|---------------------|----------|
| $0^\circ$  | 257[1]                     | 98[3]                      | 38%                 | 5.5[1.2] |
| $10^\circ$ | 248[1]                     | 100[2]                     | 40%                 | 4.9[0.7] |
| $30^\circ$ | 216[1]                     | 76[3]                      | 35%                 | 4.5[1.2] |
| $45^\circ$ | 212[1]                     | 73[3]                      | 34%                 | 3.7[0.7] |
| $60^\circ$ | 229[2]                     | 73[5]                      | 32%                 | 4.2[1.7] |
| $80^\circ$ | 314[3]                     | 96[6]                      | 31%                 | 3.3[1.2] |

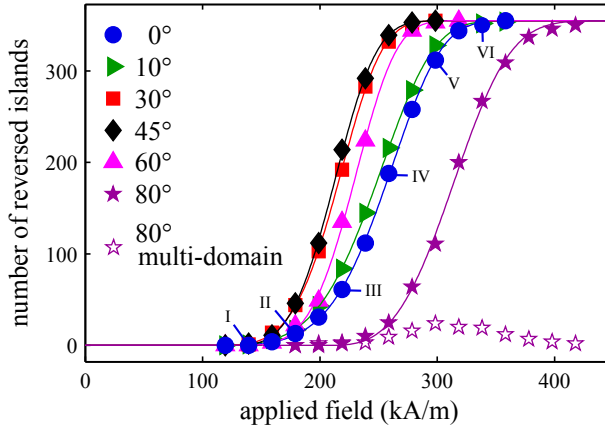


FIGURE 5.3 – Cumulative switching field distributions as function of applied field angle,  $\theta$ , where  $0^\circ$  is perpendicular to the sample surface. Partly reversed islands, i.e. multi-domain states, occur in the  $80^\circ$  series only (open stars). Weibull functions (lines) fit well to the distributions. Labels (I-VI) correspond to those of the MFM images in figure 5.1.

worse to the  $80^\circ$  SFD (see also table 5.1). Clearly, the  $45^\circ$  distribution has the smallest switching fields and the narrowest distribution. The  $80^\circ$  distribution has the highest switching fields and a wide distribution. The relative width is approximately constant (within 10 %) over the range of angles. This could hint at a single angular dependence, identical for all islands.

It is tempting to conclude from these SFDs that the switching field of *all* islands increase when the applied field angle increases from  $45^\circ$  to  $80^\circ$ , and that consequently a single mixed switching mechanism can explain the switching of all islands. However, the SFDs integrate the switching fields of the ensemble

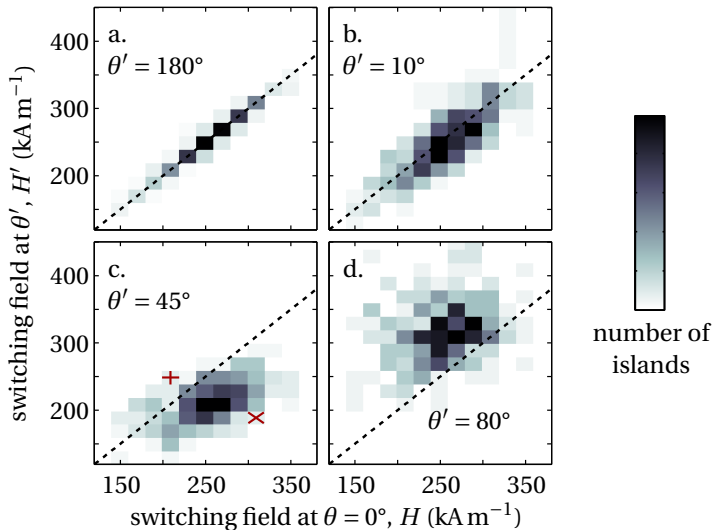


FIGURE 5.4 – 2D histograms comparing switching fields of islands at  $0^\circ$  field angle ( $H$  axis) to their switching fields at  $\theta'$  ( $H'$  axis). The colored rectangles represent the incremental number of islands that switched at  $H$  at  $0^\circ$  (horizontal axis) and at  $H'$  at  $\theta'$  (vertical axis). Darker colors correspond to more islands. In (a), switching fields measured perpendicular to the sample ( $0^\circ$  and  $180^\circ$ ) follow  $H' = H$  (dashed line) thus are highly correlated. For  $10^\circ$  and  $45^\circ$  (b, c)  $H'$  increases with  $H$ , and on average  $H' < H$ . Remarkable though, some strong islands in the  $0^\circ$  distribution ( $\times$  in c) have smaller  $H'$  than weak islands ( $+$  in c). In (d), switching fields are larger at  $80^\circ$  than at  $0^\circ$  and show no correlation. Clearly the sequential order in which the islands switch, varies drastically with field angle.

of islands, irrespectively of their individual angular dependence. When looking into more detail, we find in contrast that the order of switching of the islands varies with field angle. This is illustrated in the 2D histograms of figure 5.4, which allow us to find the switching fields at an angle  $\theta'$  (vertical axes) of islands that switched at field  $H_s$  when the angle  $\theta$  was  $0^\circ$  (horizontal axes).

For the switching fields at  $0^\circ$  and  $180^\circ$  (figure 5.4.a), we would expect perfect correlation *i.e.* islands switching at identical fields under both angles. Indeed, the switching fields are highly correlated, although some islands switch in adjacent bins (*i.e.* +1 or -1 field step). We attribute these differences to thermal fluctuations of the switching fields. Also at small angles ( $10^\circ$ , figure 5.4.b) the switching order is hardly altered and still correlated to the  $0^\circ$  distribution.

At  $45^\circ$ , however, the sequential order of switching is clearly not maintained. This is shown in figure 5.4.c, where for instance some weak islands at  $0^\circ$  (*i.e.* from the low tail of the  $\theta = 0^\circ$  SFD), are strong islands at  $45^\circ$  (*i.e.* appear in the high

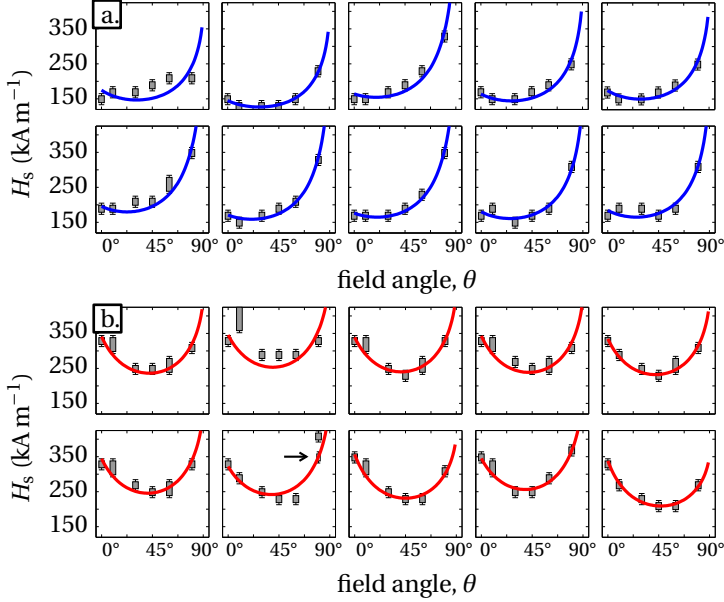


FIGURE 5.5 – Angular dependence of switching field of ten of the weakest (a) and strongest (b) islands in the 0° distribution. The field ranges (i.e. bins) in which islands switch (solid bars) or partly switch (arrow in b) are shown. Error bars represent  $2\sigma = 6 \text{ kA m}^{-1}$ . For weak islands, the angular dependencies have shapes close to a domain wall depinning modes. Strong islands show more coherent rotation shaped modes. Most shapes are well represented by fitted modified Kondorsky functions (lines), see also figure 5.6.

tail of  $\theta' = 45^\circ$  SFD). Moreover, the correlation in switching field is completely lost for  $\theta' = 80^\circ$  field angle (figure 5.4.d).

The effect of thermal fluctuations was simulated by adding fluctuations fields taken from a Gaussian distribution to switching fields sampled from the fitted Weibull distribution at 0° of figure 5.3. This allows us to create a 2D histogram of two simulated SFDs based on the same initial SFD, but with different fluctuations. The best match to figure 5.4.a is obtained for a fluctuation field of  $3(1) \text{ kA m}^{-1}$ . This value is in agreement with thermal fluctuation fields measured by Anomalous Hall Effect [Engelen et al., 2010; de Vries et al., 2013].

### 5.4.3 Individual islands

Figure 5.5 shows the angular dependence of the switching fields of individual islands. The figure compares islands that are weak (figure 5.5.a) and strong (figure 5.5.b) in the 0° distribution. Each graph shows the  $H_s(\theta)$  of a single island. These islands fall either in the first or last bin (*i.e.* field step) of the 0° SFD and

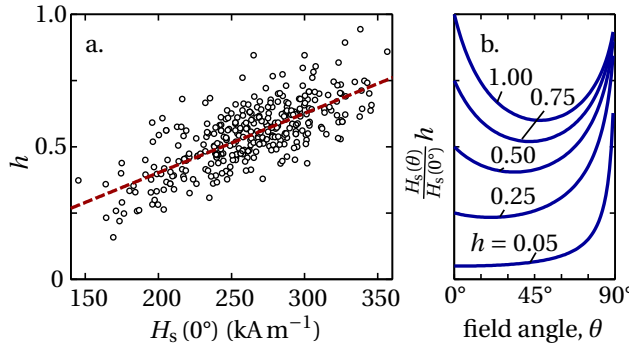


FIGURE 5.6 – (a) Fitted shape parameter  $h$  versus the fitted switching field at  $0^\circ$ ,  $H_0$ , resulting from fitting modified Kondorsky functions (b) to the angular dependent switching field of 355 individual islands. A linear fit to  $h$  (dashed line) highlights the trend from a more domain wall depinning ( $h = 0$ ) to a more coherent rotation ( $h = 1$ ) shaped angular dependence for islands with increasing switching field at  $0^\circ$ .

were picked rather arbitrarily (based on their position in the lattice). Strikingly, all weak islands have their largest switching field at  $80^\circ$  field angle, and at most only a shallow minimum at  $45^\circ$ . In contrast, all strong islands show a deep minimum at  $45^\circ$  angle, and similar switching fields at  $0$  and  $80$  degrees angle.

The modified Kondorsky functions in figure 5.5 fit reasonably well to the measured bins. Although for some islands the fits are not within the error bars, they capture the right trend of the angular dependence in almost all cases. Examples of modified Kondorsky functions are depicted for reference in figure 5.6.b.

Figure 5.6.a shows the fitted parameters. A trend of increasing shape parameter  $h$  with increasing switching field at  $0^\circ$  is clearly visible in figure 5.6.a. The trend is approximately linear. The shape parameter varies between 0.2 and 0.9 over the range of all measured  $H_s(0^\circ)$ . So the shape of the modified Kondorsky function varies from a more  $1/\cos$  angular dependence to a more coherent rotation like angular dependence.

#### 5.4.4 Discussion

The shape of the individual angular dependencies suggest that the dominating switching mechanisms differs between islands. Our explanation is based on the model of nucleation and subsequent domain wall propagation/depinning.

The likelihood of pinning decreases with increasing strength of the applied field. If the nucleation field is high, the external field is high once the domain wall is created. As a consequence the domain wall will propagate throughout the island without being pinned. The angular dependence of the switching field

therefore is dominated by nucleation, and we obtain the typical minimum at 45°. If the nucleation field is low however, the domain wall will be pinned. Since the depinning field is proportional to the perpendicular component of the field, we obtain the typical 1/cos behavior.

Because of this 1/cos angular dependence, the likelihood of domain wall pinning will increase with applied field angle. For islands with intermediate  $H_s(0^\circ)$ , the dominating switching mechanism at small angles might therefore change from nucleation to domain wall depinning. This crossover will occur at larger angles for stronger islands, which explains the trend of increasing  $h$  for higher  $H_s(0^\circ)$ .

Such mixed switching mechanisms were found and discussed before [Delalande et al., 2012; Dittrich et al., 2005; Hu et al., 2005b; Lau et al., 2011]. For larger individual islands the nucleation and pinning fields could even be extracted [Delalande et al., 2012; Lau et al., 2011]. However, an abrupt transition between extremal switching mechanism at some crossover  $\theta$  does not adequately represent  $H_s(\theta)$  of the islands. Possibly because none of the extremal switching modes take the finite geometry of the islands into account. Besides this, multiple nucleation and pinning sites may be involved, activated at different angles and temperatures [Shaw et al., 2008, 2010]. The fluctuating multi-domain remanence states we observed, also suggest pinning or nucleation at different sites. On the other hand, even in the absence of interior pinning defects, simulations have shown shallow, Kondorsky-like, angular dependencies [Uesaka et al., 1995]. Instead of defects, the increasing domain wall energy may prevent domain walls from propagating [Adam et al., 2012; Tudosa et al., 2012].

More remarkably is the rather large differences in  $H_s(\theta)$  although the islands are patterned identically. These differences could be caused by small fluctuations in their shape [Pfau et al., 2011]. On the other hand, even for identically shaped islands, unevenly distributed defects [Thomson et al., 2006] could cause the variations in  $H_s(\theta)$  of the array.

We cannot present evidence for any defects. However, edge defects likely dominate for our ion milled islands. The larger islands in [Delalande et al., 2012], patterned out of a different but identical film, would fall neatly within the distribution if included in figure 5.6 ( $H_s(0^\circ) = 250/250 \text{ kA m}^{-1}$  and  $h = 0.47/0.63$  for respectively  $D = 250/350 \text{ nm}$  islands). This is typical behavior for ion milled islands: a broad SFD, with small switching fields relatively insensitive to the size of the islands, compared to prepatterned islands [Shaw et al., 2008].

Irrespective of the possible origin of the defects, our results clearly show that in a lithographically patterned array the angular dependence of the switching field varies between islands. In general, a single, average, value of  $H_s(\theta)$  does not describe the behavior of an ensemble of islands well. Besides this, variations in the shape of the angular dependence could contribute to a wide SFD.

## 5.5 Conclusions

Using in-field MFM we determined the remanent switching fields of individual islands in a patterned array as a function of applied field angle. This work shows that similar islands may switch via different reversal mechanisms even though they are patterned in the same process.

The absolute value of the switching field, as well as the width of the distribution, reaches a minimum at 45° field angle. At 80° however, multi-domain states are induced and the switching field drastically increases. This is in agreement with reversal via nucleation by coherent rotation, and subsequent domain wall propagation with local wall pinning. [Delalande et al., 2012]

Individual islands have angular dependencies corresponding with reversal varying between domain wall depinning and coherent rotation modes. As a result, islands do not switch in the same order when the field angle is varied. Weak islands can become strong islands, and vice versa, in distributions taken under different angles.

In the 0° distribution, the weakest islands tend to reverse by domain wall depinning, whereas the strongest islands reverse more by coherent rotation. This behavior can be captured by a modified Kondorsky model, with shape parameter ranging from 0 for full domain wall depinning to 1 for coherent reversal modes. In our array of islands, the shape parameter varies from about 0.2 for the weakest, to 0.9 for the strongest islands.

This information, which could not have been obtained by integrating methods such as VSM, is crucial the search for the origins of the switching field distribution in arrays of patterned magnetic islands.

## 5.6 Acknowledgment

I and my colleagues would like to thank J. de Vries for fabrication and characterization of the sample. This research is supported by the Dutch Technology Foundation STW, applied science division of NWO and the technology program of the Ministry of Economic Affairs.

## Chapter 6

# Tip coating thickness dependence of tip-sample interactions in magnetic force microscopy on patterned arrays

### Abstract

The work described in this chapter has been done together with Martin Siekman, Hans Groenland and Leon Abelmann. The properties of magnetic force microscopy (MFM) tips are easily controlled by the thickness of their magnetic coating. We have investigated interactions between side-coated tips and 70–220 nm sized Co/Pt islands involved in imaging (read back), sample reversal (write) and tip reversal, by taking MFM images in different modes (*i.e.* in/non contact and in-field MFM), and by simulations. Tips with 35 to 80 nm thick CoNi side-coatings show a relation between read back signal and thickness that is in good agreement with a simple model based on a uniform tip magnetization, and considering only the last 400 nm of the tip. Judging from reversal of islands, we conclude that these tips have stray fields up to  $200 \text{ kA m}^{-1}$ , which is also in good agreement with the model. For some 80 nm coated tips, the MFM tip is irreversibly modified by the islands, which is a non-desired interaction. Very thick tips ( $> 80 \text{ nm}$ ) should therefore be avoided. For successful field assisted writing by MFM with side-coated MFM tips, it is necessary to narrow down the switching field distributions of the arrays.

### 6.1 Introduction

The magnetic force microscope (MFM) has been extensively used to visualize magnetization states of magnetic elements with nanoscale resolution [Zhu, 2005b]. Besides imaging (or ‘read back’) operation modes, MFM can be used to manipulate (‘write’) magnetic states of small magnetic elements locally and

in-situ [Zhu and Grütter, 2003]. This combination of reading and writing makes MFM an especially useful tool to investigate switching mechanisms [Lau and Shaw, 2011], or domain propagation in magnetic wires for memory [Parkin et al., 2008] or logic applications [Allwood et al., 2005], as it requires no complex spinstand [Teo et al., 2009] or drag tester [Moser et al., 1999] setup and special sample preparations. The MFM signal is caused by the interaction between the sample and the magnetic coating of the MFM tip. The main properties of the tip (*i.e.* resolution, stray field and stability) are most easily controlled by the thickness of this coating.

In this work, we investigate the effect of tip side-coating thickness on the interactions of the tip and sample that are involved in read-write experiments on patterned arrays of  $\sim 100\text{ nm}$ -sized magnetic islands with perpendicular anisotropy. Such islands are interesting for their rich switching behavior [Shaw et al., 2008; Thomson et al., 2006] (see also chapter 5).

MFM tips were used to write wires [Hassel et al., 2009], pillars [Jaafar et al., 2009], as well as thin-film recording media [Manalis et al., 1995] and islands with in-plane [Chang et al., 2006; Kleiber et al., 1998; Zhu et al., 2002] and perpendicular [Amos et al., 2012; Mironov et al., 2009] anisotropy. Most impressively, soft-magnetic elliptical islands could be manipulated into uniform and vortex states by precise control of the scanning motion of the tip [Chang et al., 2006]. Typically standard/commercial MFM tips are employed, which have a magnetic coating (*e.g.* Co and Fe alloys) applied on all four faces of their micromachined pyramidal tips (*e.g.* Bruker's 'MESP' tips). Thickly coated, high moment tips may directly write the sample solely by their strong stray fields [Amos et al., 2012; Kong et al., 1997]. In read back, such tips are employed strictly in non-contact mode to avoid unwanted writing; intentional writing is attained by letting the tip approach the sample selectively [Chang et al., 2006; Hassel et al., 2009; Mironov et al., 2009; Zhu et al., 2002]. Ideally however, the in-contact field of the tip is smaller than the switching fields of the imaged elements, as this allows for read back in tapping/liftmode without the tip distorting the sample. In this case, writing is performed by in-field MFM, using a bias field to assist the field of the tip [Jaafar et al., 2009; Kleiber et al., 1998; Manalis et al., 1995]. Still, to write all islands reliably, the tip field should be larger than the width of the switching field distribution of the islands.

In principle, thicker tip coatings increase the tip field and read back signal, at the cost of degrading resolution [Futamoto et al., 2013]. For uniformly magnetized islands with a diameter in the order of 100 nm however, resolution is not an issue: a coating thickness about the diameter of the island is theoretically optimal to read back their binary states [Mironov and Ermolaeva, 2009]. Of greater concern is the quality and stability (*e.g.* coercivity) of the tip magnetization, as this could inhibit the use of thick coatings. For instance, it was found that the MFM signal saturates or even decreases for thicknesses beyond 40–70 nm [Babcock et al., 1994; Chaplygin and Shevyakov, 2013; Choi et al., 2010; Kong et al., 1997]. Though, in these experiments it is not entirely clear if this is caused by a smaller moment of the tip or simply due to a reduced imaging resolution, as

simulations suggest [Choi et al., 2010].

The coercivity of the tip was determined directly using in-field MFM, by recording the contrast of MFM signals versus applied field [Futamoto et al., 2013; Jaafar et al., 2008]. Most relevantly, this method measures the coercivity of the part of the tip that is actually active in read back (*i.e.* the apex). Jaafar *et al.* investigated properties of several commercial tips [Jaafar et al., 2008]. They found, among other things, that a thick (150 nm) “high moment” tip has smaller coercivity than a standard (50 nm) tip. In similar experiments, Futamoto *et al.* found only a weak influence of the thickness of Co coatings in the 40–80 nm range on the switching fields of their fully coated tips. This behavior is similar to that of thin CoNi films deposited on flat substrates, which show a weakly decreasing coercivity with coating thickness (> 50 nm) [Spencer and Howson, 1986; Wan and Hadjipanayis, 1991]. We expect this behavior also for our CoNi side-coated tips, as the geometry of the side-coated layer approaches a thin film. Side coated tips where investigated by Heydon *et al.* [Heydon et al., 1997]. Contrastingly, their tips showed a strongly decreasing coercivity for 30–90 nm side-coatings. However, their coating material was CoPt and a larger part (several  $\mu\text{m}$ ) of the tip was active in the measurements.

In general, the active part of the tip is sample dependent on the dimension of the magnetic structures [Lohau et al., 1999]. For instance, Rastei *et al.* [Rastei et al., 2006] measured how the stray fields of tip and sample affect their magnetizations mutually. In their local hysteresis loops, the MFM contrast is recorded in-field, while the tip interacts with a patterned island. For larger islands, a larger fraction of the tip is active. Besides this, the effective write field of the tip depends on the probe motion [Chang et al., 2006; Kleiber et al., 1998; Mironov et al., 2009; Zhu et al., 2002] and the switching mechanism of the islands [Mironov et al., 2009]. For instance, Mironov *et al.* experienced this in their demonstration of probe recording on bit patterned media with perpendicular anisotropy [Mironov et al., 2009]. Their small 35 nm sized islands switch immediately when approached by the tip, whereas their larger 200 nm islands switch only if the tip performs a scanning motion over the islands. According to simulations, this motion is needed to expand a reversed domain.

We probe the effect of tip side-coating thickness using a patterned array of islands straightforwardly by taking MFM images in contact (*i.e.* tapping/liftmode) and non-contact (with bias field assist) modes. In this way, we determine directly the interactions between the tip apex and the  $\sim 100$  nm islands. We compare read back and effective tip field to calculations and magnetization loops.

In section 6.2, we determine theoretically the part of a side-coated tip active in read back and write interactions, taking into account the switching mechanism of the islands via approximate modeling. Experimental procedures and details about our tips and samples are given in section 6.3. We describe and discuss our results concerning read back, write (in/non contact) as well as unwanted tip-sample in section 6.4. Section 6.5 states our conclusions.

## 6.2 Theory

### 6.2.1 Tip and sample model

The tip and sample are modeled according to their simplified geometry, see figure 6.1. We used the same models in chapter 4 (figure 4.2).

The physical tip is a Si four-sided sharpened pyramid. The two back faces (towards the base of the cantilever) are covered by a thin film of Co<sub>at.80%</sub>Ni<sub>at.20%</sub>. At the apex, the two back-faces join into a single plane. We model this coating of this plane by a uniformly magnetized triangular prism [Van Schendel et al., 2000]. This prism is defined by ‘side angle’  $\alpha = 22.5^\circ$ , height  $L$  and variable thickness  $t$ . The physical tip has  $\sim 10 \mu\text{m}$  height, however only the apex contributes to the signal. We therefore vary  $L$  in simulations, and determine the part of the tip that significantly contributes to the read back signal and the write field. The cantilever tilt of  $10^\circ$  in combination with the tilted tip plane lead to a final inclination angle  $\beta$  of  $14^\circ$ . The magnetization of the tip is in the direction given by  $\beta$  i.e. ‘in-plane’ of the triangular prism, according to its shape anisotropy.

Our samples consist of islands with thin cylindrical magnetic layers. In our model, the islands have strictly uniform, perpendicular magnetization. The islands have equal periodicity  $\Lambda$  in both planar  $x$ ,  $y$  directions. Our simulations are based on sample B, see table 6.1. The maximum field that a tip experiences when in contact with a cylinder is  $< M_s \cdot t_s / D^*$ . Here  $M_s$  is the saturation magnetization of the sample, and  $t_s$  and  $D$  are the thickness and diameter of the cylinder, respectively. For samples A and B, imaged in tapping/liftmode MFM experiments, the field is at most  $12 \text{ kA m}^{-1}$ .

### 6.2.2 Simulation theory and method

The MFM signal is modeled according to equations (4.3)–(4.5) in chapter 4. In this chapter, we model the islands as perfect cylinders, with thickness  $t_s$  and diameter  $D$ . The effective charge density of an island is given by

$$\sigma_{\text{eff}}(\mathbf{k}) = M_s (1 - \exp(-|\mathbf{k}| t_s)) \frac{\pi D J_1(|\mathbf{k}| D/2)}{|\mathbf{k}|} \quad (6.1)$$

where  $J_1$  is a Bessel function of the first kind.

According to the model, the tip potential and charge density are proportional to  $M_{s,\text{tip}}$  and  $M_s$ , the saturation magnetization of the tip respectively the sample. The MFM read back signal (i.e. the phase shift between the drive signal and oscillation of the cantilever) is in turn proportional to the force gradient,  $\Delta\phi = -s \cdot F'$ . Close to resonance  $s = Q/c$ , i.e. the sensitivity of the phase to a force gradient is the quotient of the quality factor and spring constant of the cantilever, when modeled as a second-order system [Abelmann, 2010].

---

\*The maximum stray field results from evaluating the field on the axis of an axially magnetized cylinder [Griffiths, 1999].

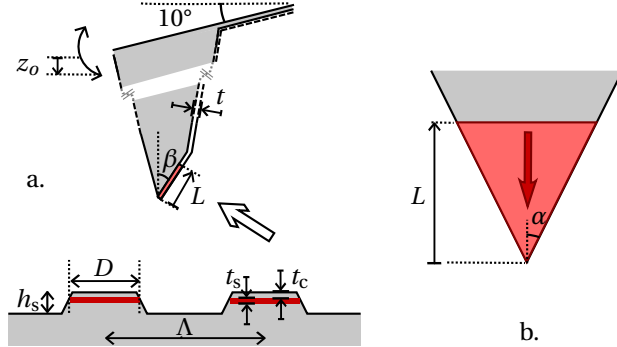


FIGURE 6.1 – Geometry of tip and sample (a), and a close up (b) of the apex of the tip as viewed from arrow in (a). The tip apex is modeled as a triangular prism (red triangle) with thickness  $t$  (= 35, 60 and 80 nm) and height  $L$ . By varying  $L$  we determine the active height in read back and write interactions. The tip has a uniform in-plane magnetization (red arrow). Symbols indicating tip and sample dimensions are explained in chapter 4 (figure 4.2, section 4.2.4.A).

The field of the tip follows directly from the negative gradient of  $\Phi$ . Whether this field reverses the islands depends on their switching field and reversal mechanism. The islands are believed to switch via a two step process of nucleation and domain wall propagation (see also chapter 5, section 5.2). In the nucleation step, a small domain reverses by coherent rotation. In the domain wall propagation step, this domain expands, switching the island fully. Both mechanisms have different dependencies on the angle of the applied field,  $\theta(x, z)$ . The local field of tip is strongest and mainly perpendicular ( $\theta = 0^\circ$ ) right under the tip apex, but takes different angles away from the apex. Therefore, the effect of the tip depends on the mechanism that dominates the reversal process.

The nucleation field according to a coherently rotating Stoner-Wohlfarth particle [Stoner and Wohlfarth, 1991, 1948] is

$$H_s(\theta) = \frac{H_s(0^\circ)}{\left[\cos^{\frac{2}{3}}(\theta) + \sin^{\frac{2}{3}}(\theta)\right]^{\frac{3}{2}}}. \quad (6.2)$$

Noticeably, a field applied at an angle of  $45^\circ$  has 2 times larger effect on nucleation compared to a  $0^\circ$  field.

The domain wall propagation field, according to the Kondorsky model (in which an invariably shaped wall separates anti-parallel domains), is

$$H_s(\theta) = \frac{H_s(0^\circ)}{\cos\theta}. \quad (6.3)$$

This  $H_s(\theta)$  is simply the perpendicular component  $H_z$  of the applied field. From

(6.2) and (6.3) it follows that near  $\theta = 0^\circ$ , the effect of a non-uniform tip field is larger for a nucleation than for a domain wall propagation dominated reversal.

In practice, the functional form of the angular dependence of the switching fields is between (6.2) and (6.3). This is attributed to different dominating switching mechanisms for different  $\theta$  [Lau et al., 2011]. We used modified Kondorsky functions [Schumacher, 1991] to capture these intermediate functional forms, by the ‘shape parameter’  $h$  (see chapter 5). For  $h = 0$ , the modified Kondorsky function is identical to equation (6.3). For  $h = 1$ , we find a nucleation-like angular dependence. At an angle of  $48^\circ$ , this dependence attains its maximum, which is 1.7 times larger in effect than a field applied at  $0^\circ$ . For our  $D = 70\text{ nm}$  islands,  $h$  takes values between 0.2 and 0.9.

Because the tip field is a local field, we should not expect to find the same switching fields as in the case of a uniform (globally) applied fields [Uesaka et al., 2012]. However, by comparing the number of islands that a tip switches to magnetization loop measurements (taken at  $\theta = 0^\circ$ ), we can determine the ‘equivalent uniform field’ of the tip. To relate this field to the actual stray field of the tip, we calculate the theoretical write bubbles of the tip, and determine the extend of the field. These bubbles are formed by contour lines of constant  $H_s(0^\circ)$ , *i.e.* lines where the tip field will switch an infinitely small island that has a certain switching field at  $0^\circ$  ( $H_s(0^\circ)$ ), according to the angular dependence of the switching mechanism.

In our simulations, we use the method described in section 4.2.4, and compute the tip potential in (4.5) analytically [Wilton et al., 1984] and obtain  $\Phi_0(\mathbf{k})$  numerically via a fast Fourier transform (FFT). Since we keep  $z$  constant, we get the force gradient by applying an inverse FFT to  $\Delta\phi(\mathbf{k})$  in (4.3), after applying transfer functions in the Fourier domain according to (4.5).

### 6.2.3 Simulation results

In figure 6.2, we vary  $L$  and test the read back signal of  $D = 220\text{ nm}$  islands (see table 6.1). The height of the active region of the tip in read back is approximately 400 nm, as increasing  $L$  further does no affect the MFM signal significantly. This active height has been found before, based on MFM images of features with similar size as our islands [Babcock et al., 1994]. Moreover, according to figure 6.2.b, the active volume is approximately constant over the range of practical scan heights. Besides this, the amplitude is linear with coating thickness for  $D = 220\text{ nm}$  and scan heights of 40 to 160 nm. The detailed pulse shape does however vary with  $t$ . For instance, the width of pulse, and the width of the peaks in the pulse, increases with  $t$ .

A small active height means that the shape of the tip apex is important, which is not well modeled by a sharp triangle. However we find that read back is not determined solely by the very apex of the tip; the magnetization up to 100 nm contributes linearly up to about 50 % of the signal in figure 6.2.b.

For too large active heights on the other hand, the magnetization of the tip is not uniform, as the remanence state of triangular thin-film elements show

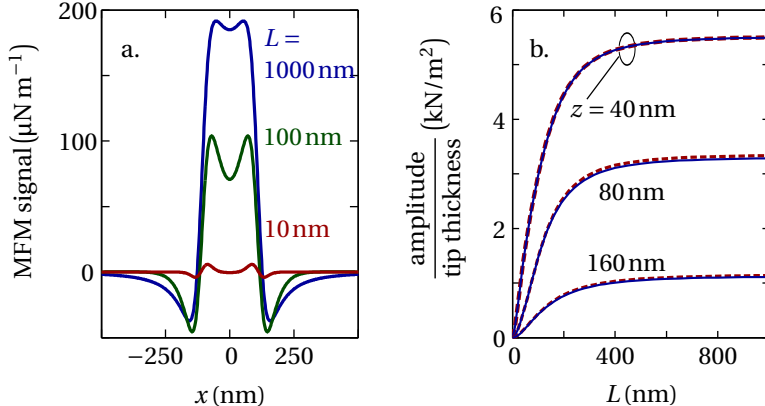


FIGURE 6.2 – Simulated read back signal dependence on tip height,  $L$ . (a) The amplitude of the pulse (i.e. maximum signal) increases with tip height [ $L = 10$  (red),  $100$  (green) and  $1000$  nm (blue)] and its shape varies. (b) The amplitude is linear with coating thickness [ $t = 35$  (blue, solid line),  $80$  nm (red, dashed line)], and has converged (> 90%) for  $L = 400$  nm for relevant scan heights,  $z$ . The ‘very apex’ of the tip (up to  $L = 100$  nm) causes only about 50 % of the amplitude. In (a)  $z = 40$  nm and  $t = 35$  nm.  $D = 220$  nm (sample B).

flux closing domains [Kirk *et al.*, 2001]. However, Lorentz microscopy images of the stray field of the apex of a side coated tip indicated a nearly uniform magnetization in the order of a micrometer [Zhou *et al.*, 1995]. So, the apex could well be in an approximate single domain state for  $L \approx 1\mu\text{m}$ .

Concerning the tip field, figure 6.3.a shows the  $H_z$  bubble for increasing  $L$ . In contrast to the read back case, the active height for the tip field varies with scan height. The field near the apex builds up quickly with  $L$ . So the in-contact field depends strongly on the shape of the apex of the tip. A larger  $L = 1000$  nm is needed to have convergence to a  $25\text{ kA m}^{-1}$  field at  $z \approx 75$  nm underneath the apex. Such large  $L$  were also determined by McVitie *et al.* experimentally [McVitie *et al.*, 2001]: These authors fitted, depending on the lateral distance to the tip, active heights exceeding  $1\mu\text{m}$  to the field of a fully coated pyramidal tip.

The in-contact write bubbles for nucleation and domain wall propagation of  $35$  and  $80$  nm tips are shown in figure 6.3.b-c. The indicated tip sample separations are those occurring in the tapping mode AFM pass of the tapping/liftmode operation. The bubbles show where the field is strong enough to switch islands with a  $H_s(0^\circ)$  between  $100$  and  $200\text{ kA m}^{-1}$ , according to (6.2) and (6.3). As expected, the nucleation write bubble (red) is larger than the domain wall propagation bubble (blue). Both bubbles are smaller than a  $D = 220\text{ nm}$  island. Even so, the nucleation bubble is larger than nucleation radius expected for easily switching islands [de Vries, 2013]. To reverse an island fully however, a nucleated domain must expand through propagation of its domain wall [Mironov

et al., 2009]. A force on the wall is needed to prevent the bubble from collapsing back to its initial, non-reversed, state. For this, the largest tip-sample  $2a \approx 40$  nm is critical, as this separation results in the smallest  $H_z$ . For the 35 nm tip, the field drops below  $100$  kA m $^{-1}$  at this separation. Therefore, a 35 nm tip will not reverse any islands with  $H_s(0^\circ) > 100$  kA m $^{-1}$  (*i.e.* the propagation field). In contrast, the  $H_z$  field of a 80 nm tip is larger than  $100$  kA m $^{-1}$  at maximum tip-sample separation, see figure 6.3.c. According to the model an 80 nm tip may switch islands in the 100 to 200 kA m $^{-1}$  range.

In non-contact MFM, we use a larger tip-sample separation,  $z \approx 65$  nm. Consequently, the write bubbles for a 35 nm tip extend over a larger area, see figure 6.3.d. Shown are modified Kondorsky write bubbles, with  $h = 0.25$  and 0.75. The field of the tip is assisted by a 250 kA m $^{-1}$  uniform, perpendicular, bias field. The hatched regions indicate where the effect of the tip field (*i.e.* excluding the bias field) is 20 to 30 kA m $^{-1}$ . So, in total the bubbles have equivalent uniform fields of 270 to 280 kA m $^{-1}$ . Due to the strong perpendicular bias a small range of  $\theta$  is involved in the region shown. The 0.75 bubble is slightly stronger, due to its stronger angular dependence for small  $\theta$ . The parameters used are relevant for our  $D = 70$  nm islands. Clearly, the bubbles cover the islands fully. Centered above an island, the field is approximately uniform. As a result, no scanning motion of the tip is needed to propagate the domain wall and the relevant  $z$  is the smallest tip-sample distance. According to this model, we expect the tip field is in effect equivalent to a uniform field of about 30 kA m $^{-1}$ . For strong islands in the distribution ( $h = 0.75$  up to 0.9) the effect of the tip is slightly stronger; at most 9 kA m $^{-1}$  at  $z = 65$  nm for  $h = 0.75$ .

## 6.3 Experiment

### 6.3.1 Side-coated MFM tips

We used commercial (Smart-Tip) AFM and 35 nm side-coated MFM tips (SC-35-M), with respectively 320 kHz and 78 kHz resonance frequency ( $\omega_0/2\pi$ ). A layer was deposited onto the AFM tips, evaporated from an Co<sub>at.80%</sub>Ni<sub>at.20%</sub> alloy. The tips were mounted under an angle, so only the back-sides of the tip were coated. Some material is deposited on the base of the cantilever in this procedure.

Figure 6.4 shows helium ion microscope (HIM) images apices of tips with 35 and 80 nm coating. A nice single sided coated layer of nominal thickness is visible. The magnetic CoNi layer forms the apex of the tip. The ‘very apex’ of the tips are bent, presumably due to stress between Si and deposited CoNi. This makes thick layers sensitive to wear, and may limit the maximum allowable coating thickness, as the bending is stronger for the thicker coating.

The 320 kHz MFM tips used in tapping/liftmode read back experiments are based on 125 μm × 30 μm × 4 μm Si cantilevers with a nominal 42 N m $^{-1}$  spring constant. To asses the sensitivity,  $s$ , we determined the frequency responses of several tips. We estimate the sensitivity of approached tips by  $s = 17(3)$  rad/Nm $^{-1}$ , see Appendix C.

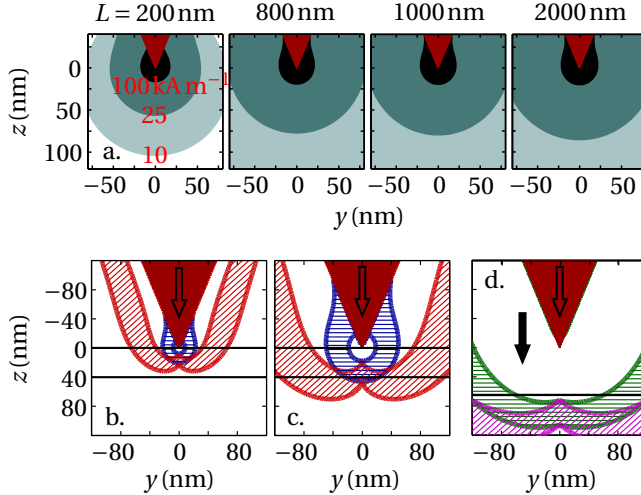


FIGURE 6.3 – *Simulated write bubbles for variations in tip height  $L$  (a) and coating thickness [ $t = 35$  (a,b,d) and  $80$  nm (c)], and for an assisting bias field (d). In (a) the  $H_z = 100$  kA m $^{-1}$  field at  $z = 20$  nm converges readily for  $L = 200$  nm. The active height is much larger ( $L = 1000$  nm) for  $z = 75$  nm. In (b) the in-contact nucleation bubble for 100 to 200 kA m $^{-1}$  (red shade) extends over a large area ( $|y| > 30$  nm), sufficient to induce a reversed domain in a (weak)  $D = 220$  nm island. However, at the large  $z = 40$  nm occurring in tapping-mode, the domain wall propagation bubble ( $H_z$ , blue) vanishes. For  $t = 80$  nm (c) the bubbles extend over larger areas and maintain pressure on the domain wall during the full cantilever oscillation, thus capable to write islands. In (d) the non-contact ( $z = 65$  nm) bias field assisted write bubbles,  $H_a + H_t = 250 + (20$  to  $30)$  kA m $^{-1}$  extend over the full  $D = 70$  nm islands and are in effect similar to uniform fields. The bubbles represent  $H_s(\theta)$  of weak (green,  $h = 0.25$ ) and strong (purple,  $h = 0.75$ ) islands; fields have slightly larger effect for strong islands. In (b-d)  $L = 1000$  nm.*

The 78 kHz MFM tips used in non-contact, vacuum, experiments have  $Q = 4.0 \times 10^3$  and nominally  $c = 2.4$  N m $^{-1}$ . This results in a sensitivity  $s_{\Delta\omega} = \omega_0/2c$  of 16 kHz/Nm $^{-1}$  for the frequency shift due to a force gradient.

### 6.3.2 Patterned arrays

Detailed fabrication of the samples is described in [de Vries, 2013]. Briefly, a Pt(30 nm) seed layer and 2-7 nm Co/Pt multilayers (see table 6.1) were deposited on a SiO<sub>2</sub>/Si substrate via UHV magnetron sputtering, as well as a 3 nm Pt capping layer. A top and bottom anti-reflective-coating (BARC) and photoresist layer were spin coated for laser interference lithography. The developed

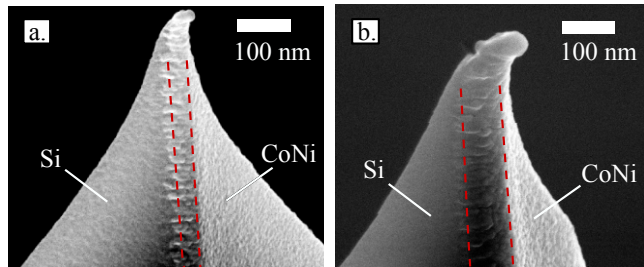


FIGURE 6.4 – Helium ion micrographs [Orion Plus (Zeiss), SE mode, 35 kV] of the apices of MFM tips with CoNi side coating of 35 nm (a) and 80 nm (b) thickness. For > 100 nm from the apex, the layers are conformal and have the desired thickness (dashed lines). The coated layers extend over the Si and are curved towards the CoNi-side, more strongly for the 80 nm tip. Wear of the apex will directly affect the magnetic properties of the tips.

TABLE 6.1 – Properties of the samples used in read back (A-C) and write experiments in tapping (B) and non-contact (C) mode.

|          | $D$<br>(nm) | $\Lambda$<br>(nm) | multi-layer<br>(nm)   | $M_s$<br>(kA m <sup>-1</sup> ) |
|----------|-------------|-------------------|-----------------------|--------------------------------|
| sample A | 110         | 500               | [Co(0.4)/Pt(1.0)] × 5 | 450                            |
| sample B | 220         | 600               | [Co(0.3)/Pt(0.3)] × 3 | 870                            |
| sample C | 70          | 300               | [Co(0.4)/Pt(1.0)] × 5 | 450                            |

pattern was transferred into the magnetic stack by O<sub>2</sub>-plasma and Ar ion etching. Due to some residual BARC material on sample C, the smallest allowable scan height is  $z \approx 65$  nm. For sample A and B, only small amounts (several nm) residual material remains on some of the islands. Table 6.1 lists the magnetic and geometric properties of the samples.

Figure 6.5 shows the magnetization loop of the  $D = 220$  nm islands, obtained by a vibrating sample magnetometry (VSM) at room temperature using a DMS VSM-10. After saturating at 1400 kA m<sup>-1</sup>, the field was swept at a rate of 32 Am<sup>-1</sup>/s in the 80 kA m<sup>-1</sup> to 280 kA m<sup>-1</sup> range. The switching fields of the  $D = 70$  nm islands have been determined previously using in-field MFM (see chapter 5). For this, we applied step-wise increasing field pulses with 1 s duration and counted the number of switched islands in MFM images taken in-between field steps. The resulting cumulative switching field distribution, or ‘direct current demagnetization’ (DCD) curve, is included in figure 6.11.a.

### 6.3.3 Experimental procedures and methods

We used two MFMs. For in-contact experiments in ambient conditions (on sample A and B), we used a desktop DI3100 (Digital Instruments) in liftmode

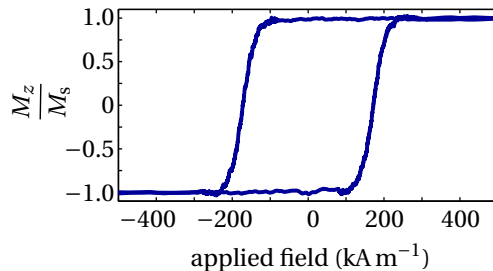


FIGURE 6.5 – VSM magnetization loop of the  $D = 220\text{ nm}$  islands (sample B). The onset of the loop is near  $100\text{ kA m}^{-1}$ ; 20 % and 80 % of the islands have switched at  $150\text{ kA m}^{-1}$  and  $200\text{ kA m}^{-1}$ , respectively.

and *linear* liftmode (see chapter 4). For non-contact experiments (sample C), we used a home-built vacuum MFM, with in-field imaging capabilities.

The non-contact mode employed a ‘constant height’ imaging mode. However, the scan height (*i.e.* tip-sample separation) fluctuated due to the parabolic distortion of the piezo tube scanner and piezo nonlinearities. The scan height fluctuates over 30 nm from the center to the edges of the scanned area. Also the absolute scan-height is unknown in non-contact mode. In order to compare simulated and measured read back pulses, we fitted for each island (*i.e.* read back pulse) the scan height and background level.

We applied corrections to the MFM images (see chapter 4) for background and interference signals, positioning errors (piezo distortion and drift), and force gradients of non-magnetic origin. Images taken in liftmode were corrected for scan height variations. Typical scan heights in liftmode are nominally 20 nm. The actual scan height is however set off by an additional, approximately 20 nm *i.e.* the amplitude of the cantilever in the tapping mode pass, controlled by the set-point.

For the in-contact write experiments, we counted the number of islands that switched while scanning an MFM image. The islands that switched showed black (*i.e.* attractive) MFM contrasts. Prior to imaging, the samples and tips were DC magnetized using a NdFeB permanent magnet. We captured MFM data directly after landing the tip. The MFM started in the center of the imaged area, scanning in an upward direction, at 1–2 s per scan line. The first 2–3 scan lines taken were noisy, as the tip and electronics needed to settle after approaching.

In non-contact write experiments, the tip field was assisted by a bias field. Similar to the DCD measurements described above, we applied fields in a step-wise increasing fashion. However the field was kept on during acquisition of the MFM image. We counted the number of islands that switched in these images. Scan rates were such that the tip spent 1–4 s above an island.

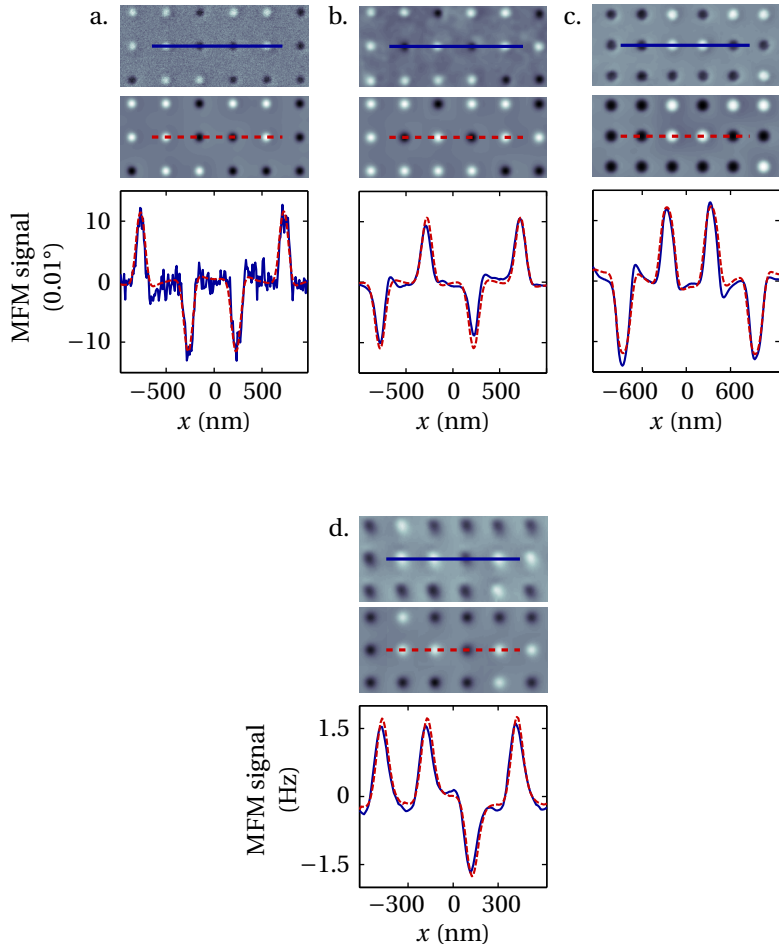


FIGURE 6.6 – *Measured (blue) and simulated (red) read back signals of a (a) 35, (b) 60 and (c) 80 nm tip in contact, and (d) 35 nm tip in non-contact. In (a-c), simulations used a fitted sensitivity  $s = 8 \text{ rad}/(\text{Nm}^{-1})$ , 2.1 times smaller than expected. In (d) the unknown background level and scan height (58 to 78 nm, mostly  $z = 65 \text{ nm}$ ) were fitted for each MFM pulse, using the nominal sensitivity. All simulated pulse amplitudes and shapes agree well with experiments. Scan height are 57 (a), 76 (b) and 69 nm (c) respectively, and MFM modes: (a) linear lift (b,c) liftmode after correction for scan height variations, and (d) non-contact frequency modulation MFM in a  $260 \text{ kA m}^{-1}$  perpendicular field. Imaged samples are (a,b) sample A, (c) sample B, and (d) sample C.*

## 6.4 Results and discussion

### 6.4.1 Read back

Figure 6.6 shows experimental and simulated MFM images and *i.e.* cross-sections (scan lines). To convert simulated force gradients to phase shift signals, we used an adjusted sensitivity of  $s = 8 \text{ rad/Nm}^{-1}$ . Using this factor, the amplitudes and shapes of the simulated pulses agree very well with experiments, and reproduce the dependence on  $t$ . Simulated amplitudes are within 10 % of the average pulse amplitude<sup>†</sup>. However, the sensitivity is much smaller than the  $17 \text{ rad/Nm}^{-1}$  expected from the frequency responses of the tips.

The smaller  $s$  could (partly) be due to a reduced moment of the tip caused by a apex magnetization that is non-uniform *i.e.* the magnetization shows variations in angle to reduce magnetostatic energy [Tomlinson and Farley, 1997]. A large error in active height, scan height or tip shape, is unlikely, as the simulated pulse shapes match the experimental ones well. Similarly, a strongly reduced moment induced by the stray field of the sample would distort the signal and result in differences between pulses of up and down magnetized islands. We do not observe this. A combination of small effects however, in addition to a reduced magnetization, could lead to the 2.1 times difference.

For the non-contact in-field MFM signals in 6.6.d, we fitted the unknown scan height and background level in simulations for each island/pulse. The resulting  $z \approx 65 \text{ nm}$  and  $58\text{--}78 \text{ nm}$  range is in agreement with spectroscopy/AFM experiments. With the fitted  $z$  the pulse amplitudes and shapes are in good correspondence with experiments.

### 6.4.2 Write field

#### 6.4.2.A No or small write interactions

Scanning with a commercial 35 nm tip, in figure 6.7, results in no observable effect of the tip field. The 35 nm tip is our standard for imaging patterned arrays. In our experience, island reversal is only observed if the islands are already in a multi-domain states before imaging. Similarly, a 60 nm tip shows little write interaction. Figure 6.8 shows two pairs (a-b and c-d) of consecutive scans with a 60 nm tip. Only a single island switches in the first row of islands that is fully scanned. Scanning more islands (fig b), even after remagnetizing the tip (c d), does not result in more switched islands.

Comparing to the VSM magnetization curve (figure 6.5), the field of the 35 nm tip is in effect smaller than a  $100 \text{ kA m}^{-1}$ , as this is the onset field at which islands reverse in the VSM loop. Because a 60 nm tip is able to switch an island, its equivalent uniform field is about  $100 \text{ kA m}^{-1}$ . From these images, we cannot

---

<sup>†</sup>Here we took the pulse amplitude with respect to local back ground signal (*i.e.* the signal in between islands), as this fluctuates in experiment.

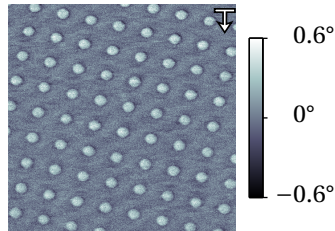


FIGURE 6.7 – MFM image of a DC erased patterned array raster scanned by a tip with 35 nm coating. Black and white contrasts corresponds to respectively attractive and repulsive force gradients. The image shows only white pulses, which means that none of the islands reverses its magnetization during scanning. The arrow indicates the scanning direction.

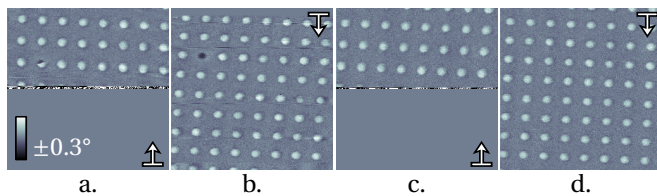


FIGURE 6.8 – Behavior of the 60 nm tips. In (a-b) a single island switches. After remagnetizing the tip (c-d) no islands switch.

conclude that the fields are stable over time, because island reversals are too rare.

#### 6.4.2.B Stable write interactions

We observed strong write interaction in tapping mode for an 80 nm tip, see figure 6.9. Scanning over the initially DC magnetized sample yields many reversed (black) and reversing (turning to black) islands. This is the behavior of an 80 nm ‘case I’ tip. For this case the tip is not influenced by the sample. However, we observed other, undesired interactions for 80 nm tips in which the sample strongly influences the tip. These cases (II and III) are discussed below.

Figure 6.10 shows the stability of the case I tips. We made several scans with the same tip. Images were taken at different locations around the same area, resulting in (slightly) overlapping images. The bar graphs represent the number of islands that switched when they were scanned for the first time (*i.e.* the first time the island appears in the image; occasionally, some islands switch in a second (or consecutive) pass of the tip). The error bars estimate the 95% confidence levels, based on a normally distributed switching probability and finite sample size [Wilson, 1927]. The error bars vary because, due to the

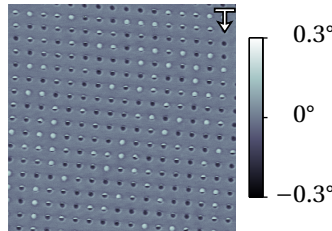


FIGURE 6.9 – MFM image made with a ‘case I’ tip with an 80 nm coating. Many islands reverse their magnetization, appearing as an abrupt switch from a white to a black pulse in the MFM image.

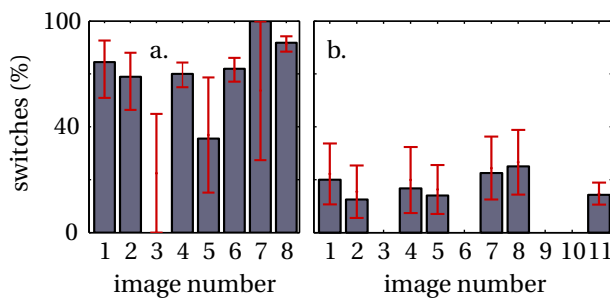


FIGURE 6.10 – Fraction of islands that switched in the first pass of the tip for subsequently scanned images, for two ‘case I’ tips with 80 nm coating. In (b) the tip is remagnetized after image 3 and 6. The error bars indicate estimated 95% confidence levels based on the sample size (e.g. in image 3 in (a) 0 out of 3 newly imaged islands switched). On average 80% (a) and 20% (b) of the islands switch, approximately constant over the number of images taken. In (b) no new (first-pass) islands were imaged in 3, 6, 9 and 10.

overlap, not each image contains the same number of ‘new’ islands, not imaged before.

In figure 6.10.a, roughly 80% of the islands switch. Here, the images were taken subsequently, after a single approach. The percentage of switched islands remains constant, even after 8 scans. This indicates a stable magnetic state of the tip. Similarly, the 80 nm tip tested in figure 6.10.b switches an approximately constant number of islands. About 20% of the islands switch in each scanned image. In this series of images, the tip approached the sample 3 times, after being remagnetized. This indicates a reproducible and stable magnetic state of the tip. According to the magnetization loop (figure 6.5), the tips have an equivalent uniform field of  $200 \text{ kA m}^{-1}$  and  $150 \text{ kA m}^{-1}$ , since these are the fields at which 80% respectively 20% of the islands reverse.

In non-contact mode, we use the assistance of a bias field to determine

the field of 35 nm tips. Figure 6.11.a shows 3 magnetization curves. Two were taken in-field for two different tips. The third curve is a regular DCD curve, in which the bias field was turned off while the image was taken. Comparing the in-field curves to the DCD curve, the in-field curves appear shifted by 30 and 18 kA m<sup>-1</sup> towards lower applied fields. These shifts are about constant for the whole distribution *i.e.* the width/shape of the curves are not affected. This indicates that effect of the tip field is constant for each island, independent of its switching field. We expect the difference between the two in-field curves are caused by variations in scan height between measurement series.

Figure 6.11.b shows that the effect of the tip field is indeed constant. This 2D histogram<sup>‡</sup> compares switching fields with ('bias field assist' vertical axis) and without ('DCD' horizontal axis) the field of the tip. The colored rectangles indicate the number of islands that switched at  $H$  in the DCD curve *and* at  $H'$  in the in-field curve. The distributions are highly correlated; weak and strong islands in the DCD distribution are also weak and strong switchers in the bias field assisted distribution. Thermal fluctuations of the switching fields may cause the spread/width ( $\pm 1$  field step) in the histogram. Clearly the 18 kA m<sup>-1</sup> shift is the same for weak and strong islands, although their dominating switching mechanism varies significantly (*i.e.* domain wall propagation respectively nucleation). The tip field is in effect equivalent to applying a uniform bias field. This was expected from the shape of write bubbles, which cover the islands completely. Moreover, the measured 18 and 30 kA m<sup>-1</sup> fields for scan heights between 60 and 80 nm is close to our simulations. However, a possible increase in effective tip field for weak to strong islands is not evident in figure 6.11.

#### 6.4.3 Undesired tip-sample interactions

Instead of the tip sensing and manipulating the stray field respectively magnetization of the sample, the sample may influence the tip. We observed this for some 80 nm tips. Their properties are dramatically affected. We distinguish two cases, in addition to the 'case I' 80 nm tip, discussed above.

Case II behavior is shown in figure 6.12. The tip manipulates the sample, as some island switch in figure 6.12.a. However, this happens only in the first few scan lines (~ two scanned rows of islands). Strikingly, no additional islands switch in 6.12.a, or in subsequently scanned images 6.12.(b-d). The same happens after remagnetizing the tip; again, only in the first scan lines islands switch<sup>§</sup>. Also the MFM signal appears to degrade, as topographic interactions increases in the subsequent imaging. Remagnetizing the tip restores the MFM signal.

---

<sup>‡</sup>In chapter 5, we used similar 2D histograms in figure 5.4

<sup>§</sup>Except for the two domain island (see center of figure 6.12.f). This island switches partly in figure 6.12.e, survives in two domain state while imaged in figure 6.12.f, but finally fully reverses in figure 6.12.g.

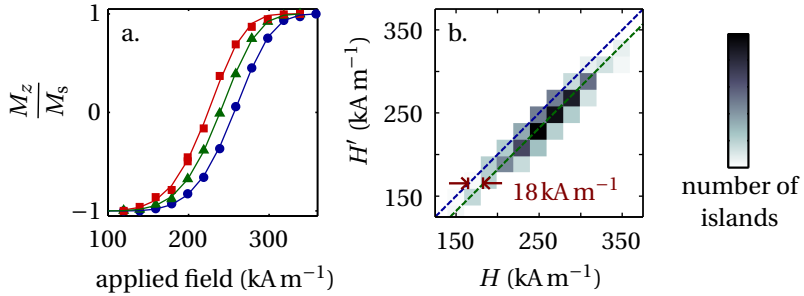


FIGURE 6.11 – *Cumulative switching field distribution (a) of 70 nm islands (sample C) determined by non-contact MFM, using an applied field only ('DCD',  $\circ$ ), and an applied field + tip field ('bias field assisted',  $\triangle \square$ , scanned at 1 s respectively 4 s per island, at  $z \approx 65 \text{ nm}$ ). The tip field reduces the whole DCD-distribution by 18 ( $\triangle$ ) and 30  $\text{kA m}^{-1}$  ( $\square$ ). Comparing individual islands in a 2D histogram (b), indeed shows high correlation between bias field assisted  $\triangle$  ( $H'$ -axis) and DCD ( $H$ -axis) switching fields (following green line); the constant 18  $\text{kA m}^{-1}$  shift from the  $H' = H$  (blue line) is equal for weak to strong islands.*

Apparently, the effective field of the tip weakens during scanning and this can be restored by remagnetizing the tip. These reversible effects indicate the tip is demagnetized by the stray field of the sample.

Figure 6.13 displays case III behavior of a 80 nm tip. Initially all islands switch in the first pass of the tip. The islands switch when the tip is far away from the island, because only black, attractive MFM contrast is visible. However, the switching position gets closer to the center of the islands in image 6.13.c–d, as larger white, repulsive regions appear in the images. More clearly, the reducing number of switching islands in 6.13.e–f, indicates a weaker moment of the tip. Remagnetizing restores some of the tips magnetization, however the read back signal is about halved (figure 6.13.g). Finally, in image 6.13.h, the switching capacity of the tip is gone and the tip crashes frequently into an island in the liftmode (supposedly non-contact) pass.

This irreversible reduction in effective tip field can be attributed to wear of the tip. We suspect that the strong field of the tip (effectively at least 250  $\text{kA m}^{-1}$ , as all islands switch) is due to a strongly bended tip apex, resulting in more magnetic material close to the sample. Also, such a deformed tip likely demagnetizes [Tomlinson et al., 1995] and wears easily.

#### 6.4.4 Discussion

From the expected linear behavior of the magnetic signal with coating thickness, we can conclude that the magnetization is not deteriorating for  $t = 35 – 80 \text{ nm}$ . However stability issues, likely due to the bent shape of the apex, limit the

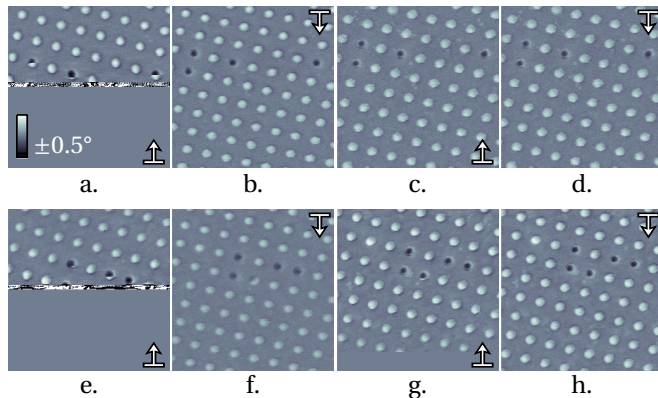


FIGURE 6.12 – MFM images demonstrating ‘case II’ type behavior of an MFM tip with 80 nm coating; (a) is the first scan after approaching the sample, (b-d) have been scanned subsequently. (e) is the first scan after remagnetizing the tip and approaching the sample on a different spot; (f-h) have been scanned subsequently. Islands switch only in the first scan lines of (a) and (e), indicating that the tips magnetization weakens during scanning, but can be restored by remagnetizing the tip.

allowable thickness to about 80 nm. As a result, the effective field of side-coated tips has a maximum of about  $200 \text{ kA m}^{-1}$ , though possibly larger in a bias field as we expect that a slightly non-uniform apex magnetization could reduce the moment of the tip in remanence. The effective field could either be governed by a nucleation or a domain wall propagation field. Nevertheless it is larger than possible depinning fields (retaining islands in 2-domain states at remanence) as all our islands reverse fully.

Typically, the switching fields of small islands [Thomson et al., 2006] are larger (*e.g.* sample C) than this effective field. This admits the use of contact modes. However,  $200 \text{ kA m}^{-1}$  is typically smaller than the width of the switching field distribution of such islands (*e.g.* sample C). Hence, for probe recording purposes, the higher moment of a completely (and thickly) coated tip seems required, or perhaps an energy assisted writing scheme [Zhang et al., 2006].

A side-coated tip can however program an array of islands, even though its field is smaller than the width of their switching field distribution. As figure 6.14 shows, first the strongest islands are written, and thereafter the weaker islands at step-wise monotonically decreasing bias fields. Here, writing is attained by letting the tip approach and raster scan over an island. Though time consuming and incapable to update islands, this method lets us record any desired sequence onto the sample.

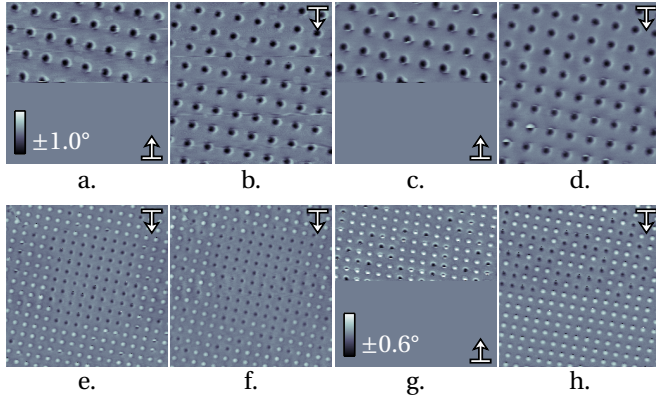


FIGURE 6.13 – ‘Case III’ behavior of a tip with an 80 nm coating. (a) and (b) are the first scans made after approach; (c-f) have been made at a new spot, without remagnetizing the tip; in (e-f) the scan range is extended and the resolution is halve (e) and the same (f) as in (a-d). The small black and white spots in (e) are due to contact between tip and sample. In (a-d) all islands switch in the first pass of the tip. However, in (d-e) the islands switch when the tip is closer to the centers of the islands. This indicates a weaker moment of the tip. In (e) only 13 % of the islands switch in the first pass of the tip, indicating a reduced moment of the tip. The weaker moment is irreversible, as only a few islands switch after remagnetization (g). The tip fails in (h).

## 6.5 Conclusions

We investigated the interactions between side-coated MFM tips and patterned arrays of magnetic islands with 70 to 220 nm diameter, as a function of magnetic coating thickness, both in theory and experiment. We considered imaging (read back), reversal of the magnetization in the islands by the MFM tip (write) and undesired sample-tip interaction.

We modeled the MFM tip by a uniformly magnetized triangular magnetic element. This simple model is in good agreement with observed read back signals. The model reproduces the pulse shapes and the dependence on coating thickness excellently, with relatively an error less than 10 % in amplitudes. However, the model predicts signals with two times larger magnitude than the in-contact phase shift signals acquired in liftmode. We found that the pulse amplitude is linear with tip thickness in the range of 35 to 80 nm. From the model, we conclude that 400 nm of the apex of the MFM tip contributes significantly to the signal.

We used the stray field of the MFM tip to reverse the islands. We define the equivalent field of the tip, as the applied field at which the island switches if the field would be uniform. In contact mode, this equivalent field increases with tip thickness from less than  $100 \text{ kA m}^{-1}$  for 35 nm tips to  $200 \text{ kA m}^{-1}$  for 80 nm

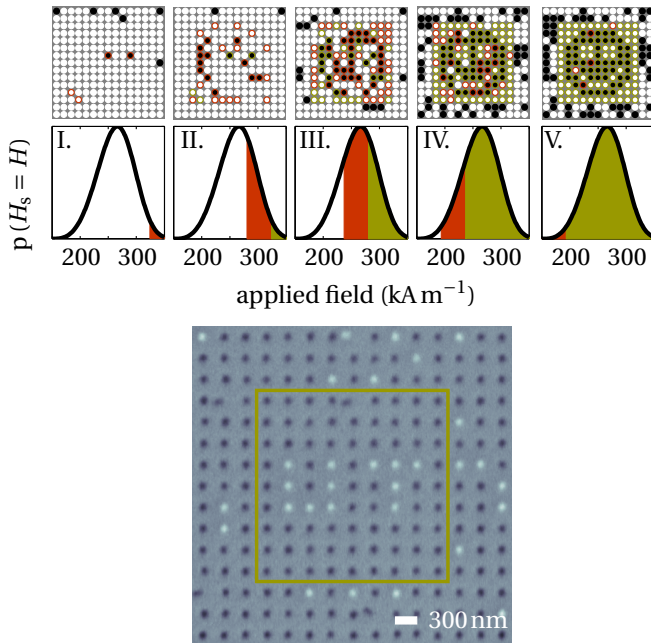


FIGURE 6.14 – ‘Write’ demonstration using a 35 nm tip of which the field ( $H_t$ ) is smaller than the width of the switching field distribution. Schematically (a), the sample can be manipulated into any desired state, by writing the strongest islands first (I) using a large bias field  $H_a$ , and subsequently weaker islands are rewritten at decreasing bias (II-V). In each step the islands in  $H_s < H_s \leq H_a + H_t$  (red islands in the images/distributions) are written, not affecting previously written islands ( $H_s > H_a + H_t$ , green), but erasing weaker islands ( $H_s \leq H_a$ , blank); updates are impossible and outside the written area islands have random magnetization. In experiment (b), this method allowed us to write “University of Twente.” in an abbreviated form.

tips. This is in agreement with our model, which predicts that the write bubbles are smaller than the island, and grow with increasing tip thickness. Only for thick (e.g.  $\geq 80 \text{ nm}$ ) coatings, the bubbles have sufficient strength during the full motion of the cantilever.

In non-contact mode, the equivalent field of a 35 nm tips is 18 to 30  $\text{kA m}^{-1}$  at  $z \approx 65 \text{ nm}$ . The equivalent field is independent of the applied field, over the entire range of switching fields from 150 to 300  $\text{kA m}^{-1}$ . This is in agreement with the model, which predicts that at a tip-sample distance of 65 nm the write bubbles are much larger than the island.

Our model shows that the effective tip height during writing is larger than during read back, by as much as a factor of two. In contrast to read back, the

dependence of the write field on the tip thickness is no longer linear for small distances to the tip apex.

Not only do the MFM tips reverse the magnetization in the islands, which is desired, also undesired influence of the stray fields of the islands on the tips was observed. We observed for some of the 80 nm tips reversible sample-tip interactions, where the magnetization of the tip is reduced, as well as irreversible interactions, due to wear of the tip. Helium ion micrographs show that thicker coatings extend further beyond the silicon tip, which indeed could make them more prone to wear.

When using side coated MFM tips for write experiments on patterned islands, we find that the effective write field increases with tip thickness, as expected. The increase is however not linear, and when the tip thickness reaches 80 nm, undesired island-tip interaction occurs. Reliable manipulation of islands with tips having thinner side-coatings is only possibly via elaborate writing schemes. Therefore, for successful field assisted writing by MFM, a narrow switching field distribution of the islands is of primary importance, as it is for magnetic recording on bit patterned media.

## 6.6 Acknowledgment

I and my colleagues would like to thank J. de Vries for fabrication and characterization of the samples, and G. Hlawacek and V. Veligura for HIM imaging. This research is supported by the Dutch Technology Foundation STW, applied science division of NWO and the technology program of the Ministry of Economic Affairs.



## Chapter 7

# Simulating 3D self-assembly of shape modified particles using magnetic dipolar forces

### Abstract

The work described in this chapter has been done together with Tijmen Hageman, Per Loethman, and Leon Abelmann. We investigated the feasibility of 3D self-assembly of magnetic particles that interact via magnetic dipolar forces. Typically magnetic particles, such as isotropic spheres, self-organize in stable 2D configurations. By modifying the shape of the particles, 3D self-assembly may be enabled. The magnetic configurations of simple particle arrangements are obtained via energy minimization in simulations. The outcome of the simulations is in agreement with a demonstration using magnetic spheres of centimeter radius. The simulations show that a 3D configuration can become energetically favorable over 2D configurations, if the particles are indented so that their shape approaches a tetrahedron.

### 7.1 Introduction

Microfabrication techniques are currently based on top-down lithography and therefore inherently two dimensional (2D), or at best very restricted in the third dimension. Fabrication by means of three dimensional (3D) self-assembly will open up a wide range of new applications, such as new types of (smart) super-materials with interesting optical, mechanical, electrical and magnetic properties [Elwenspoek et al., 2010]. On the long term, we envision 3D electronics as an answer to atomic limits emerging at the end of Moore's law progress [Abelmann et al., 2010].

In this study, the focus is on 3D self-assembly driven by dipolar magnetic forces. Particles that interact by dipolar forces only, typically assemble in 2D



**FIGURE 7.1 –** *Photographs of simple configurations of toy magnets ('neocubes') with a diameter of 4 mm. All the configurations are stable, except for the two rightmost configurations (including the 3D configuration (dashed box)); when the magnets are forced in one of these meta-stable configurations, they readily rearrange when touched.*

configurations [Pelesko, 2007]. Some simple configurations of milli-magnetic particles are shown in figure 7.1. When experimenting with these toy magnets (neocubes), we discovered that a three-dimensional configuration of four spheres is meta-stable. In this chapter we investigate by means of simulations, whether a four particle system could be stable if the shape of the particle is modified.

Section 7.2 describes the design of the particles and a setup to investigate magnetic self-assembly on the centimeter scale. In simulations, we treat the particles as magnetic dipoles, and explore the stability of particle configurations by minimizing the magnetostatic energy. Section 7.3 discusses the theory and simulation method. In section 7.4, the results of simulations and experiments are presented and discussed. First, we consider spherical particles (section 7.4.1) and their stable configurations. Subsequently, we demonstrate assembly of four particles on the centimeter scale (section 7.4.2). Finally (section 7.4.3), we allow the particles to have a modified (non-spherical) shape, and we investigate the requirements to attain a 3D configuration that is energetically favorable over 2D configurations.

## 7.2 Self-assembly experiment

### 7.2.1 Experimental setup

To demonstrate the theoretical predictions in this chapter, we performed a 3D self-assembly experiment on the centimeter scale. The particles are cylindrical magnets with an axial magnetisation enclosed in a non-magnetic shell, see figure 7.2.

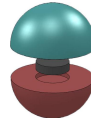


FIGURE 7.2 – *Exploded view of the magnetic particle used in the simulations. Shown are the permanent magnet and the non-magnetic encapsulation, which consist of two half-spheres. This type of particle can be easily produced by 3D printing.*

TABLE 7.1 – *Design specifications of the simulated particle, and the maximum force of two particles in contact (i.e.  $2r$  center-to-center separation) with their cylindrical magnets axially aligned [Vokoun et al., 2009].*

|                                 |                        |
|---------------------------------|------------------------|
| particle radius, $r$            | 9.25 mm                |
| magnet radius, $D/2$            | 2 mm                   |
| magnet height, $t$              | 4 mm                   |
| saturation magnetization, $M_s$ | $1.35 \text{ T}/\mu_0$ |
| maximum magnetic force          | 15 mN                  |

The particles are fabricated by 3D printing and the magnets are commercial neodymium (NdFeB) permanent magnets ([supermagnete.de](http://supermagnete.de)). The parameters of the particles are listed in table 7.1.

The 3D printing technology will in the future allow for easy modification of the shape of the particles. Besides this, the plastic encapsulation reduces the mass density of the particles (compared to solid NdFeB spheres), which allows us to avoid the (quick) sedimentation of the particles in self-assembly experiments in water.

Since the average density of the particles cannot be set exactly equal to that of water, we chose to make them slightly heavier and levitate them against gravity in an upward water flow. This flow of  $19.7(5)$  cm/s is generated by a conventional water pump connected to a transparent cylinder with a inner diameter of 17.5 cm, see figure 7.3. To prevent particles from escaping the observation area, nets are positioned in the cylinder.

Because of the inlet of water into the tube, the presence of the bottom net and the flow itself, turbulence is generated that disturbs the system of magnetic particles out of its local minima.

## 7.2.2 Video analysis

Two orthogonally placed cameras record sequences of images of the particles in the observation area, at a rate of 5 frames/s. Since the determination of the position of four objects in a three-dimensional space is far from trivial, and

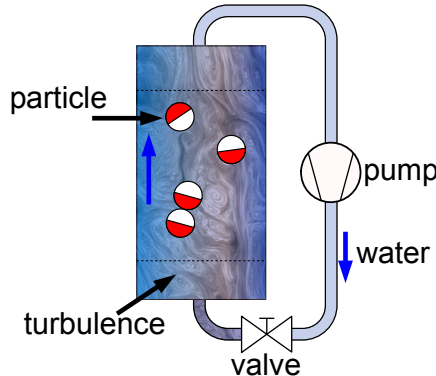


FIGURE 7.3 – Schematic layout of the 3D self-assembly experiment. The 3D printed particles are inserted in a transparent cylinder, and levitated against gravity by an upward flow generated by a pump. The flow generates turbulence, that acts as a disturbing energy to drive the system out of local minima.

the aim of the experiment is merely a demonstration, we chose to perform the image analysis manually.

Sets of 2200 images were randomly chosen from the six hour observation. Six colleagues were asked to observe the images from both cameras, and decide whether there was a ring of four particles (“ring”)\*, a line of four particles (“line”), or neither of the two (“none”). A majority voting method was used to combine the six individual observations. In the analysis there were 429 “none” votes (19.5% of all decisions). Severely conflicting situations, in which ring and line configuration both received more than one vote, did not occur. Instances in which the ring as well as the “none” configuration received three votes (8.0% of the total observations) were decided in favor of the ring. Similarly for the line versus “none” decision, which was rare however (0.7%).

In case the disturbing energy is large compared to the energy difference between “ring” and “line” configurations, we expect an equal occurrence of lines and rings. For the set of 1771 observations this case leads to an uncertainty of 2.3% on the observed average occurrence, at a confidence level of 95%.

## 7.3 Simulation theory and procedure

### 7.3.1 Magnetostatic energy of dipoles

For simplicity, we approximate the moment of the cylindrical magnets of the particles by dipoles. The magnetostatic energy of a single dipole in a magnetic

---

\*We will call this diamond configuration a “ring”, since this is the  $N = 4$  particle approximation of a circle in which the dipoles form a flux closing configuration.

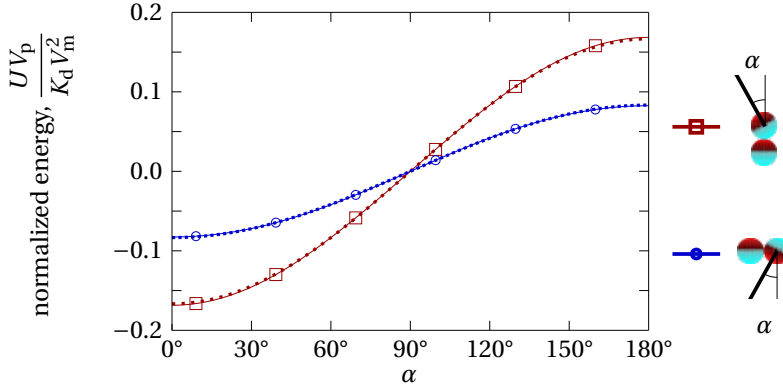


FIGURE 7.4 – Energy of two particles in axial (squares) and radial (circles) configurations against angle  $\alpha$ , which defines the tilt of the magnetization of one of the particles, see insets. Approximating the axially magnetized cylindrical magnets by dipoles (dotted lines) results in energies accurate within 1 % at the extrema of the exact energies (solid lines), for the particle and magnet dimensions in table 7.1.

field is given by

$$U = -M\hat{\mathbf{m}} \cdot \mathbf{B}, \quad (7.1)$$

where  $M = M_s V_m$  is the magnitude of the dipole moment, with  $V_m$  the volume of the cylinder;  $\hat{\mathbf{m}}$  is the unit vector in the direction of the dipole moment and  $\mathbf{B} = \mu_0 \mathbf{H}$  is the magnetic field at the position of the dipole. This magnetic field is caused by the other dipoles in the system. The field of a single dipole is given by

$$\mathbf{B} = \frac{\mu_0}{4\pi} \frac{M}{|\mathbf{r}|^3} (3\hat{\mathbf{r}}(\hat{\mathbf{m}} \cdot \hat{\mathbf{r}}) - \hat{\mathbf{m}}), \quad (7.2)$$

where  $\mathbf{r}$  is the vector from the dipole to the point where the field is evaluated, and  $\hat{\mathbf{r}} = \mathbf{r}/|\mathbf{r}|$ . The total magnetostatic energy of a configuration of particles can be obtained by summing the energies of all interacting dipole-pairs in the configuration.

In figure 7.4, we compare the dipole approximation of the energy to the exact energy (calculated in Appendix D). The exact energy calculation takes the cylindrical shape of the magnets into account. The exact and approximate curves are very similar, however the dipole approximation results in a slightly smaller difference between the energy minima of the configurations. In order to obtain quantitative results, the accuracy of the simulations can be improved by taking the exact energy in account for particles that are in contact.

### 7.3.2 Energy minimization procedure

The preferred magnetic configuration (that is, the orientations of the magnetic moment of the particles) is found by minimizing the total magnetostatic energy of the configuration dynamically. Only the torques on the dipoles are considered and not the forces. In other words, the positions of the particles are fixed in the simulations and the particles can only lower their energy via rotation. The energies of particle trajectories are obtained by series of such minimizations. In a series the particle positions are manually altered according to a pre-defined path. To determine stable positions and relevant trajectories of the particles, we use the observed configurations of the neocubes in figure 7.1 as a guide.

This magnetostatic energy is minimized by allowing the dipole moments to rotate in the direction of the net field via

$$\frac{\Delta \hat{\mathbf{m}}}{\Delta t} = -\alpha \hat{\mathbf{m}} \times (\hat{\mathbf{m}} \times \mathbf{H}). \quad (7.3)$$

After each iteration step  $\Delta t$ , a new configuration of the dipole moments is calculated ( $\hat{\mathbf{m}}_{t+\Delta t} = \hat{\mathbf{m}}_t + \Delta \hat{\mathbf{m}}$ ). This configuration results in a new field  $\mathbf{H}$  for the next iteration step. The damping factor  $\alpha$  is manually adjusted to optimize simulation speed while maintaining convergence. Typically,  $\alpha \Delta t = 10^{-4}(\text{A/m})^{-1}$ . The simulation is stopped after 10000 steps, or when the change in the total magnetization is below a certain tolerance:

$$\sum_{n=1}^N |\Delta\phi_n| + |\Delta\theta_n| < 10^{-5} \text{ rad}, \quad (7.4)$$

where  $N$  is the number of dipoles in the configuration and  $\phi$  and  $\theta$  are the angles defining the direction of dipole moment;  $\Delta\phi$  and  $\Delta\theta$  are the changes of these angles in a single time step.

The energy does not necessarily converge to a global minimum, but could get stuck in a local minimum. Therefore, the simulations are repeated several times, with random initial dipole moments, to find the magnetic configuration with the lowest energy.

## 7.4 Results and discussion

The energies corresponding to the simple configurations in figure 7.1 have been simulated first. The distance between two neighboring particles in these configurations is  $2r$ . Table 7.2 shows the final magnetization state of the simple configurations and the corresponding energies. The energies are proportional to  $K_d \equiv \mu_0 M_s^2 / 2$  and  $V_m^2$ , and inversely proportional to the volume of the spherical particle,  $V_p$ . The configuration with the lowest energy for  $N = 3$  is the “line” configuration in 3.a. For  $N = 4$  the “ring” configuration in 4.b has the lowest energy. Configuration 4.c and the 3D configuration 4.d have higher energy than configuration 4.b, as was expected from our experience with the neocubes.

TABLE 7.2 – *Magnetic configurations and normalized magnetostatic energies after energy relaxation; in all configurations the dipoles are positioned in plane, except for the 3D configuration 4.d.*

| configuration |   | magnetostatic energy<br>$UV_p/K_d V_m^2$ |
|---------------|---|--|
| 3.a           |  | -0.35                                    |
| 3.b           |  | -0.31                                    |
| 4.a           |  | -0.55                                    |
| 4.b           |  | -0.56                                    |
| 4.c           |  | -0.53                                    |
| 4.d           |  | -0.42                                    |

### 7.4.1 Energy barriers

The energy barrier between configuration 3.a and 3.b has been investigated, see figure 7.5. The trajectory is parametrized by angle  $\theta$ , which is defined in the figure. For each  $\theta$ , the lowest energy state is found via the simulations. Both the 3.a and 3.b configurations correspond to a minimum in the energy landscape. This means that these configurations are stable. The maximum energy is attained for  $\theta = 105^\circ$ .

For the 4-dipole system, two trajectories are considered. In the first trajectory, an in-plane path from configuration 4.b to 4.c is parametrized. The energy corresponding to this trajectory is given in figure 7.6. At  $\theta = 120^\circ$ ,  $U(\theta)$  has a local maximum. Therefore, the configuration of 4.c is not stable. This is in correspondence with the observed meta-stable behavior of the neocubes in this configuration.

The second trajectory is a path from configuration 4.b to 4.d. The final configuration is ‘3D’, since the dipoles move out of the plane. The energy and the parametrization are given in figure 7.7. The energy attains a maximum at  $\theta = 90^\circ$ , so the 3D configuration is only meta-stable. This is again in correspondence with the behavior of the neocubes.

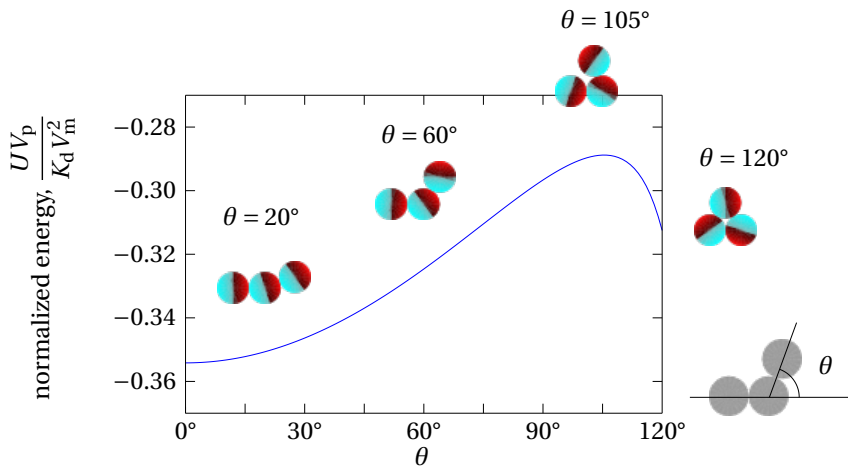


FIGURE 7.5 – Trajectory in the energy landscape of a 3-dipole system; the energy is plotted against  $\theta$ , which is defined in the lower right. The insets show the configuration of the particles for various  $\theta$ , after minimization of the energy.

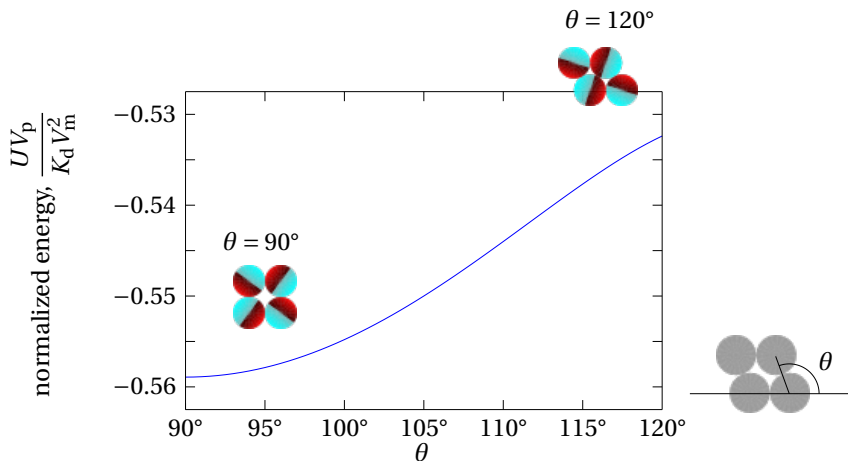


FIGURE 7.6 – The in-plane trajectory in the energy landscape of a 4-dipole system. The energy is plotted against  $\theta$ , which is defined in the lower right inset. The magnetic configurations after energy minimization for  $\theta = 90^\circ$  and  $\theta = 120^\circ$  are also shown.

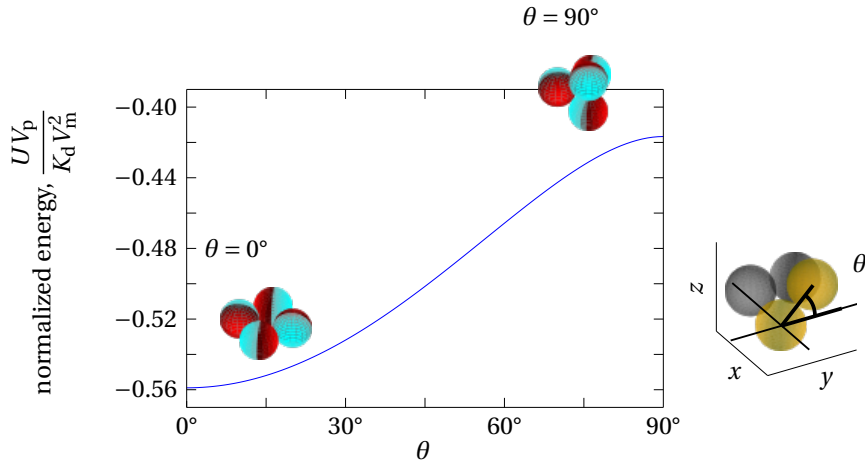


FIGURE 7.7 – The out-of-plane trajectory in the energy landscape of a 4-dipole system. The energy is plotted against  $\theta$ , which is defined in the lower right inset. The magnetic configurations after energy minimization for  $\theta = 0^\circ$  and  $\theta = 90^\circ$  are also shown.

## 7.4.2 Experimental verification

Four 3D printed particles with embedded magnets and dimensions as in table 7.1 were inserted in the upward turbulent flow for a total of six hours. Figure 7.8 shows representative snapshot of the video recording. Next to occasional disconnected sets (top left image), we mostly observed connected spheres in either a line or ring configuration.

The video recording was analyzed by six colleagues for occurrence of lines or ring configurations (situation 4.a or 4.b in table 7.2), or none of these. The result is shown in figure 7.9. There is considerable ambiguity in what people regard a line configuration, resulting in quite a large variation between observers. To deal with this issue, we adopted a majority vote system, shown on the right. From the voting, we conclude that the chance of observing a line or a ring is practically identical, which is in agreement with the very small difference in energy of both states (Table 7.2, state 4.a and b).

## 7.4.3 Shape modifications

From figure 7.7 we conclude that the 3D configuration with four dipoles is not stable. We continue to investigate whether this 3D configuration can be made stable by modifying the shape of the particles. Moreover, if the energy of the 3D configuration can be reduced in this way, the 3D configuration might become energetically favorable over the 2D configurations.

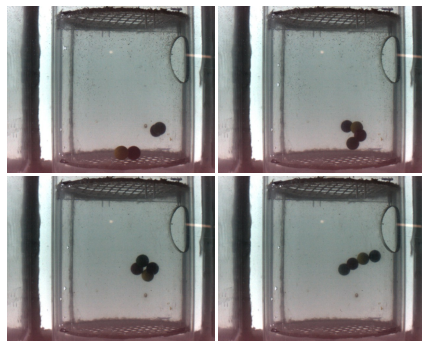


FIGURE 7.8 – Shapshots of four spheres in the self-assembly reactor setup. The spheres have embedded magnets, and are levitated by an upward water flow. Turbulence in the flow provides the disturbing energy for the system, so that it can explore the energy landscape. The bottom images show the ring and line configurations that are analyzed further in this chapter.

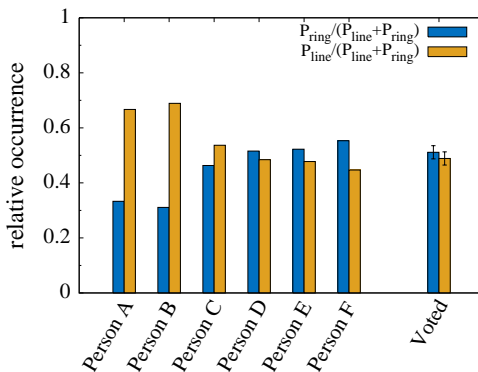


FIGURE 7.9 – Relative occurrence of lines and rings, according to six different observers. On the right the majority vote over the six observations is shown. The error bars represent the standard deviation in the set of results obtained by randomly leaving a single person out of the voting process. Clearly, the ring and line configurations are observed almost equally, which is in agreement with the small difference in energy between configuration 4.a and 4.b in table 7.2.

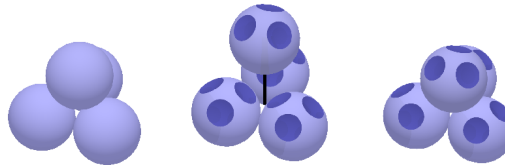


FIGURE 7.10 – Illustration of a shape modification. The unmodified particles (left drawing) can be indented to allow a closer packing of the spheres (right drawing). By making 3 indentations, the shape of a particle is approximately a tetrahedron, which could possibly be used as a building block for larger assemblies. The exploded view (center drawing) shows the indentations and the simulated vertical trajectory (line) of the top particle.

Figure 7.10 illustrates a possible shape modification; the particles have been indented at three positions. With such a modification, the top particle can be positioned closer to the 3 bottom particles. This results in a lower energy.

The effect of this shape modification is investigated by simulating a trajectory. The 3 bottom dipoles are configured in a ring, with their centers in the  $x$ - $y$  plane. The top particle moves vertically in the  $-z$  direction, as illustrated in figure 7.10. At each position the energy is minimized and  $U(z)$  is obtained, where  $z$  is the distance between the center of the top particle and the  $x$ - $y$  plane. At  $z/r = 2/3\sqrt{6}$  the top particle touches the bottom particles if the particles have their unmodified spherical shape. To allow a smaller distance  $z$ , the shape of the particles must be modified.

Figure 7.11 shows the energies versus  $z/r$  that are obtained for two situations. In the first situation, all dipole moments are free to rotate. In the second situation, the magnetization of the top particle is fixed in the  $z$  direction. This is of interest, because the modification of the particles defines a preferred orientation of the dipole moment. However, the constraint of having preferred orientations of the dipole moments can be resolved by designing particles that contain magnets which are free to rotate with respect to the shell.

The energies of the two cases are compared with the 4-dipole ring configuration (4.b. in table 7.2), since this is the 2D configuration with the lowest energy. In case that the top particle has a fixed magnetization in the  $z$ -direction, the energy is always larger than the energy of the ring configuration (horizontal line in figure 7.11). However, in the case where all particles are free to rotate their dipole moments, the energy is lower than the ring configuration if  $z/r \leq 1.28$ . Therefore, for particles with a rotatable magnet and a modified shape, the 3D configuration is preferred over the 2D configurations.

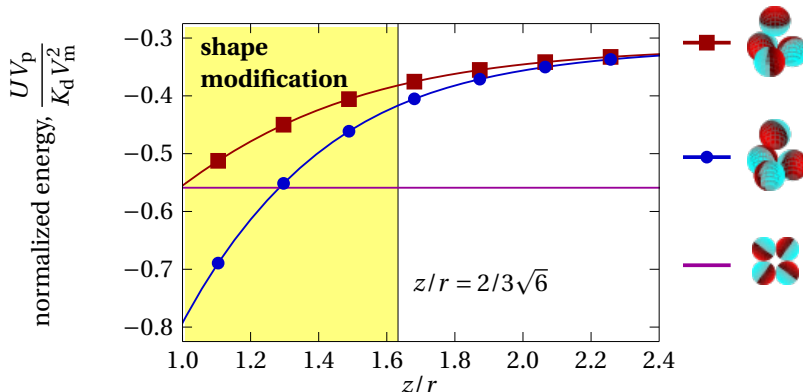


FIGURE 7.11 – Energy versus  $z$  position of the top dipole in the 3D configuration with 4 dipoles. In the ‘free’ case (circles) all dipoles were free to rotate their dipole moment during the energy minimization; in the ‘fixed’ case (squares), the moment of the top dipole was fixed the  $z$  direction during the energy minimization. The shaded area indicates the region where the shape of the particles needs to be modified. The horizontal line indicates the energy of the 4-dipole ring configuration.

## 7.5 Conclusions

We theoretically analyzed whether particles with dipolar magnetostatic interaction can form three-dimensional structures. The magnetostatic energies of simple particle configurations are obtained via simulations by dynamic minimization.

The simulations show that for a four sphere system the 2D line and ring configurations have approximately equal energies. All investigated 2D configurations are energetically favored over a 3D structure, which is meta-stable.

The theoretical observations are confirmed by a demonstration using centimeter sized spheres levitated in a turbulent flow. Indeed, the 3D configuration is never observed, and occurrence of lines and rings is approximately equal.

The video data from the demonstration experiment was manually analyzed by six persons, rather than a computer algorithm. Despite the simple task to discriminate lines from spheres and large data set, there was significant variation between observers.

Theory shows that if the particles are indented, so that they start to approach a tetrahedral shape and the magnets are free to rotate inside the particles, a stable 3D configuration can be obtained. This results encourages further macro scale experiments using 3D printed particles with embedded spherical magnets.

## 7.6 Acknowledgment

I and my colleagues would like to thank Mathijs Marsman for the idea to use magnetic particles with embedded magnets, initial experiments and many discussion, as well as Léon Woldering for the realization of the experimental setup, the concept to use indented particles and numerous discussions. Without these talented colleagues, this research would not have been possible. I would also like to thank Yannick Klein, Christian Marger, Tim Mehlhorn and Marc Pichel for diligent manual observation of the recorded video data.

This research is supported by the Dutch Technology Foundation STW, which is part of the Netherlands Organisation for Scientific Research (NWO), and which is partly funded by the Ministry of Economic Affairs



# Chapter 8

## Using magnetic levitation for 2D and 3D self-assembly of cubic silicon macroparticles

### Abstract

This chapter is based on [Woldering et al., 2016] \*, in which I contributed in the determination of the magnetostatic energies of the assemblies. Today's micro- and nano-fabrication is essentially two-dimensional, with very limited possibilities of accessing the third dimension. The most viable way to mass-fabricate functional structures at the nano-scale, such as electronics or MEMS, with equal feature sizes in all directions, is by three-dimensional self-assembly. Up to now, three-dimensional self-assembly has mainly been restricted to crystals of polymer spheres. We report on two- and three-dimensional self-assembly of silicon cubes, levitated in a paramagnetic fluid. We demonstrate the benefits of templating and study the effect of a change in hydrophilicity of the cubes. These experiments bring us one step closer to three-dimensional self-assembly of anisotropic, semiconducting units, which is a crucial milestone in overcoming the scaling limits imposed by contemporary 2D microfabrication.

### 8.1 Introduction

Self-assembly is the process in which units such as atoms, molecules, colloidal or microfabricated particles spontaneously form organized structures [Pelesko, 2007]. The final shape and properties of the resulting structure is entirely determined by the properties of the individual units, and not by external (human) direction.

---

\*This work is published in Woldering L.A., Been A.J., Alink L., Abelmann L., 2016 “Using magnetic levitation for 2D and 3D self-assembly of cubic silicon macroparticles” *Physica status solidi RRL* **10**, p. 176.

Self-assembly occurs at all length scales, from the tiniest molecules to entire galaxies [Whitesides and Grzybowski, 2002]. In this chapter, we study the three-dimensional self-assembly of anisotropic silicon particles as a fabrication technique for 3D silicon micromachining. Self-assembly of microfabricated objects in two dimensions has received wide attention with promising results [Goldowsky et al., 2013; Tkachenko and Lu, 2015] and very complex shapes [Mastrangeli et al., 2014]. The transition to three dimensions is of technological importance for complex structures such as photonic band gap materials [Vlasov et al., 2001; Woldering et al., 2011], metamaterials fabricated from cubic building blocks [Belov et al., 2013], three-dimensional electrical networks [Gracias et al., 2000] and 3D cross-point architectures for computer memories [Abelmann et al., 2010]. Processes for 3D silicon microfabrication are necessary in order to overcome the scaling limits imposed by 2D microfabrication [Elwenspoek et al., 2010; Park et al., 2004].

For self-assembly, four elements are critical: the characteristics of the individual units, the driving forces which bind the units, the disturbing forces which allow the units to find their optimal position, and the environment in which the self-assembly takes place [Pelesko, 2007]. Organized structures are obtained when these four elements are properly tuned. For submicrometer sized particles, the gravitational force is small compared to drag forces and sedimentation of particles is slow [Vlasov et al., 2001]. However, in our research we use particles of several hundred  $\mu\text{m}$ . At these length scales, sedimentation takes place too rapidly, and has an undesired effect on the outcome of the self-assembly experiments. Therefore there is a need to counteract gravity in these systems. To this end we employ the magneto-Archimedes levitation [Ikezoe et al., 1998] in a paramagnetic fluid, sometimes also called diamagnetic levitation [Hennek et al., 2015; Peltine, 2004; Subramaniam et al., 2014]. Preferably the term magneto-Archimedes is used, since strictly speaking the levitated objects do not have to be diamagnetic, as long as they are less paramagnetic than the surrounding fluid. The magneto-Archimedes effect also provides a driving force pushing the particles towards each other [Ilievski et al., 2011b; Mirica et al., 2011].

Magnetic forces are increasingly used in self-assembly. For instance, assembly was performed using magnetic nanoparticle fluids [Yang et al., 2013], magnetite nanocubes have been self-assembled into helical superstructures [Singh et al., 2014], a macro scale Zeeman slower was fabricated from permanent magnets [Lebedev and Weld, 2014], and colloidal assembly was directed by magnetic moulds [Demirörs et al., 2013].

In this chapter, the 2D and 3D self-assembly of levitated silicon macroparticles is discussed. Since the magneto-Archimedes driving force in our system is axi-symmetric, we expect the target structures to be cubic closed packed disc-like (2D case) or ellipsoid-like (3D case) structures, built from the constituent macroparticles. The submillimeter particles were levitated in a paramagnetic fluid. These particles have a much higher density than commonly used [Ilievski et al., 2011b; Mirica et al., 2011]. Early results indicated that the levitated 3D

self-assembly of these macrocubes is very challenging [Woldering et al., 2014]. Therefore, in order to increase the quality of the resulting 3D crystals, the particles were made less hydrophilic. This reduction in hydrophilicity introduces additional binding forces between the particles that are in contact, as was demonstrated by means of the self-assembly of hydrophobic silver nanocubes [Rycenga et al., 2008] and other anisotropic shapes [Clark et al., 2001].

Successful 2D and 3D templated self-assembly is demonstrated in this chapter, as well as the 3D levitated self-assembly of silicon macrocubes. These results are the first ever 3D self-assembly of silicon particles with an anisotropic shape by means of magnetic levitation. This method is a promising route towards 3D micromachining of silicon aided by self-assembly.

## 8.2 Experimental

The self-assembly experiments were performed in a home-built setup, fabricated from aluminum, schematically depicted in figure 8.1. In this setup a cuvette filled with a paramagnetic liquid and up to 54 diamagnetic silicon macrocubes was positioned between two NdFeB magnets. These magnets were obtained by stacking 5 smaller cylindrical magnets, resulting in a stack with a total length of  $l = 35\text{ mm}$  and a radius of  $D/2 = 12.5\text{ mm}$ . The magnetic field strength at the edge of the magnets was measured with a Gauss meter to be 1.25 T. By placing these stacks of magnets so that similar poles face each other, a magnetic field gradient is obtained in the cuvette. The gradient and point of zero field was adjusted by changing the distance between the magnets from 14 to 22 mm by raising magnet 1.

The silicon particles are pushed towards a position on the central axis between the two magnets as a result of the magnetic field gradient inside the paramagnetic medium. This is the position where the magnitude of the magnetic field is lowest<sup>†</sup>. Since all particles are forced towards this central region, an effective pressure exists that keeps the particles in close contact.

By changing the separation  $h$  between the two magnets, the magnetic field gradient can be altered, which aids attempts to obtain the target structures. The paramagnetic fluid used is a 2 mol/L solution of GdCl<sub>3</sub> (Sigma Aldrich G7532, gadolinium(III)chloride hexahydrate 99%) in demineralized water. The relatively strong susceptibility of this fluid enhances the susceptibility contrast between the diamagnetic macrocubes and the paramagnetic liquid environment.

In order to introduce vibrations into the system, one end of the cuvette is pressed against a piezo-actuator (FPA-0150E-S-0518-150-SS-1M3 FlexFrame PiezoActuator, dynamic, structures & materials, LLC).

The electric capacity of the piezo-element is 1.8 µF A spring ensures that the cuvette is kept in position while the piezo-element is actuated. The actuation frequency and amplitude are generated by means of a waveform generator (Agilent A33220A), which is connected to a 10× high voltage amplifier (SyLAB

---

<sup>†</sup>The actual position of assembly is slightly lower due to gravity.

LM3325). Typically the piezo-element was actuated for 30 minutes. Care was taken to prevent strong oscillatory fluid flows, which typically results in an undesired alignment of particles at the nodes of the resulting standing waves. We determined an actuation frequency of 300 Hz with a peak to peak voltage of 130 V to be optimal for self-assembly. From this voltage and the capacity of the piezo-element, we can estimate that the upper limit in the disturbing energy in the system is in the order of 15 mJ.

The macrocubes were diced from a double-sided polished silicon wafer (p-type,  $\langle 100 \rangle$ , resistivity = 5–10  $\Omega$  cm). The dicing procedure was optimized in order to make sure that the particles are as close as possible to a cube and that the diced surfaces be as smooth as possible. To obtain the cubes, first the average thickness of the wafer was determined around the edge of the wafer by a micrometer caliper to be 525  $\mu\text{m}$ . The manufacturer specifies a thickness variation over the entire wafer of less than 5  $\mu\text{m}$ . Subsequently, the wafer was diced so that edges were obtained with lengths equal to the measured average thickness of the wafer. For dicing, we employed a Loadpoint Micro Ace 3 dicing saw, equipped with an F1230 blade. The blade was operated at 32 000 rpm at a feed rate of 1 mm/s. Any residual dicing foil was removed using a piranha solution ( $\text{H}_2\text{SO}_4$  (conc): $\text{H}_2\text{O}_2$  (30%) = 4:1, temperature = 100 °C, 10 min), followed by rinsing. The particles were stored in demineralized water. Inspection by scanning electron microscopy (FEI Quanta 450) confirmed that the particle size was as designed within measurement error (519(10)  $\mu\text{m}$ ).

In order to optimize the dicing process for flatness of the cubes, the morphology of the resulting surface was analyzed by means of scanning electron micrographs (FEI Quanta 450). Atomic force microscopy (AFM, Dimension 3100) on a face of a single particle resulted in a RMS roughness of 12.6 nm over a 10  $\mu\text{m}$  scan range, with a peak-peak value of 460 nm.

Due to the native surface oxide, the water wets the silicon cubes completely (contact angle of 0°). Some of the cubes were made less hydrophilic by means of chemical functionalization with hexamethyldisilazane (HMDS) [Awomolo et al., 2007; Hertl and Hair, 1971].

To begin with, the macrocubes were heated on a hot-plate at 70(20) °C to remove any adsorbed water from the surface. Subsequently, the particles were immersed in pure HMDS (BASF, VLSI Selectipur). The surface reaction between the silicon and HMDS was allowed to proceed for one minute while stirring, after which the suspension was poured on top of a Whatman general purpose filter paper. The residual HMDS was quickly removed by rinsing the particles with excess acetone (VWR Chemicals, Technical grade, 99 %) and isopropyl alcohol (Merck Millipore, for analysis, 99.8%). The macrocubes were dried in air.

This chemical reaction was also performed on a whole, unprocessed wafer. This wafer allowed the contact angle of a droplet of water on the silicon surface to be measured before and after the reaction, in order to characterize the change in hydrophilicity. The contact angles were measured using a Metrology Dataphysics OCA-20. After the one minute HDMS treatment, the surface

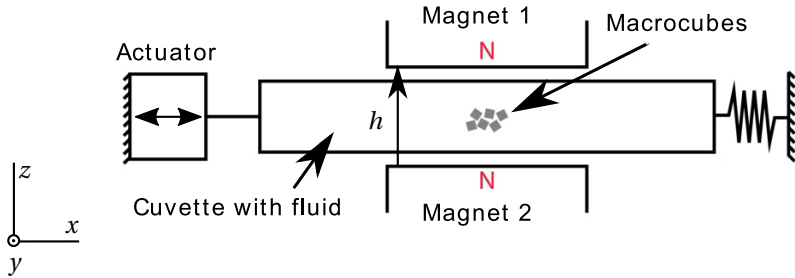


**FIGURE 8.1 – Schematic illustration of the home-built setup. Silicon macrocubes are introduced to a cuvette with a square cross-section that contains a paramagnetic liquid. The cuvette is positioned between two magnets that are placed with similar poles facing. The resulting magnetic field gradient causes the particles to be forced towards a central region between the two magnets, labeled Magnet 1 and Magnet 2. A piezo-actuator introduces vibrations into the cuvette, which allows self-assembly to occur. Cameras were used to visualize the self-assembly process and the resulting arrays of particles.**

became less hydrophilic with a contact angle of 53°.

The macrocubes were used for several 2D and 3D self-assembly experiments. In this chapter, four different experiments are reported:

- Measuring the levitation height of single macrocubes as a function of the magnet separation  $h$ .
- Templated 2D self-assembly of macrocubes on the bottom of the cuvette.
- Templated 3D self-assembly of macrocubes on the bottom of the cuvette.
- Levitated 3D self-assembly of macrocubes.

Typically, around 54 macrocubes were used for the self-assembly experiments.

The levitation heights of single silicon macrocubes were measured by means of non-magnetic, synthetic calipers (WIHA, Vernier Calipers #41103). Two cameras were used to observe the self-assembly experiments: a Dino-lite pro USB microscope and a Nikon 1 J2 compact flash camera. The latter was equipped with a Macro-Switar 1:1.9 CMT lens (focal length = 75 mm) and an 85 mm extension tube. The results were stored as photographs, see for example figures 8.3 and 8.6.

## 8.3 Results and discussion

### 8.3.1 Levitation of single macrocubes

Single, non-surface treated macrocubes were levitated in the paramagnetic fluid with different magnet separations. The resulting measured particle lev-

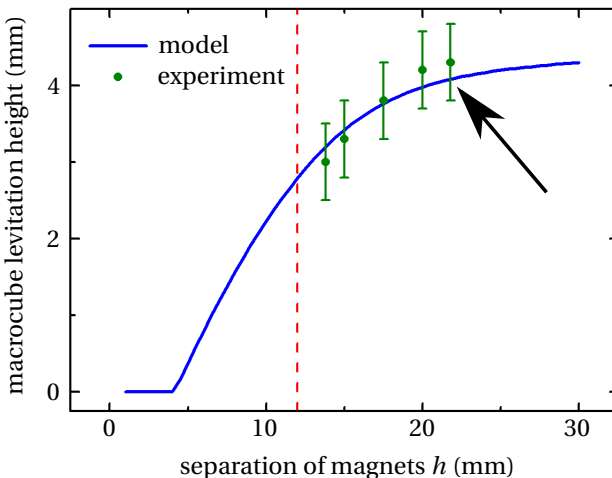


FIGURE 8.2 – Measured levitation height (green dots) of a single silicon macrocube as a function of magnet separation  $h$ . The measured data is compared to values expected based on our theoretical model (solid line). The dashed line is the minimum separation of the magnets, as dictated by the dimensions of the cuvette. The maximum separation is indicated by the arrow.

itation heights are plotted in figure 8.2. The separation distance  $h$  between the two cylindrical magnets was changed by raising magnet 1. As a result, the point of zero field is raised as well. In this way levitation heights over 4 mm could be achieved. The measured heights are compared to the expected values based on a magneto-static model, which takes into account the distribution of magnetic field energy throughout the area of interest. The model neglects magnetic interparticle interactions and assumes that the particles are small, so the force density is constant over the volume of the particle. Details can be found in appendix E.1. The theoretical and measured values are found to be in excellent agreement, see figure 8.2, which confirms that our model provides a good description of the experiment.

### 8.3.2 Two-dimensional self-assembly

Two-dimensional self-assembly of macrocubes was performed on the bottom of the cuvette. The cuvette acts as a template and makes sure that all the particles are positioned in the same plane. Figure 8.3.a <sup>‡</sup> is a photograph of the

<sup>‡</sup>In addition, a video of the self-assembly process can be found online in the accompanying material (SA\_2D\_Templated) of reference [Woldering et al., 2015].

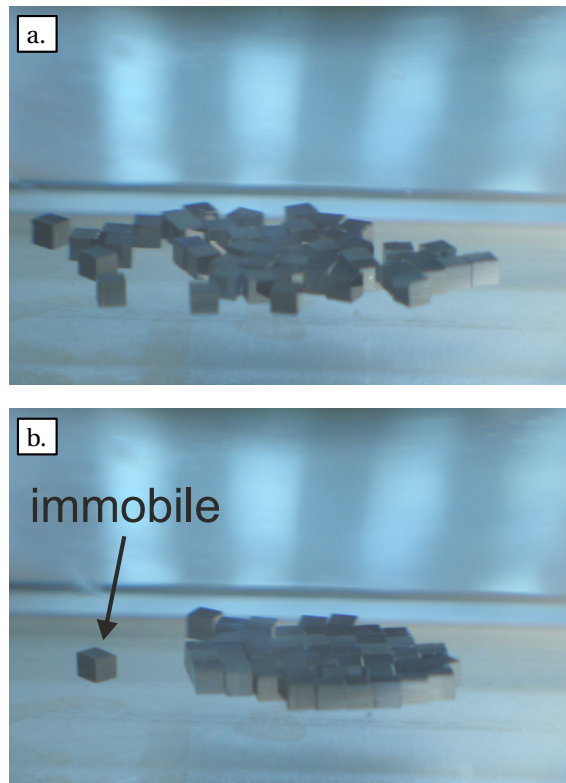


FIGURE 8.3 – (a) Collection of randomly distributed silicon macrocubes before 2D self-assembly. The particles are lying on the bottom of the cuvette, which acts as a template. The macrocubes are surface treated to make them less hydrophilic and have edges of  $525(10)\text{ }\mu\text{m}$ . (b) Array of silicon cubes after self-assembling for 20 minutes. During this time the piezo-actuator was operated in order to introduce a vibration to the system. The particles are aligned next to each other in a square distribution. Deviations from the ideal configuration are observable.

macrocubes on the bottom of the cuvette before self-assembly. It is apparent that the particles are randomly positioned, resulting in a high amount of disorder. Figure 8.3.b is a photograph of the macrocubes after self-assembly for 20 minutes. The generated vibrations allow the particles to optimize their position in the magnetic field, that is, find those positions where the total energy of the array is as low as possible. In the final array, the particles have aligned themselves neatly next to each other, resulting in a square distribution of the macrocubes, which is the target configuration. Some deviations from the ideal square distribution are observable.

The theoretical model employed in the previous section is also used to ana-

lyze the magnetic energy of these templated 2D arrays. In this case the model is modified slightly in order to take the rotational orientation of the cubes into account. Details can be found in appendix E.2. We have analyzed the magnetic energy of the 2D array of macrocubes at intervals of 50 seconds for a 1500 seconds self-assembly experiment, see figure 8.4. In these photographs, the position of each individual macrocube was determined manually with the aid of a MATLAB script that transforms the perspective (see appendix E.3). Subsequently the known distribution of the magnetic field energy in the cuvette was used to calculate the cumulative energy of the array. The calculated energy is given with respect to the value of the magnetic energies of a square configuration, see insets in figure 8.4. At time  $< 600$  seconds, a rapid decrease of the energy difference between the actual and the square array is observed. From this result we surmise that energy minimization is indeed achieved when operating the piezo-actuator. This means that there is a good balance between the vibrational energy in the system and the energy forcing the macrocubes together. Consequently, we confirm that this setup is very suitable for this self-assembly process. After 600 seconds, the energy difference levels off at a value of around  $U = 3\text{ nJ}$ . Since the energy difference remains constant at a value which is non-zero, it is apparent that the lowest possible energy is not obtained. The optimal configuration has lower energy. A possible explanation is that the introduced vibrations are still too energetic. In this respect, it is tempting to compare the energy levels with the energy pumped into the system by the piezo. From the upper limit of 15 mJ provided by the power source, a fraction is taken up by the array of particles. If we assume this fraction is the volume of the particles to the entire volume of the system (about  $15 \times 10^3$ ), the energy a single particle can absorb is about  $1\text{ }\mu\text{J}$ . Since this value is a factor of thousand larger than the observed energy levels, this approach is probably too naive. Other attempts to estimate the disturbing energy in the system from macroscopic inputs, such as the velocity of the piezo, lead to much too high values as well.

### 8.3.3 Three-dimensional self-assembly

Self-assembly in three-dimensions was demonstrated by means of two examples: (I) templated, see figure 8.6.a and (II) levitating, see figure 8.6.b. As a template, again the bottom of the cuvette was used as in the 2D situation, but magnet 1 was not lowered as much. In the levitated case, the macrocubes were made less hydrophilic, to enhance the interaction.

In both cases, the target structure is a large 3D perfect primitive cubic crystal built from individual macrocubes. In both cases we find that many of the macrocubes are nicely aligned with each other and that the structure obtained closely matches the target structure. The result for the templated case appears to be much better than the levitated case, as expected. This result is understandable from the intuitive argument that in the templated case, pre-organization along one of the plane directions in the crystal is provided.

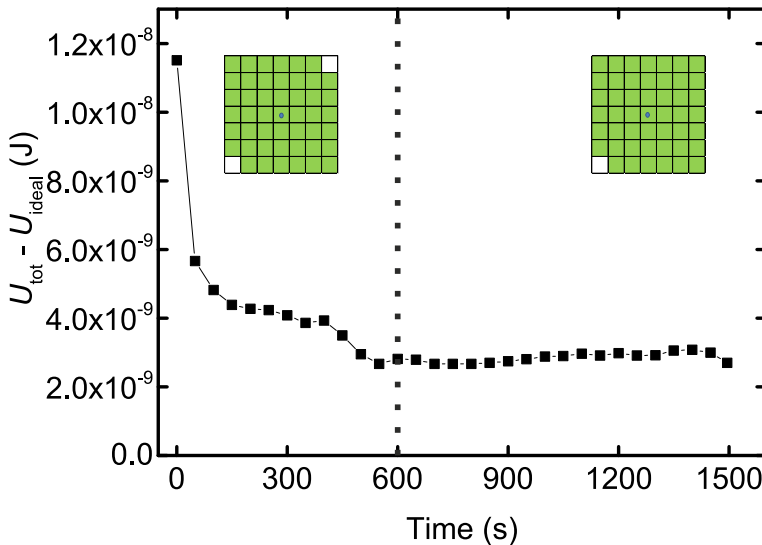


FIGURE 8.4 – *Difference between calculated energy of observed 2D arrays and of target configuration versus time. The energy difference decreases with time, indicative of energy minimization. After 600 seconds, the energy difference remains at around  $U = 3 \text{ nJ}$ . The insets show the square target configurations for the number of cubes in the field of view. There are some missing cubes at the corners of the structures, since the number of macrocubes was insufficient for full squares. At 600 seconds an additional cube entered, which is reflected in the target structure.*

To quantify these results, we used photographs <sup>§</sup> of the resulting 3D structures, similar to those in figure 8.6, to determine the percentage of observable good contacts between particles as a ratio with the total number of observable contacts. The six faces of each macrocube that could be observed were assessed. Contacts with an overlap of more than 95 % were rated as good. All other contacts are rejected, but counted. Furthermore, in the case of rotational misalignment, the contact is also rejected as bad. Faces that cannot be seen are not counted. For both types of 3D self-assembly, the relative number of good bonds was determined and compared in figure 8.5.

For the templated case, we find around 75 % good contacts, compared to around 25 % for the levitated experiment. This result confirms the qualitative observation that the templated results are better than the levitated self-assembly. In the levitated case, when the macrocubes are made less hydrophilic the number of faces that had no observable rotational misalignment appeared

<sup>§</sup>In addition, a video of the self-assembly process can be found online in the accompanying material (SA\_3D\_Templated) of reference [Woldering et al., 2015].

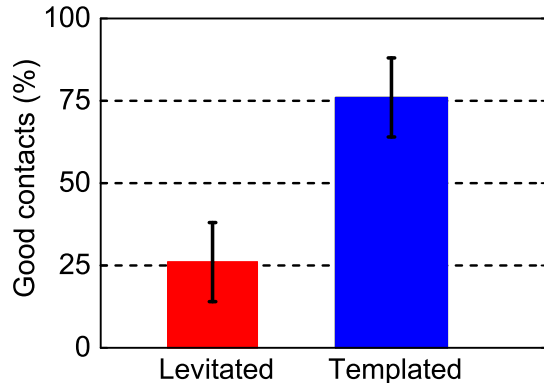


FIGURE 8.5 – Number of good contacts in arrays resulting from levitated (red) self- and templated (blue) self-assembly of surface treated macrocubes. The vertical bars depict the standard deviation of the measurements. The levitated and templated experiments were repeated 12 and 3 times, respectively.

to increase. The surface treatment however seems to have no significant effect on the number of good contacts. The effect of a change in hydrophilicity requires more research before definite conclusions can be drawn.

In the photograph in figure 8.6.b we find deviations from the perfect primitive cubic crystal structure. There appear to be planes of cubes aligned vertically ( $yz$ -planes), that are rotated with respect to each other (around the  $x$ -axis). We speculate that this is related to the anisotropy in the disturbing energy, caused by the fact that the piezo introduces sound waves along the long axis of the cuvette.

One can observe an elongation of the entire assembly in the  $xy$ -plane. This effect is due to the shape of the force field, which is slightly ellipsoidal, with the short axis along the  $z$  direction. This shape can be adjusted by modifying the distance between the magnets.

From these results it is apparent that this method has high potential for 3D self-assembly. We surmise that by tuning the hydrophilicity of the particles and the making the vibrational energy in the system less directional may result in an even closer match with the target structure.

## 8.4 Conclusions

We have demonstrated two- and three-dimensional self-assembly of anisotropic silicon cubes with edges of  $525\text{ }\mu\text{m}$ , treated with HDMS to make them less hydrophilic. To provide a driving force for self-assembly and avoid sedimentation, the cubes were levitated in a paramagnetic  $\text{GdCl}_3$  solution. The levitation height is controllable up to approximately 4 mm by changing the distance between the two permanent magnets that generate the magnetic field.

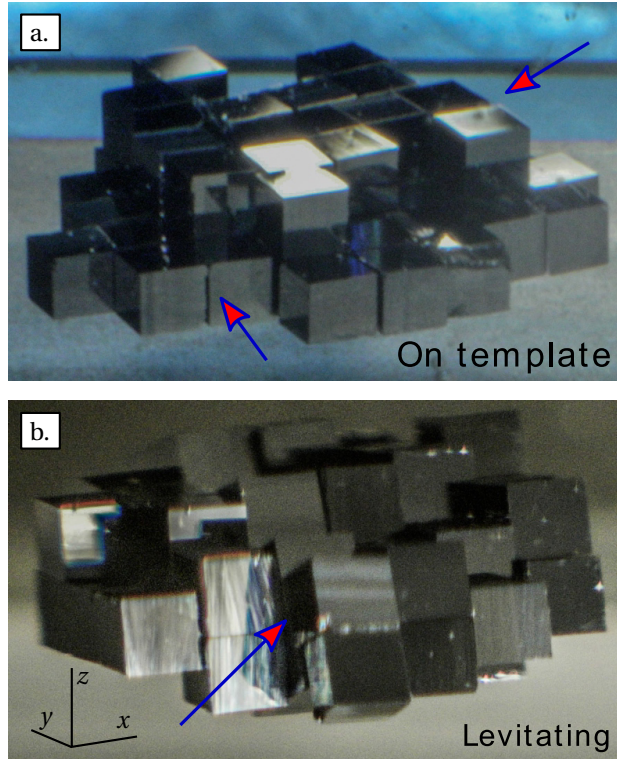


**FIGURE 8.6 – (a)** Photograph of the resulting array after 3D self-assembly in a paramagnetic liquid of hydrophilic silicon cubes on a template. The template is formed by the bottom of the cuvette. The macrocubes are successfully organized in a structure that closely resembles the target 3D cubic crystal, see for example the positions at the arrows. **(b)** Photograph of the resulting array after 3D self-assembly of levitating surface treated silicon cubes. The structure is a good match to the target cubic crystal, however small structural mismatches are identifiable, see for example the arrow. In particular, rotational and positional alignment errors are visible in between separate crystal planes.

A piezo element in our setup provides energy that drives the energy of the system towards a global minimum. For two-dimensional self-assembly, this was demonstrated by calculating the magnetic energy as a function of time.

The use of a non-structured surface as template is beneficial for successful self-assembly. For the 3D experiment, the fraction of cube faces that are fully aligned increases from 25 % to 75 % after inserting a template. The resulting structure is a good match with the target cubic crystal structure.

Further optimization is expected to be possible by tuning the hydrophilicity of the macrocubes and of the vibrational energy in the system. This method

is a promising route towards magnetically driven 3D self-assembly for applications such as 3D photonic bandgap crystals [Woldering et al., 2011] or memory crystals [Abelmann et al., 2010].

## **8.5 Acknowledgment**

We would like to thank Miko Elwenspoek and Jan Eijkel for inspiring discussions and Remco Sanders and Garud Snoep for helpful assistance. This work was financially supported by a VENI fellowship (Technical Sciences) by the Netherlands Organisation for Scientific Research (NWO) to Léon A. Woldering

# **Chapter 9**

## **Conclusions and recommendations**

In this thesis, I investigated magnetostatic interactions in arrays and their role in future electronics. In data storage, a role is projected for magnetostatic interactions in the reading and writing of 2D arrays of islands, in bit patterned media recording. I have investigated these interactions experimentally by imaging patterned arrays with a magnetic force microscope, assisted by modeling and simulations. Another role may be found in 3D fabrication of electronics by means of self-assembly. Magnetostatic interactions were studied that act as driving and/or binding force in the self-assembly of 2D and 3D arrays, by means of experiments and calculations based on large scale prototypes.

### **9.1 Patterned 2D arrays of islands**

#### **Side-coated tips corrigibly read and partially write arrays**

Side-coated MFM tips were used to test both the reading and writing of patterned arrays. The read back pulses of such tips are well modeled concerning their shape by a simple model. Moreover, magnetostatic distortions inflicted by the vertical tip motion, as well as distortion of non-magnetic origin, can be corrected computationally using the geometry of the imaged array. Besides this, a proper choice of the coating thickness of the tip (*e.g.* 35 nm and 80 nm) allows us to respectively image the sample without distortion, and to manipulate the magnetization of the islands. However the coating thickness is limited by the stability of the magnetization of the tip. In effect, the stray field of side-coated tips has been found to be smaller than the width of switching field distributions typical for arrays with sub-100 nm islands.

#### **Recommendation: explore fully-coated tips**

Since resolution is not an issue for imaging  $\geq 70$  nm islands, I would recommend to explore fully coated tips for the combined task of imaging and manipulating such arrays. Those tips potentially have higher magnetic moments,

and allow us to eliminate electrostatic interactions electrically (by applying a tip-sample voltage), as these interactions involve only single tip and sample layers of the same materials.

### **Fluctuating island shapes cause media noise**

The tip interacts with the sample via the combined field of the islands. However, it is worthwhile to investigate the islands individually and minutely. Even in arrays perfectly patterned concerning the positions of the islands, the shape of the perimeter of the islands fluctuates. This is unavoidable in lithographic patterning. A model that captures shape fluctuations by the dominant components of the noise spectrum of the perimeters, showed that this causes variation in the center of mass and area of the islands. These variations directly result in position and amplitude jitter in the read back sensors that interact on a coarse scale with the field. According to the model the jitters are correlated, which becomes important when extrapolated to the high areal densities required for BPM recording.

### **Simple 2D ISI reducing codes handle more media noise**

In high density BPM recording, media noise inhibits the correct detection of the stored bits, in addition to inter symbol interference. Taking advantage of the 2D phase-synchronized nature of the array, a simple coding scheme proved effective (*e.g.* permitting 8.5 % more position jitter), by avoiding the occurrence of the worst case 2D interfering patterns (at the cost of a 5/6-code rate). To reduce the bit error rate further, the 2D constraint codes could be incorporated in more sophisticated error correction coding, combined with more complex (*e.g.* maximum likelihood based) detection schemes. Ideally, such detection schemes handle ISI in a 2D fashion, and take all knowledge of media jitters into account, including their possible correlations.

### **Switching mechanisms vary from island to island**

Besides island to island fluctuations in shape, an investigation of their individual interactions with a globally applied field revealed that ~ 100 nm-sized islands in an identically patterned array can exhibit a broad distribution in their switching mechanism. Moreover, for the investigated array the switching mechanism turned out to be correlated to the switching field: Weak, easily switching islands showed a domain wall propagation dominated reversal, becoming more coherent rotation-like for stronger, harder to switch, islands. This stresses the need to investigate the switching of the elements of the array on an individual basis, as their individual characteristics are overlooked in distributions measured as a whole.

### The extend of local fields matter in island reversal

The effect of local fields on islands has been quantified by the 'equivalent uniform field'. These fields were determined by comparing the switching fields of islands in the local, non-uniform stray field of the tip to their switching field distribution (SFD) taken in global, uniform fields. At a large tip sample distance, the local tip field is in effect equivalent to a uniform field, yet too weak for any easy recording experiment. At smaller tip-sample distances, it remains difficult to interpret the effect of the tip in terms of its actual stray field. Analysis showed this effect depends on the switching mechanism of the island, which varies within the distribution of islands *and* may vary within the switching process. The simple tip model shows that in-contact the first 100 nm of the apex contributes significantly to the field. Therefore, to assess the effect of local fields fully by means of simulations, the shape and magnetization of the apex must be modeled in more detail, as well as the reversal modes of the islands.

### Further research: relate switching fields and full read back signals of islands to their shapes

For further research on 2D patterned arrays, it is interesting to investigate whether there is a relation between the islands geometry (*e.g.* perimeter) and switching field (and thus switching mechanism). This could give insight in the origin of the switching field distribution. Additionally, it is interesting to see in experiment whether the shapes and read back signals of islands are in agreement, since this is commonly assumed in media noise modeling. This might however be difficult, because the tested islands show only 6 % fluctuation in area, whereas a properly corrected signal still has 5 % to 9 % error (between images respectively imaging modes). If this error cannot be reduced, it seems necessary to compare the full shapes of the read back pulses (*i.e.* not only their amplitudes) to a simulated signal. This more detailed approach requires a more complex tip model than the simple geometric model, which oversimplifies the magnetization of the tip. Alternatively, deconvolution of a tip transfer function might work without requiring an accurate model.

## 9.2 Self-assembled 2D and 3D arrays of particles

In the near future, 2D arrays will likely find an application in data storage as bit patterned media. Investigations of magnetostatic interactions will be continually required, as the main challenges of BPM technology are handling the 2D-ISI in read back and narrowing down the distributions in write operations. Yet inevitably, 2D storage will be overtaken by 3D structures, which likely not rely on magnetism for data retention. Still, the fabrication of 3D arrays offer a new role for magnetostatic interactions by means of self-assembly. Dialetically, the pioneering experiments described in this thesis suggest that full magnetostatic 3D self-assembly (*e.g.* by dipolar interactions) calls for 2D arrays of magnetic

islands as templates, and demands detailed knowledge of the interactions between and among the individual islands and self-assembling elements.

### **Templates and binding forces improve the quality of self-assembled arrays**

For 3D micro-fabrication, I studied magnetostatic interactions that drive 2D and 3D self assemblies of diamagnetic particles via globally applied fields. Experiments with prototypical millimeter-sized particles showed that the orientational preference (as essentially imposed by the anisotropic (*i.e.* cubic) shape of the particles) could be improved by templating and adding a binding interparticle interaction. These measures offer a promising route to form the desired well ordered 3D array of a supercube. In 2D, calculations confirmed that the particles indeed minimize their energy, however, their configuration does not attain a minimum energy. A likely cause is too energetic excitation and the lack of a strong binding force.

### **Magnetic dipolar particles need anisotropic shapes to 3D self-assemble**

The role of magnetostatic interactions in binding individual particles was investigated theoretically by calculating trajectories in energy landscapes. Isotropically shaped particles (*i.e.* spheres) that interact via their magnetic dipole moments, prefer to assemble in 2D configurations. This is in correspondence with the behavior of ‘neodymium’ toy-magnets. Introduction of anisotropy, by indenting the particles, leads theoretically to a stable 3D configuration of four particles. Although the proposed scheme involves complex particles with freely rotating dipole moments, clearly an anisotropic shape is crucial to built larger 3D self-assemblies based on dipolar magnetostatic interactions.

### **Recommendation: increase hydrophobic binding and magnetostatic confinement, but avoid dipoles**

Concerning the self-assembly of 3D arrays, I would recommend to investigate self-assembly with hydrophobic particles, as the experiments with cubes with reduced hydrophilicity showed an improved quality of the self-assembled arrays. Magnetically, it is interesting to explore a stronger (tunable) field gradients to confine the particles more strongly. This may require a complicated setup of magnets. To use magnetostatic forces as a binding force, a higher order magnetic moment could possibly soften the constraints concerning the shape of the particles.

## **Appendices**



## Appendix A

# Detection of island perimeters

### A.1 Edge model and fitting procedure

Image processing is used to determine the perimeters of islands in a scanning electron microscopy (SEM) image. Figure A.1.a shows a single island in the image. In chapter 2, figure 2.1.a shows a larger section of the SEM image.

The problem is to detect the perimeter in 3D data ( $x, y, \text{SEM intensity} = f$ ) or, in cylindrical coordinates,  $(r, \theta, f)$ . Going from the center of an island radially outward, the SEM image shows near the edges of the island a gradual transition from high to low (zero) intensity. We model this edge by an arctangent transition with amplitude  $b$ , transition center  $R$  and width parameter  $a$ ,

$$f_n(r) = b_n \left( \frac{1}{2} - \frac{1}{\pi} \arctan \left( \frac{R_n - r}{a} \right) \right). \quad (\text{A.1})$$

Here  $f_n(r)$  is a function of radial position,  $r$ . We allow  $R_n$ ,  $b_n$  to vary width polar angle  $\theta_n$  and use  $a = 1 \text{ pixel} = 6.25 \text{ nm}$ . A number ( $1 \leq n \leq 20$ ) of such edges (determined by  $\theta_n$  distributed equally within  $[0, 2\pi]$ ) describes the island shape, and  $R_n$  gives us a discrete description of the perimeter  $R(\theta)$ .

The  $b_n$  and  $R_n$  were fitted to the shape of each island. In this process, simulated SEM intensity images are obtained using interpolation in the Fourier domain. A minimization routine in MATLAB was used to minimize the mean square error between the SEM and simulated image. Figure A.1.b shows the result of fitting for the island in A.1.a.

### A.2 improving the centers of the islands

By applying an averaging filter and peak detection, we obtained a first estimate of the centers of the islands, which was used in the detection of the perimeters. We verified the fitting of the detected perimeter is not sensitive to a small variation in the center of the island. However, the Fourier components of the perimeter ( $c_n$ ) are sensitive to what is taken as the center of the islands. Clearly,

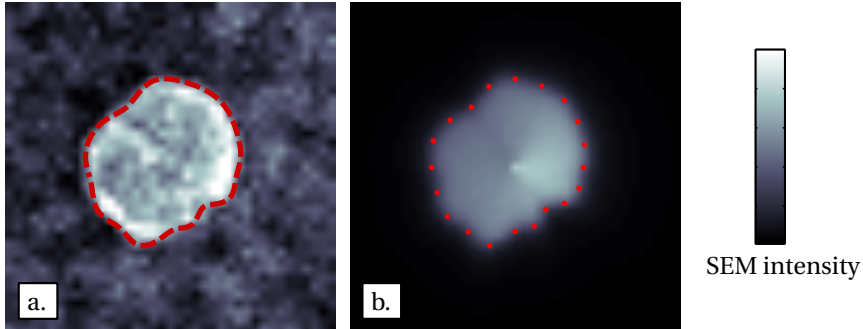


FIGURE A.1 – (a) SEM image of an island with diameter  $\approx 110$  nm and (b) simulated SEM intensity resulting from fitting the perimeter  $R(\theta_n)$  (20 red dots) and SEM intensity amplitude  $b_n$  to the image in (a). By interpolating  $R(\theta_n)$  to higher resolution, the perimeter of the island (dashed line in (a),  $R(\theta)$ ) is obtained.

for a perfectly circular perimeter (with only  $c_0 = R$  component), a  $c_1$  component, as well as other components, will be detected if a center is used that is not at the true center of the circle.

To improve the estimate of the island centers, the rough island centers were updated in an iterative procedure. In each iteration, a new center coordinate is calculated for each island, according to the centers of nearest neighboring islands (*i.e.* the mean of the  $x$  and  $y$  coordinates of the centers of the neighbors). Centers of islands without neighbors (neighbors that fall outside the SEM image), or with badly shaped neighboring islands, were not updated. The procedure has settled after 8 iterations. By improving the island centers, the detected perimeters have a smaller mean  $c_n$  ( $< 0.01c_0$ ) and smaller variance  $S_n$  (*e.g.*  $S_1$  reduces by a factor 2), for  $n > 0$ . In other words, after improving the centers, the detected perimeters are on average more circular and have smaller fluctuations.

## Appendix B

# Method for 2D coding simulations

In chapter 3 an MFM based channel is used to test a 2D coding scheme. In this appendix, the simulation method is described. The channel is based on the MFM channel used in [Groenland and Abelmann, 2007], and the simulation method is similar. The MFM read back pulse mimics a HDD based read back of media with a soft underlayer (SUL) [Nutter et al., 2005]; the pulse has the typical overshoot *i.e.* negative going signal at the side tails of the pulse.

The read back signal consist of the linear superposition of positive and negative read back pulses. The signal is sampled at the (ideal) bit positions *i.e.* the center of islands according to their ideal position in the 2D lattice. The signal fluctuates because of the varying 2D inter symbol interference (2D-ISI), and due to variations in the position of the islands (*i.e.* bit/island position jitter). The position variations are modeled by a random 2D translation sampled from a uniform distribution (jitter factor =  $J/\Lambda$  with  $\Lambda$  the bit period), with a limited range so island overlap is avoided.

The read back pulse is based on the response of a bar shaped tip [Abelmann, 2010] and a cylindrical island. The pulse is proportional to  $F'$ , in the Fourier domain given by

$$\Phi_0(\mathbf{k}) = -\frac{1}{2}\mu_0 M_{s,\text{tip}} t w \frac{1}{|\mathbf{k}|} \text{sinc}\left(\frac{tk_x}{2}\right) \text{sinc}\left(\frac{wk_y}{2}\right) (1 - \exp(-L|\mathbf{k}|)) \quad (\text{B.1})$$

$$\sigma_{\text{eff}}(\mathbf{k}) = M_s (1 - \exp(-|\mathbf{k}| t_s)) \frac{\pi D J_1(|\mathbf{k}| D/2)}{|\mathbf{k}|} \quad (\text{B.2})$$

$$F'(\mathbf{k}) = -|\mathbf{k}|^2 \sigma_{\text{eff}}(\mathbf{k}) \Phi_0(\mathbf{k}) \exp(-z|\mathbf{k}|). \quad (\text{B.3})$$

$$(\text{B.4})$$

Here  $\mathbf{k} = (k_x, k_y)$  denotes spatial frequencies in the  $x$ - $y$  plane;  $\Phi_0$  is the potential of the tip in the plane of the apex (similar to an ‘ABS’ potential in a hard disk drive channel [Nutter et al., 2004]); tip dimensions are  $(t \times w \times L)$  in  $(x, y, z)$ ;  $M_{s,\text{tip}}$  is the saturation magnetization of the tip, and  $\mu_0$  the vacuum permeability;  $\text{sinc}(x) = \sin(x)/x$ . The effective charge density  $\sigma_{\text{eff}}$  accounts for the surface

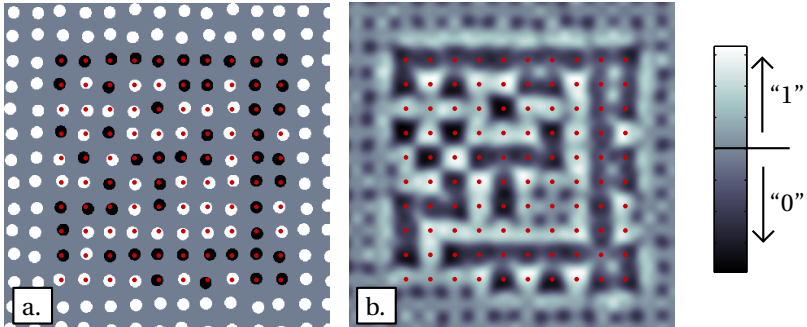


FIGURE B.1 – Coding simulation example of a  $10 \times 10$  data pattern (red dots) in an ‘all one’ background. The islands (a) have 10 % position jitter. Colors indicate the bit values i.e. “1” (white) and “0” (black). (b) MFM signal according to the channel used in chapter 3. The red dots indicate the ideal lattice position at which the signal is detected (“1” or “0” for respectively white or black contrast). Frames of  $127 \times 127$  data patterns were used in the actual simulation, in which the islands in the background have random bit values.

charge on bottom and top faces of the cylindrical island with thickness  $t_s$ , diameter  $D$ , and saturation magnetization  $M_s$ . The  $J_1$  is a Bessel function of the first kind. The tip-sample distance (between the top of the island and the tip apex) is  $z$ .

The signal on the  $x$ -axis is used to create a circular symmetric pulse in order to have equal ISI in both dimensions. This signal is tabulated. The table is used to look up the signal value at the lattice position of an island and its neighbors, taking into account the position shift of the island. The sign of the pulse depends on the bit value the island holds.

In the simulations, random data is coded and mapped on to a 2D island array. A 2D read back signal is obtained by summing the signal of all the islands. A threshold detector converts the signal to a binary signal, based on the sign of the signal (*i.e.* threshold level is 0).

As an example, figure B.1 shows a small simulated data pattern (without coding). In chapter 3, larger frames of  $127 \times 127$  islands have been simulated. Over 15 million bits were simulated to obtain a bit error rate (BER) for a given code and jitter factor.

## Appendix C

# MFM sensitivity modeling and estimation

Here we estimate the sensitivity of the phase shift between cantilever deflection and excitation caused by a (magnetic) force derivative acting on the tip. For this, we use the frequency response of the cantilever as measured by the DI 3100 MFM and Nanoscope extender and software.

Theoretically [Abelmann, 2010; Sader, 1998], the cantilever behaves in the limit of small dissipation ( $Q \gg 1$ ) as a simple harmonic oscillator. Driven near resonance, the sensitivity  $s = Q/c$ . The quality of resonance  $Q = \partial\phi/\partial\omega|_{\omega=\omega_0} \cdot \omega_0/2$ , is thus given by the slope of the phase response at resonance and the resonance frequency of the cantilever ( $\omega_0 \approx \omega_{\text{resonance}}$ ). We use Sader's method [Sader et al., 1999] to determine the spring constant  $c$  from the frequency response of the cantilever. The expression for the spring constant (*i.e.* equation (4) in [Sader et al., 1999]) is proportional to  $Q$ . We obtain

$$s = \gamma_z \gamma_{\text{eff}} \frac{1}{0.1906 \rho w^2 l \Gamma_i(\omega) \omega^2}, \quad (\text{C.1})$$

with  $l$  the length and  $w$  the width of the cantilever,  $\rho$  the density of the fluid and  $\Gamma_i$  the imaginary part of the hydrodynamic function. We will use the nominal/specified values for the geometrical parameters, and those given in [Sader et al., 1999] for fluid parameters (air). We introduce the factor  $\gamma_z$  to take into account the reduction in  $Q$  when the tip approaches the sample [Green and Sader, 2005]. The  $\gamma_{\text{eff}}$  accounts for the distortion in the measured DI phase signal; it converses the true phase shift signal to the DI phase signal. We will use the DI phase signal to present measured and simulated signals.

The relation between DI phase signal and true phase shift can be modeled [Abelmann, 2010; Bocek, 2001] by

$$\phi = \arcsin \frac{V_\phi(\omega) - V_{\phi,0}}{V_0} = \arctan \frac{\omega \omega_0}{Q(\omega_0^2 - \omega^2)}. \quad (\text{C.2})$$

Here, the ‘voltages’  $V_\phi(\omega)$ ,  $V_{\phi,0}$  and  $V_0$  are respectively the DI phase signal at frequency  $\omega$ , its offset and scale factor;  $\omega_0$  denotes the natural resonance frequency of the cantilever. Fitting  $V_{\phi,0}$ ,  $V_0$ ,  $\omega_0$  and  $Q$  to the measured phase response  $V_\phi(\omega)$  results in the true phase response,  $\phi$ .

We measured frequency responses of several cantilevers and determined  $Q = 468(27)$  and  $\gamma_{\text{eff}} = 1.12(10)$ , where the uncertainty is the standard deviation over the different cantilevers. For an approached tip (at 40–100 nm nominal scan height) we determined  $\gamma_z = 0.85(1)$ , where the uncertainty is over this single tip. Based on this,  $s = 17(3) \text{ rad/Nm}^{-1}$ , were we estimate a 10%–20% variation over the cantilevers. Using  $Q$ , we calculate  $c = 27(2) \text{ N m}^{-1}$ . This value is much smaller than the nominal  $42 \text{ N m}^{-1}$ , however it agrees with calibrations of similar cantilevers [Kim et al., 2010].

To check the fitting results, we compared  $Q$  to the width of the frequency response of the cantilever oscillation amplitude. The fitted  $Q$  matches better than a  $Q_V$  derived directly from  $V_\phi(\omega)$ . The quality factor given by the DI software (which has a different value, and is based on the amplitude response) was found to predict the width of the amplitude response reasonably. In respect to this quality factor, the fitted  $Q$  is on average 11 % smaller, while the uncorrected  $Q_V$  is 28 % higher.

Besides this, we have verified that frequency shift signals can indeed be converted to phase shift signals via the slope  $\partial V_\phi / \partial \omega|_{\omega=\omega_{\text{drive}}}$ , by comparing MFM scan lines (over the same islands in a patterned array) taken in frequency shift and phase shift operation modes. The scale factor obtained from the slope matches with a fitted factor (that minimizes the mean squared error between scan lines) within the 4 % wide confidence interval of the fit (using a 95 % confidence level).

## Appendix D

# Magnetostatic energy of two cylinders

To obtain the exact magnetostatic energy of two cylinders, we take the multipole moments of the cylinders and sum the energy of each multipole pair

$$U = \sum_{N_1=0}^{N_m} \sum_{N_2=0}^{N_m} U_{N_1, N_2}. \quad (\text{D.1})$$

Here  $N_m$  is the multipole order;  $N_m = 0$  corresponds to the monopole moment,  $N_m = 1$  to the dipole moments. For  $N_m$  sufficiently large, the sum converges to the exact energy. The energy of multipole pair  $N_1 - N_2$  is

$$U_{N_1, N_2} = \sum_{\mathbf{n}_1} \sum_{\mathbf{n}_2} \frac{q_{\mathbf{n}_1} q_{\mathbf{n}_2}}{\mathbf{n}_1! \mathbf{n}_2!} \frac{\partial^{N_1 + N_2}}{\partial \mathbf{r}^{\mathbf{n}_1} \partial \mathbf{r}^{\mathbf{n}_2}} \frac{1}{\mathbf{r}} \quad (\text{D.2})$$

In the sums,  $\mathbf{n}_i = (n_x, n_y, n_z)_i$  runs over all combinations of  $n_x + n_y + n_z = N_i$ , where the  $n$ 's are integers  $\geq 0$ . The  $\partial \mathbf{r}^{\mathbf{n}} = \partial x^{n_x} \partial y^{n_y} \partial z^{n_z}$  with  $\mathbf{r}$  the center to center separation between cylinders, and  $\mathbf{n}! = n_x! n_y! n_z!$ .

The multipole moments,  $q_{\mathbf{n}}$  are

$$q_{\mathbf{n}} = \int_{V_m} x^{n_x} y^{n_y} z^{n_z} (-\nabla \cdot \mathbf{m}) d\mathbf{r}^3, \quad (\text{D.3})$$

where the integral is over the volume of the magnet. The  $q_{\mathbf{n}}$  depend on the orientation of the cylinders. For a cylinder tilted by a rotation of  $\alpha$  over the y-axis (as in figure 7.4)

$$\begin{aligned} q_{\mathbf{n}} = & \int_0^{D/2} \int_0^{2\pi} r (r \sin \varphi)^{n_y} \cdot [(r \cos \varphi \cos \alpha - \frac{t}{2} \sin \alpha)^{n_x} \cdot (r \cos \varphi \sin \alpha + \frac{t}{2} \cos \alpha)^{n_z} \\ & (r \cos \varphi \cos \alpha + \frac{t}{2} \sin \alpha)^{n_x} \cdot (r \cos \varphi \sin \alpha - \frac{t}{2} \cos \alpha)^{n_z}] d\varphi dr. \end{aligned} \quad (\text{D.4})$$

Here we used that the ‘magnetic charge density’ is distributed on the top and bottom disks of the cylinder, *i.e.*  $-\nabla \cdot \mathbf{m} = \pm M_s \delta(z \mp t/2)$ . The integral can be written as a sum of  $\cos^k \alpha \cdot \sin^l \alpha \cdot (t/2)^m \cdot (D/2)^p$  terms, which we evaluated numerically in MATLAB [[Mathworks, 2010](#)].

For the dimensions of our magnets and particles (in table 7.1), the error of the dipole approximation is only 1 % for  $|\mathbf{r}| = 2r$ . However, if we would equip the particle with a flat magnet, *e.g.*  $D/2 = 4\text{ mm}$  and  $t = 2\text{ mm}$ , the error is 11 %. The accuracies improve by about a factor 10 for each next  $N_m$ , when we evaluate (D.1) upto  $N_m = 8$ .

## Appendix E

# Diamagnetic levitation

### E.1 Diamagnetic levitation

Diamagnetic materials are repelled from magnetic fields [Feynman et al., 1964], which makes diamagnetic materials perfect for magnetic levitation. The degree to which a material is diamagnetic is measured in the magnetic susceptibility  $\chi$ . For diamagnetic materials this is a negative number, for paramagnetic materials—materials attracted to magnetic fields—this is a positive number. Strongly diamagnetic materials, like pyrolytic graphite, are easy to levitate [Pelline, 2004] in contrast to weakly diamagnetic materials. The challenge to levitate a weakly diamagnetic material, like silicon, can be overcome with a paramagnetic medium [Haynes, 2013a]. By surrounding the weakly diamagnetic material with a strongly paramagnetic medium, levitation can be achieved [Winkleman et al., 2007]. The paramagnetic medium is attracted to the magnets, pushing the diamagnetic material away: Magnetic levitation is achieved. The forces involved with diamagnetic levitation in a paramagnetic medium are twofold: On the one hand, there is a buoyant force, depending on the gravity, densities of the two materials, and volume of the diamagnetic particle. On the other hand, there is a magnetic force, which is dependent of the magnetic susceptibilities of the two materials, volume of the diamagnetic particle, and the applied magnetic field. Since both forces are a function of particle volume, the force density can be determined [Winkleman et al., 2007]. Assuming that the susceptibility is small, so that the liquid is not saturated, and that the particles is small, so that the force density is more or less constant,

$$\mathbf{F}/V_p = -(\rho_l - \rho_p)\mathbf{g} - \frac{(\chi_l - \chi_p)}{\mu_0} (\mathbf{B} \cdot \nabla) \mathbf{B}. \quad (E.1)$$

Here  $\mathbf{F}$  is the force on the particle,  $V_p$  is its volume;  $\rho_l$  and  $\rho_p$  are the densities, and  $\chi_l$  and  $\chi_p$  the magnetic susceptibilities of the liquid and particle, respectively. Vector  $\mathbf{g}$  is the gravitational acceleration,  $\mu_0$  the vacuum permeability and  $\mathbf{B}$  the magnetic field. The density of silicon is  $\rho_p = 2329 \text{ kg/m}^3$  [Haynes,

2013b], the density of a 2 mol/L GdCl<sub>3</sub> solution in water was measured to be  $\rho_l = 1459 \text{ kg/m}^3$ . The magnetic susceptibility can be calculated for the GdCl<sub>3</sub> solution in water, see equation E.2 [Haynes, 2013a],

$$\chi_l = 27.930 \cdot 10^{-3} \cdot 4\pi \cdot C, \quad (\text{E.2})$$

where  $C$  is the concentration of GdCl<sub>3</sub> in water, in this work 2 mol/L. At these concentrations, the magnetic susceptibility of silicon is negligible ( $\chi_p = -3.215 \cdot 10^{-6}$  [Haynes, 2013a]).

In order to obtain a stable levitation point, two magnets can be placed close to each other with similar poles facing [Mirica et al., 2008]. To calculate the forces on a particle, the magnetic field needs to be determined. For the calculation of the magnetic field of a single magnet, the Biot-Savart equation was used, see equation E.3 [Feynman et al., 1964]

$$\mathbf{B}(\mathbf{r}_1) = \frac{\mu_0}{4\pi} \int \frac{\mathbf{j}(\mathbf{r}_2) \times \mathbf{r}_{12}}{|\mathbf{r}_{12}|^3} d\mathbf{r}_2. \quad (\text{E.3})$$

Here  $\mathbf{B}$  is the magnetic,  $\mu_0$  is the permeability of free space,  $\mathbf{r}_{12} = \mathbf{r}_1 - \mathbf{r}_2$  is the full displacement vector;  $\mathbf{j} = \nabla \times \mathbf{m}$  is the current density in of the magnet, which has magnetization  $\mathbf{m}$ . For a uniformly, axially magnetized (*i.e.* along  $z$ ) cylindrical magnet,  $\mathbf{j}$  is located on its side surface, directed horizontally and tangentially to this surface. The magnitude of this surface current density is  $|\mathbf{m}|$ . The magnetization of the magnets used in this work was calculated from a magnetic field measurement at the edge of the magnets, and is  $1.25/\mu_0 \text{ A m}^{-1}$ .

To obtain a two magnet model, the field of the second magnet is shifted by  $z = l + h$  and superimposed on the field of the first magnet, where  $h$  is the separation between the magnets and  $l$  the length of the magnet stack.

To avoid elliptical integrals [Ravaud et al., 2010], implementation of equation (E.3) includes a discrete summation of the integral over the azimuthal angle. All analytical calculations were performed using MATLAB<sup>\*</sup>. The analytical model was verified with finite element method (FEM) simulations using COMSOL<sup>†</sup>. The FEM model takes the finite size of the liquid container in account (the susceptibility contrast between liquid and air); the model agrees with the analytical calculations within 0.3 % in the region between the magnets. The analytical calculations of the magnetic field were used to model the levitation height as in equation E.1, see figure 8.2.

## E.2 Energy of assembly

To calculate the magnetostatic forces on the particles and the energy of their ensemble, we derive an approximate solution of the quasi-static, no-current, Maxwell equations. The liquid and the particles are modeled as linear permeable regions. Their permeabilities are respectively  $\mu_l = \mu_0 \cdot (1 + \chi_l)$  and  $\mu_p =$

<sup>\*</sup>MATLAB R2013a, MathWorks, Natick, US.

<sup>†</sup>COMSOL 4.3, COMSOL BV, Zoetermeer, The Netherlands.

$\mu_0 \cdot (1 + \chi_p)$ , where the  $\chi$ 's are magnetic susceptibilities and  $\mu_0$  the vacuum permeability. The applied magnetic field is due to exterior sources. We define  $-\nabla\phi = \mathbf{H}$ ,  $\mathbf{B} = \mu(\mathbf{H} + \mathbf{m})$ , so  $\nabla \cdot \mathbf{H} = -\nabla \cdot \mathbf{m}$ . It is convenient to take  $\mu = \mu_l$ . Then the induced magnetization  $\mathbf{m} = 0$  in the liquid and  $\mathbf{m} = (\chi_p - \chi_l) \frac{\mu_0}{\mu_l} \mathbf{H}$  in the particle.

Our main approximation concerns the boundary conditions imposed on  $\phi$  at the interface between regions with different permeability. These conditions are: (I)  $\phi$  is continuous over the interface and (II)  $\mu_l \frac{\partial\phi}{\partial\mathbf{n}}|_l = \mu_p \frac{\partial\phi}{\partial\mathbf{n}}|_p$ , where  $\mathbf{n}$  is the, say, outer surface normal. For small susceptibilities ( $\chi \ll 1$ ), we can violate condition (II) a bit and take  $\mu_p \frac{\partial\phi}{\partial\mathbf{n}}|_p \approx \mu_l \frac{\partial\phi}{\partial\mathbf{n}}|_p$ , so  $\frac{\partial\phi}{\partial\mathbf{n}}$  is continuous. Then  $\mathbf{H}$  is determined solely by the free-space field of the exterior sources. Consequently, there is no inter-particle interaction. Next to this, we will use  $\mu_l \approx \mu_0$ .

With these approximations, the energy of a particle in the susceptible liquid background is then given by

$$U = -\frac{1}{2} \int \mathbf{m} \cdot \mathbf{B} dV \quad (\text{E.4})$$

$$= -\frac{1}{2\mu_0} \int_{V_p} (\chi_p - \chi_l) |\mathbf{B}|^2 dV, \quad (\text{E.5})$$

where  $V_p$  is the volume of the particle, and the field  $\mathbf{B} = \mu_0 \mathbf{H}$  is given by the free-space/vacuum field of the sources (*i.e.* the static magnets). Upon differentiation with respect to the particle position we obtain the force on the particle

$$\mathbf{F} = -\nabla U \quad (\text{E.6})$$

$$= \frac{1}{2\mu_0} \int_{V_p} (\chi_p - \chi_l) (\nabla |\mathbf{B}|^2) dV, \quad (\text{E.7})$$

or,

$$\mathbf{F} = \frac{1}{\mu_0} \int_{V_p} (\chi_p - \chi_l) (\mathbf{B} \cdot \nabla) \mathbf{B} dV, \quad (\text{E.8})$$

where we used  $\nabla \times \mathbf{B} = 0$  (which holds, as  $\mathbf{B}$  is given by a free-space field). For small gradients of  $\mathbf{B}$  over the particle volume, the force is well represented by the force density

$$\mathbf{F}/V = \frac{1}{\mu_0} (\chi_p - \chi_l) (\mathbf{B} \cdot \nabla) \mathbf{B}. \quad (\text{E.9})$$

This is a familiar expression [Winkleman et al., 2007] (and (E.1)), applicable in case of small particles and small susceptibilities.

Equation (E.5) has been used to calculate the energy of a system of particles. Numerically,  $|\mathbf{B}|^2$  was calculated/tabulated once (as function of radial distance and  $z$ ) at high resolution. We used this table together with linear interpolation to integrate over the particle volume by means of Riemann summation, taking the position and orientation (*i.e.* rotation) of the particle into account. The energy of the ensemble is the sum of the energy of the individual particles.

### E.3 Perspective transformation

To calculate the energy of the particles in the 2D self-assembly process, we determined their position and orientation in photographs (*e.g.* figure 8.3). For this purpose it is convenient to have a top-view of the particles. We applied a perspective transform to attain this view.

For the perspective transformation we consider a matrix,  $A$ , that maps 2D world coordinates  $(x, y)$  to image/pixel coordinates  $(i, j)$  [Hartley and Zisserman, 2004]. A general linear transformation is given by

$$\begin{bmatrix} x \\ y \\ 1 \end{bmatrix} = A \cdot \begin{bmatrix} i \\ j \\ 1 \end{bmatrix}, \quad (\text{E.10})$$

with

$$A = \begin{bmatrix} a_{xi} & a_{xj} & a_{x1} \\ a_{yi} & a_{yj} & a_{y1} \\ a_{1i} & a_{1j} & a_{11} \end{bmatrix}. \quad (\text{E.11})$$

Such transformation matrices are routinely inverted in camera calibration methods that employ a calibration grid (*e.g.* checkerboard pattern) with known world coordinates [Hartley and Zisserman, 2004]. Here, we do not have such a fixed grid. However, we know the dimensions of the cubical particles. For instance, the vertices of the top face of a cube are related by

$$\begin{aligned} \mathbf{p}_2 - \mathbf{p}_1 &= \mathbf{u} \\ \mathbf{p}_3 - \mathbf{p}_4 &= \mathbf{u} \\ \mathbf{p}_3 - \mathbf{p}_2 &= \mathbf{v} \\ \mathbf{p}_4 - \mathbf{p}_1 &= \mathbf{v}, \end{aligned} \quad (\text{E.12})$$

where  $\mathbf{p}_{1..4}$  are the vertices oriented in a counterclockwise fashion. Since the top face of a particle is square in real world coordinates, the edges are orthogonal and related via

$$\begin{aligned} \mathbf{u} &= \begin{bmatrix} u_x \\ u_y \end{bmatrix} \\ \mathbf{v} &= \begin{bmatrix} -u_y \\ u_x \end{bmatrix}. \end{aligned} \quad (\text{E.13})$$

Substituting (E.10) and (E.13) in (E.12) results a set of equations in terms of (I) the elements of matrix  $A$  (*i.e.* the  $a$ 's), (II) the  $M$  pairs of diagonal coordinates ( $u_{x,m}$  and  $u_{y,m}$ ) and (III) the  $M \times 4$  pairs of vertex coordinates in the image ( $i_{1..4,m}$  and  $j_{1..4,m}$ ). Unknown are (I) and (II), known are (III). Additionally, we defined the origin in the photograph as the central pixel (resulting in  $a_{x1} = a_{y1} = 0$ ) and we define the  $x$ -axis by

$$a_{xi}\Delta i_0 + a_{xj}\Delta j_0 - 1 = 0 \quad (\text{E.14})$$

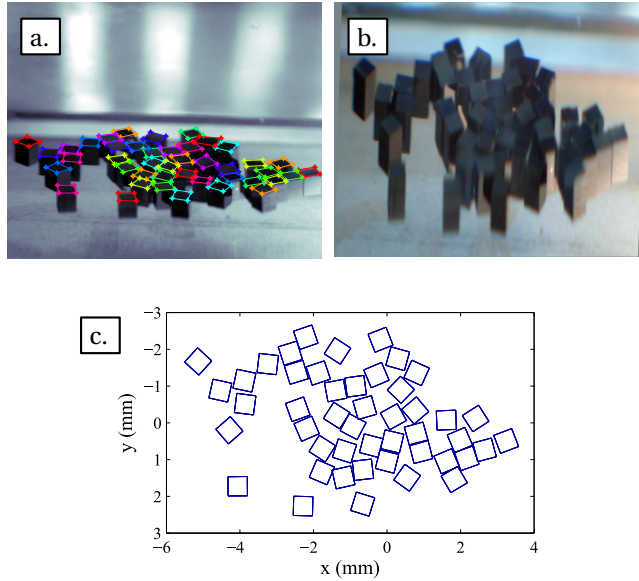


**FIGURE E.1 – Example of the perspective transformation.** (a) A raw photograph with manually detected vertices of the top faces of the particles; (b) The image after perspective transformation and color enhancement; the top faces have been transformed into squares. (c) Positions and orientations of the particles, which were manually detected in the transformed image.

where  $(\Delta i_0, \Delta j_0)$  is the vector in the image that corresponds to the unit  $x$ -axis. The matrix elements of  $A$  are solved by minimizing the mean squared error in (E.12) and (E.14). For this, the vertex coordinates were determined manually (*i.e.* by eye) in a photograph. For the actual transformation we used the `imtransform` function of the MATLAB image processing toolbox. This transformation was applied to entire photographs, however, only the pixels that correspond to positions in the plane of the top faces of the cubes are correctly transformed. Figure E.1 shows an example of the perspective transformation.

# Bibliography

- Abelmann L, February 2010  
“Magnetic force microscopy”  
In: *Encyclopedia of Spectroscopy and Spectrometry*, volume 2, pp. 1415–1425, Elsevier, Amsterdam
- Abelmann L, Tas N, Berenschot E, Elwenspoek M, 2010  
“Self-assembled three-dimensional non-volatile memories”  
*Micromachines* **1**, pp. 1–18, doi: [10.3390/mi1010001](https://doi.org/10.3390/mi1010001)
- Abramowitz A, Stegun I A, 1972  
*Handbook of mathematical functions with formulas, graphs, and mathematical tables* (tenth printing),  
Dover Publications (New York)  
— Bessel functions of the first kind: p. 358
- Adam J P, Rohart S, Jamet J P, Ferré J, Mougin A, Weil R, Bernas H, Faini G, 2012  
“Magnetization reversal by confined droplet growth in soft/hard hybrid nanodisks with perpendicular anisotropy”  
*Phys. Rev. B* **85**, pp. 214417–1–7, doi: [10.1103/PhysRevB.85.214417](https://doi.org/10.1103/PhysRevB.85.214417)
- Alekseev A, Popkov A, Shubin A, Pudonin F, Djuzhev N, 2014  
“Effect of horizontal magnetization reversal of the tips on magnetic force microscopy images”  
*Ultramicroscopy* **136**, pp. 1–5, doi: [10.1016/j.ultramic.2013.08.007](https://doi.org/10.1016/j.ultramic.2013.08.007)
- Alink L, Groenland J P J, de Vries J, Abelmann L, 2012  
“Determination of bit patterned media noise based on island perimeter fluctuations”  
*IEEE Trans. Magn.* **48**, pp. 4574–4577, doi: [10.1109/TMAG.2012.2201138](https://doi.org/10.1109/TMAG.2012.2201138)
- Allen F G, Gobeli G W, July 1962  
“Work function, photoelectric threshold, and surface states of atomically clean silicon”  
*Physical Review* **127**, pp. 150–158, doi: [10.1103/PhysRev.127.150](https://doi.org/10.1103/PhysRev.127.150)
- Allwood D A, Xiong G, Faulkner C C, Atkinson D, Petit D, Cowburn R P, 2005  
“Magnetic domain-wall logic”  
*Science* **309**, pp. 1688–1692, doi: [10.1126/science.1108813](https://doi.org/10.1126/science.1108813)
- Amos N, Butler J, Lee B, Shachar M H, Hu B, Tian Y, Hong J, Garcia D, Ikkawi R M, Haddon R C, Litvinov D, Khizroev S, 2012  
“Multilevel-3D bit patterned magnetic media with 8 signal levels per nanocolumn”  
*PLoS ONE* **7**, doi: [10.1371/journal.pone.0040134](https://doi.org/10.1371/journal.pone.0040134)
- Argento C, French R H, 1996  
“Parametric tip model and force-distance relation for Hamaker constant determination from atomic force microscopy”  
*Journal of Applied Physics* **80**, pp. 6081–6090, doi: <http://dx.doi.org/10.1063/1.363680>

- Arnett P, Minvielle T, Nair S, 1999  
“Extracting media noise characteristics from MFM images”  
*J. Magn. Magn. Mater.* **193**, pp. 479–483
- ASTC, ASTC technology roadmap - <http://idema.org/?cat=10> -accessed March 2016
- Awomolo A, Jiang L, Zhang J, Jursich G, Takoudis C, 2007  
“Dielectric materials in organic thin film transistors”  
*Journal of Undergraduate Research* **1**, pp. 47–51
- Aziz M M, Wright C D, Middleton B K, Du H, Nutter P, 2002  
“Signal and noise characteristics of patterned media”  
*IEEE Trans. Magn.* **38**, pp. 1964–1966, doi: [10.1109/TMAG.2002.802787](https://doi.org/10.1109/TMAG.2002.802787)
- Babcock K, Elings V, Dugas M, Loper S, 1994  
“Optimization of thin-film tips for magnetic force microscopy”  
*IEEE Transactions on Magnetics* **30**, pp. 4503–4505, doi: [10.1109/20.334130](https://doi.org/10.1109/20.334130)
- Bai J, Takahashi H H band Ito, Rheem Y W, Saito H, Ishio S, 2004  
“Influence of inhomogeneous coercivities on media noise in granular perpendicular media investigated by using magnetic force microscopy”  
*J. Magn. Magn. Mater.* **283**, pp. 291–296, doi: [10.1016/j.jmmm.2004.06.003](https://doi.org/10.1016/j.jmmm.2004.06.003)
- Belle B D, Schedin F, Pilet N, Ashworth T V, Hill E W, Nutter P W, Hug H J, Miles J J, 2007  
“High resolution magnetic force microscopy study of e-beam lithography patterned Co/Pt nanodots”  
*J. Appl. Phys.* **101**, p. 09F517, doi: [10.1063/1.2713429](https://doi.org/10.1063/1.2713429)
- Belov P A, Slobozhanyuk A P, Filinov D S, Yagupov I V, Kapitanova P V, Simovski C R, Lapine M, Kivshar Y A, 2013  
“Broadband isotropic  $\mu$ -near-zero metamaterials”  
*Appl. Phys. Lett.* **103**, pp. 211903–1–211903–4
- Berger A, Lengsfeld B, Ikeda Y, 2006  
“Determination of intrinsic switching field distributions in perpendicular recording media (invited)”  
*Journal of Applied Physics* **99**, 08E705, doi: <http://dx.doi.org/10.1063/1.2164416>
- Bocek D, June 2001  
“About “Bocek” degrees used in the extender package on digital instruments nanoscope scanning probe microscopes”  
*Microscopy Today* **9**
- Boncheva M, Andreev S A, Mahadevan L, Winkleman A, Reichman D R, Prentiss M G, Whitesides S, Whitesides G M, 2005  
“Magnetic self-assembly of three-dimensional surfaces from planar sheets”  
*Proceedings of the National Academy of Sciences* **102**, pp. 3924–3929, doi: [10.1073/pnas.0500807102](https://doi.org/10.1073/pnas.0500807102)
- Brown W, 1963  
*Micromagnetics*  
Interscience tracts on physics and astronomy, Interscience Publishers
- Burkhardt H, May 1989  
“Optimal data retrieval for high density storage”  
In: *CompEuro '89., 'VLSI and Computer Peripherals. VLSI and Microelectronic Applications in Intelligent Peripherals and their Interconnection Networks', Proceedings.*, pp. 1/43–1/48, doi: [10.1109/CMPEUR.1989.93341](https://doi.org/10.1109/CMPEUR.1989.93341)

- Cambel V, Gregušová D, Eliáš P, Fedor J, Kostič I, Maňka J, Ballo P, 2011  
 "Switching magnetization magnetic force microscopy - an alternative to conventional lift-mode MFM"  
*Journal of Electrical Engineering* **62**, pp. 37–43
- Cambel V, Precner M, Fedor J, Šoltýs J, Tóbik J, Ščepka T, Karapetrov G, 2013  
 "High resolution switching magnetization magnetic force microscopy"  
*Appl. Phys. Lett.* **102**, doi: [10.1063/1.4791591](https://doi.org/10.1063/1.4791591)
- Chan K S, Rachid E M, Eason K, Radhakrishnan R, Teo K K, 2012  
 "Comparison of one- and two-dimensional detectors on simulated and spin-stand readback waveforms"  
*Journal of Magnetism and Magnetic Materials* **324**, pp. 336 – 343, doi: [10.1016/j.jmmm.2010.12.022](https://doi.org/10.1016/j.jmmm.2010.12.022)  
 Selected papers of the 9th Perpendicular Magnetic Recording Conference(PMRC 2010)
- Chang J, Mironov V L, Gribkov B A, Fraerman A A, Gusev S A, Vdovichev S N, 2006  
 "Magnetic state control of ferromagnetic nanodots by magnetic force microscopy probe"  
*Journal of Applied Physics* **100**, doi: [10.1063/1.2384811](https://doi.org/10.1063/1.2384811)
- Chaplygin Y A, Shevyakov V I, 2013  
 "Investigation into the effect of cantilever structural parameters on the sensitivity of magnetic force microscopy"  
*Nanotechnologies in Russia* **8**, pp. 186–190, doi: [10.1134/S1995078013020031](https://doi.org/10.1134/S1995078013020031)
- Che X, Lederman M, Gibson G A, Bertram H N, Schultz S, 1993  
 "Noise analysis and image focusing for magnetic force microscopy"  
*J. Appl. Phys.* **73**, pp. 5805–5807, doi: [10.1063/1.353583](https://doi.org/10.1063/1.353583)
- Cheng H, Greengard L, Rokhlin V, 1999  
 "A fast adaptive multipole algorithm in three dimensions"  
*Journal of Computational Physics* **155**, pp. 468 – 498, doi: [10.1006/jcph.1999.6355](https://doi.org/10.1006/jcph.1999.6355)
- Chiolerio A, Allia P, 2012  
 "Towards a quantitative analysis of magnetic force microscopy data matrices"  
*Journal of Magnetism and Magnetic Materials* **324**, pp. 2416–2428, doi: [10.1016/j.jmmm.2012.01.035](https://doi.org/10.1016/j.jmmm.2012.01.035)
- Chiolerio A, Celasco E, Celegato F, Guastella S, Martino P, Allia P, Tiberto P, Pirri F, 2008  
 "Enhanced imaging of magnetic structures in micropatterned arrays of Co dots and antidots"  
*Journal of Magnetism and Magnetic Materials* **320**, pp. e669–e673, doi: [10.1016/j.jmmm.2008.04.149](https://doi.org/10.1016/j.jmmm.2008.04.149)
- Chiolerio A, Martino P, Celegato F, Giurdanella S, Allia P, 2010  
 "Enhancement and correlation of MFM images: Effect of the tip on the magnetic configuration of patterned Co thin films"  
*IEEE Transactions on Magnetics* **46**, pp. 195–198, doi: [10.1109/TMAG.2009.2033202](https://doi.org/10.1109/TMAG.2009.2033202)
- Choi S J, Kim K H, Cho Y J, Lee H s, Cho S h, Kwon S J, Moon J h, Lee K J, 2010  
 "Demonstration of ultra-high-resolution MFM images using Co<sub>90</sub>Fe<sub>10</sub>-coated CNT probes"  
*Journal of Magnetism and Magnetic Materials* **322**, pp. 332–336, doi: [10.1016/j.jmmm.2009.09.052](https://doi.org/10.1016/j.jmmm.2009.09.052)
- Clark T, Tien J, Duffy D C, Paul K E, Whitesides G M, 2001  
 "Self-assembly of 10-µm-sized objects into ordered three-dimensional arrays"  
*J. Am. Chem. Soc.* **123**, pp. 7677–7682

- Coffey K R, Thomson T, Thiele J U, 2002  
“Angular dependence of the switching field of thin-film longitudinal and perpendicular magnetic recording media”  
*Journal of Applied Physics* **92**, pp. 4553–4559, doi: [10.1063/1.1508430](https://doi.org/10.1063/1.1508430)
- Cohen G, Halpern E, Nanayakkara S U, Luther J M, Held C, Bennewitz R, Boag A, Rosenwaks Y, 2013  
“Reconstruction of surface potential from kelvin probe force microscopy images”  
*Nanotechnology* **24**, doi: [10.1088/0957-4484/24/29/295702](https://doi.org/10.1088/0957-4484/24/29/295702)
- Constantoudis V, Kokkoris G, Xydi P, Gogolides E, Pargon E, Martin M, 2009  
“Line-edge-roughness transfer during plasma etching: modeling approaches and comparison with experimental results”  
*Journal of Micro/Nanolithography, MEMS, and MOEMS* **8**, pp. 043004–043004–8, doi: [10.1117/1.3268365](https://doi.org/10.1117/1.3268365)
- de Vries J, October 2013  
*Energy barriers in patterned media*  
Ph.D. thesis, Univ. of Twente, Enschede
- Delalande M, de Vries J, Abelmann L, Lodder J C, 2012  
“Measurement of the nucleation and domain depinning field in a single Co/Pt multilayer dot by Anomalous Hall effect”  
*J. Magn. Magn. Mater.* **324**, pp. 1277–1280, doi: [10.1016/j.jmmm.2011.09.037](https://doi.org/10.1016/j.jmmm.2011.09.037)
- Demirörs A F, Pillai P P, Kowalczyk B, Grzybowski B A, 2013  
“Colloidal assembly directed by virtual magnetic moulds”  
*Nature* **503**, pp. 99–103
- Dittrich R, Hu G, Schrefl T, Thomson T, Suess D, Terris B D, Fidler J, 2005  
“Angular dependence of the switching field in patterned magnetic elements”  
*Journal of Applied Physics* **97**, doi: [10.1063/1.1851931](https://doi.org/10.1063/1.1851931)
- Dürig U, 1999  
“Relations between interaction force and frequency shift in large-amplitude dynamic force microscopy”  
*Applied Physics Letters* **75**, pp. 433–435
- Elwenspoek M, Abelmann L, Berenschot E, van Honschoten J, Jansen H, Tas N, 2010  
“Self-assembly of (sub-)micron particles into supermaterials”  
*J. Micromech. Microeng.* **20**, p. 064001, doi: [10.1088/0960-1317/20/6/064001](https://doi.org/10.1088/0960-1317/20/6/064001)
- Engelen J B C, Delalande M, le Fèbre A J, Bolhuis T, Shimatsu T, Kikuchi N, Abelmann L, Lodder J C, 2010  
“Thermally induced switching field distribution of a single CoPt dot in a large array”  
*Nanotechnol.* **21**, p. 035703, doi: [10.1088/0957-4484/21/3/035703](https://doi.org/10.1088/0957-4484/21/3/035703)
- Feynman R P, Leighton R B, Sands M, 1964  
*The Feynman Lectures on Physics, Vol II*,  
Addison Wesley
- Fontana R E, R H S, Decad G, May 2012  
“Technology roadmap comparisons for TAPE, HDD, and NAND Flash: Implications for data storage applications”  
*IEEE Transactions on Magnetics* **48**, pp. 1692–1696, doi: [10.1109/TMAG.2011.2171675](https://doi.org/10.1109/TMAG.2011.2171675)
- Futamoto M, Hagami T, Ishihara S, Soneta K, Ohtake M, 2013  
“Improvement of magnetic force microscope resolution and application to high-density recording media”  
*IEEE Transactions on Magnetics* **49**, pp. 2748–2754, doi: [10.1109/TMAG.2013.2251868](https://doi.org/10.1109/TMAG.2013.2251868)

- Giessibl F J, 1997  
 "Forces and frequency shifts in atomic-resolution dynamic-force microscopy"  
*Physical Review B: Condensed Matter and Materials Physics* **56**, pp. 16010–16015
- Gil A, Colchero J, Gómez-Herrero J, Baró A M, 2003  
 "Electrostatic force gradient signal: Resolution enhancement in electrostatic force microscopy and improved Kelvin probe microscopy"  
*Nanotechnology* **14**, pp. 332–340, doi: [10.1088/0957-4484/14/2/345](https://doi.org/10.1088/0957-4484/14/2/345)
- Giles R, Cleveland J P, Manne S, Hansma P K, Drake B, Maivald P, Boles C, Gurley J, Elings V, 1993  
 "Noncontact force microscopy in liquids"  
*Appl. Phys. Lett.* **63**, pp. 617–618, doi: [10.1063/1.109967](https://doi.org/10.1063/1.109967)
- Glijer P, Noel Abarra E, Kisner H, Suzuki T, 1996  
 "MFM studies of recording phenomena in high density longitudinal recordings"  
*IEEE Transactions on Magnetics* **32**, pp. 3557–3562, doi: [10.1109/20.538689](https://doi.org/10.1109/20.538689)
- Göddenhenrich T, Lemke H, Mück M, Hartmann U, Heiden C, 1990  
 "Probe calibration in magnetic force microscopy"  
*Applied Physics Letters* **57**, pp. 2612–2614, doi: [10.1063/1.103827](https://doi.org/10.1063/1.103827)
- Goldowsky J, Mastrangeli M, Jacot-Descombes L, Gullo M, Mermoud G, Brugger J, Martinoli A, Nelson B, Knapp H, 2013  
 "Acousto-fluidic system assisting in-liquid self-assembly of microcomponents"  
*Journal of Micromechanics and Microengineering* **23**, p. 125026, doi: [10.1088/0960-1317/23/12/125026](https://doi.org/10.1088/0960-1317/23/12/125026)
- Goll D, Bublat T, 2013  
 "Large-area hard magnetic L1<sub>0</sub>-FePt and composite L1<sub>0</sub>-FePt based nanopatterns"  
*physica status solidi (a)* **210**, pp. 1261–1271, doi: [10.1002/pssa.201329017](https://doi.org/10.1002/pssa.201329017)
- Gómez-Moñivas S, Sáenz JJ, Carminati R, Greffet JJ, 2000  
 "Theory of electrostatic probe microscopy: a simple perturbative approach"  
*Applied Physics Letters* **76**, pp. 2955–2957
- Gracias D H, Tien J, Breen T L, Hsu C, Whitesides G M, 2000  
 "Forming electrical networks in three dimensions by self-assembly"  
*Science* **289**, pp. 1170–1172
- Green C P, Sader J E, 2005  
 "Frequency response of cantilever beams immersed in viscous fluids near a solid surface with applications to the atomic force microscope"  
*Journal of Applied Physics* **98**, doi: [10.1063/1.2136418](https://doi.org/10.1063/1.2136418)
- Griffiths D J, 1999  
*Introduction to electrodynamics*,  
 Prentice Hall, 3rd edition
- Groenland J P J, Abelmann L, Jun. 2007  
 "Two-dimensional coding for probe recording on magnetic patterned media"  
*IEEE Trans. Magn.* **43**, pp. 2307–2309, doi: [10.1109/TMAG.2007.893137](https://doi.org/10.1109/TMAG.2007.893137)
- Haast M, Schuurhuis J, Abelmann L, Lodder J, Popma T, 1998  
 "Reversal mechanism of submicron patterned coni/pt multilayers"  
*IEEE Transactions on Magnetics* **34**, pp. 1006–1008, doi: [10.1109/20.706339](https://doi.org/10.1109/20.706339)
- Hartley R I, Zisserman A, 2004  
*Multiple View Geometry in Computer Vision*,  
 Cambridge University Press, ISBN: 0521540518, second edition

- Hasegawa T, Pei W, Wang T, Fu Y, Washiya T, Saito H, Ishio S, 2008  
“MFM analysis of the magnetization process in  $\text{Li}_0\text{-Al}$  FePt patterned film fabricated by ion irradiation”  
*Acta Materialia* **56**, pp. 1564–1569, doi: [10.1016/j.actamat.2007.12.008](https://doi.org/10.1016/j.actamat.2007.12.008)
- Hassel C, Stienen S, Römer F M, Meckenstock R, Dumpich G, Lindner J, 2009  
“Resistance of domain walls created by means of a magnetic force microscope in transversally magnetized epitaxial Fe wires”  
*Applied Physics Letters* **95**, doi: [10.1063/1.3187219](https://doi.org/10.1063/1.3187219)
- Haykin S S, 1989  
*An introduction to analog and digital communications*,  
Wiley  
ISBN 9780471859789
- Haynes W M, 2013a  
“Magnetic susceptibility of the elements and inorganic compounds”  
In: *CRC handbook of chemistry and physics, 94th Edition*, volume 94, pp. 4.131–4.136, CRC Press
- Haynes W M, 2013b  
“Physical constants of inorganic compounds list of abbreviations”  
In: *CRC handbook of chemistry and physics, 94th Edition*, pp. 4.43–4.101, CRC Press
- Van der Heijden F, 1994  
*Image based measurement system: object recognition and parameter estimation*,  
John Wiley & Sons Ltd  
Section 6.2 on p. 151 discusses parameter estimation.
- Hellwig O, Berger A, Thomson T, Dobisz E, Bandic Z Z, Yang H, Kercher D S, Fullerton E E, 2007  
“Separating dipolar broadening from the intrinsic switching field distribution in perpendicular patterned media”  
*Applied Physics Letters* **90**, doi: [10.1063/1.2730744](https://doi.org/10.1063/1.2730744)
- Hennek J, Nemiroski A, Subramaniam A, Bwambok D, Yang D, Harburg D, Tricard S, Ellerbee A, Whitesides G, 2015  
“Using magnetic levitation for non-destructive quality control of plastic parts”  
*Advanced Materials* **27**, pp. 1587–1592, doi: [10.1002/adma.201405207](https://doi.org/10.1002/adma.201405207)
- Hertl W, Hair M L, 1971  
“Reaction of hexamethyldisilazane with silica”  
*J. Phys. Chem.* **75**, pp. 2181–2185
- Heydon G P, Farley A N, Hoon S R, Valera M S, Tomlinson S L, 1997  
“Resonant torque magnetometry: A new in-situ technique for determining the magnetic properties of thin film MFM tips”  
*IEEE Transactions on Magnetics* **33**, pp. 4059–4061, doi: [10.1109/20.619662](https://doi.org/10.1109/20.619662)
- Hoffmann B, Houbertz R, Hartmann U, 1998  
“Eddy current microscopy”  
*Applied Physics A: Materials Science & Processing* **66**, pp. S409–S413, doi: [10.1007/s003390051173](https://doi.org/10.1007/s003390051173)
- Hu G, Thomson T, Rettner C T, Raoux S, Terris B D, 2005a  
“Magnetization reversal in CoPd nanostructures and films”  
*Journal of Applied Physics* **97**, doi: [10.1063/1.1849572](https://doi.org/10.1063/1.1849572)

- Hu G, Thomson T, Rettner C T, Terris B D, 2005*b*  
 "Rotation and wall propagation in multidomain co/pd islands"  
*IEEE Trans. Magn.* **41**, pp. 3589–3591, doi: [10.1109/TMAG.2005.854733](https://doi.org/10.1109/TMAG.2005.854733)
- Hubert A, Schäfer R, 1998  
*Magnetic domains: the analysis of magnetic microstructures*,  
 Springer-Verlag, Berlin, Heidelberg, New-York
- Hug J, Stiefel B, Van Schendel P J A, Moser A, Hofer R, Martin S, Güntherodt H J, Porthun S, Abelmann L, Lodder C J, Bochi G, O'Handley R C, 1998  
 "Quantitative magnetic force microscopy on perpendicularly magnetized samples"  
*Journal of Applied Physics* **83**, pp. 5609–5620
- Ikezoe Y, Hirota N, Nakagawa J, Kitazawa K, 1998  
 "Making water levitate [7]"  
*Nature* **393**, pp. 749–750, doi: [10.1038/31619](https://doi.org/10.1038/31619)
- Ilievski F, Mani M, Whitesides G, Brenner M, 2011*a*  
 "Self-assembly of magnetically interacting cubes by a turbulent fluid flow"  
*Phys. Rev. E Stat. Nonlinear Soft Matter Phys.* **83**, pp. –, doi: [10.1103/PhysRevE.83.017301](https://doi.org/10.1103/PhysRevE.83.017301)
- Ilievski F, Mirica K A, Ellerbee A K, Whitesides G M, 2011*b*  
 "Templated self-assembly in three dimensions using magnetic levitation"  
*Soft Matter* **7**, pp. 9113–9118, doi: [10.1039/C1SM05962A](https://doi.org/10.1039/C1SM05962A)
- ITRS, 2013  
*International technology roadmap for semiconductors 2013 edition: Process integration, devices, and structures*  
 See [www.itrs2.net](http://www.itrs2.net)
- Jaafar M, Asenjo A, Vázquez M, 2008  
 "Calibration of coercive and stray fields of commercial magnetic force microscope probes"  
*IEEE Trans Nanotechnol* **7**, pp. 245–250, doi: [10.1109/TNANO.2008.917785](https://doi.org/10.1109/TNANO.2008.917785)
- Jaafar M, Gómez-Herrero J, Gil A, Ares P, Vázquez M, Asenjo A, 2009  
 "Variable-field magnetic force microscopy"  
*Ultramicroscopy* **109**, pp. 693–699, doi: [10.1016/j.ultramic.2009.01.007](https://doi.org/10.1016/j.ultramic.2009.01.007)
- Jaafar M, Iglesias-Freire O, Serrano-Ramón L, Ibarra M R, de Teresa J M, Asenjo A, 2011  
 "Distinguishing magnetic and electrostatic interactions by a kelvin probe force microscopy-magnetic force microscopy combination"  
*Beilstein J. Nanotechnol.* **2**, pp. 552–560, doi: [10.3762/bjnano.2.59](https://doi.org/10.3762/bjnano.2.59)
- Jiang Y, Guo W, 2009  
 "Temperature dependence of the stability of written bits in a magnetic hard-disk medium investigated by magnetic force microscopy"  
*Journal of Magnetism and Magnetic Materials* **321**, pp. 2963–2965, doi: [10.1016/j.jmmm.2009.04.063](https://doi.org/10.1016/j.jmmm.2009.04.063)
- Keskinoz M, 2008  
 "Two-dimensional equalization/detection for patterned media storage"  
*IEEE Trans. Magn.* **44**, pp. 533–539, doi: [10.1109/TMAG.2007.914966](https://doi.org/10.1109/TMAG.2007.914966)
- Kikuchi N, Kato T, Okamoto S, Kitakami O, Tezuka N, Sugimoto S, 2008  
 "Magnetization reversal process and bistability of Co/Pt multilayer dot"  
*Journal of Applied Physics* **103**, 07C510, doi: [10.1063/1.2838288](https://doi.org/10.1063/1.2838288)

- Kim M S, Choi J H, Kim J H, Park Y K, 2010  
“Accurate determination of spring constant of atomic force microscope cantilevers and comparison with other methods”  
*Measurement: Journal of the International Measurement Confederation* **43**, pp. 520–526, doi: [10.1016/j.measurement.2009.12.020](https://doi.org/10.1016/j.measurement.2009.12.020)
- Kirk K J, McVitie S, Chapman J N, Wilkinson C D W, 2001  
“Imaging magnetic domain structure in sub-500 nm thin film elements”  
*Journal of Applied Physics* **89**, pp. 7174–7176, doi: [10.1063/1.1355336](https://doi.org/10.1063/1.1355336)
- Kleiber M, Kümmelen F, Löhndorf M, Wadas A, Weiss D, Wiesendanger R, 1998  
“Magnetization switching of submicrometer Co dots induced by a magnetic force microscope tip”  
*Physical Review B - Condensed Matter and Materials Physics* **58**, pp. 5563–5567, doi: [10.1103/PhysRevB.58.5563](https://doi.org/10.1103/PhysRevB.58.5563)
- Kondorsky E, 1940  
“On hysteresis in ferromagnetics”  
*J. Phys (Moscow)* **2**, pp. 161–181
- Kong L, Zhuang L, Chou S Y, 1997  
“Writing and reading 7.5 Gb/in<sup>2</sup> longitudinal quantized magnetic disk using magnetic force microscope tips”  
*IEEE Transactions on Magnetics* **33**, pp. 3019–3021, doi: [10.1109/20.617830](https://doi.org/10.1109/20.617830)
- Krone P, Makarov D, Cattoni A, Faini G, Haghiri-Gosnet A M, Knittel I, Hartmann U, Schrefl T, Albrecht M, 2011  
“Investigation of the magnetization reversal of a magnetic dot array of Co/Pt multilayers”  
*Journal of Nanoparticle Research* **13**, pp. 5587–5593, doi: [10.1007/s11051-010-0123-z](https://doi.org/10.1007/s11051-010-0123-z)
- Kryder M H, Gage E C, McDaniel T W, Challener W A, Rottmayer R E, Ju G, Hsia Y T, Erden M F, 2008  
“Heat assisted magnetic recording”  
*Proc. IEEE* **96**, pp. 1810–1835, doi: [10.1109/JPROC.2008.2004315](https://doi.org/10.1109/JPROC.2008.2004315)
- Lau J, Liu X, Boling R, Shaw J, 2011  
“Decoupling nucleation and domain-wall propagation regimes in (co/pd) n multilayer nanostructures”  
*Physical Review B - Condensed Matter and Materials Physics* **84**, doi: [10.1103/PhysRevB.84.214427](https://doi.org/10.1103/PhysRevB.84.214427)
- Lau J W, Liu X, 2012  
“Angular dependence of switching field distribution in (Co/Pd)<sub>n</sub> multilayer nanostructure arrays”  
*Journal of Applied Physics* **112**, doi: [10.1063/1.4764338](https://doi.org/10.1063/1.4764338)
- Lau J W, Shaw J M, 2011  
“Magnetic nanostructures for advanced technologies: Fabrication, metrology and challenges”  
*Journal of Physics D: Applied Physics* **44**, doi: [10.1088/0022-3727/44/30/303001](https://doi.org/10.1088/0022-3727/44/30/303001)
- Lebedev V, Weld D M, 2014  
“Self-assembled Zeeman slower based on spherical permanent magnets”  
*J. Phys. B: At. Mol. Opt. Phys.* **47**, pp. 155003–1–155003–5
- Li W M, Chen Y J, Huang T L, Xue J M, Ding J, 2011  
“Calculation of individual bit island switching field distribution in perpendicular magnetic bit patterned media”  
*Journal of Applied Physics* **109**, doi: [10.1063/1.3563069](https://doi.org/10.1063/1.3563069)

- Li W M, Huang X L, Shi J Z, Chen Y J, Huang T L, Ding J, 2012  
 "Angular dependence and temperature effect on switching field distribution of Co/Pd based bit patterned media"  
*Journal of Applied Physics* **111**, doi: [10.1063/1.3678456](https://doi.org/10.1063/1.3678456)
- Li Z, Li X, Liu D, Saito H, Ishio S, 2014  
 "Near surface magnetic domain observation with ultra-high resolution"  
*Nanoscale* **6**, pp. 11163–11168, doi: [10.1039/c4nr02215g](https://doi.org/10.1039/c4nr02215g)
- Lide D R, editor, 1995  
*CRC handbook of chemistry and physics, 76th edition*,  
 CRC Press, Boca Raton, Florida, USA
- Lohau J, Kirsch S, Carl A, Dumpich G, Wassermann E F, 1999  
 "Quantitative determination of effective dipole and monopole moments of magnetic force microscopy tips"  
*Journal of Applied Physics* **86**, pp. 3410–3417
- Luo F, Heyderman L J, Solak H H, Thomson T, Best M E, 2008  
 "Nanoscale perpendicular magnetic island arrays fabricated by extreme ultraviolet interference lithography"  
*Applied Physics Letters* **92**, doi: [10.1063/1.2841821](https://doi.org/10.1063/1.2841821)
- Luttge R, 2009  
 "Massively parallel fabrication of repetitive nanostructures: Nanolithography for nanoarrays"  
*J. Phys. D: Appl. Phys.* **42**, p. 123001, doi: [10.1088/0022-3727/42/12/123001](https://doi.org/10.1088/0022-3727/42/12/123001)
- Luttge R, van Wolferen H A G M, Abelmann L, 2007  
 "Laser interferometric nanolithography using a new positive chemical amplified resist"  
*J. Vac. Sci. Technol. B* **25**, pp. 2476–2480, doi: [10.1116/1.2800328](https://doi.org/10.1116/1.2800328)
- Manalis S, Babcock K, Massie J, Elings V, Dugas M, 1995  
 "Submicron studies of recording media using thin-film magnetic scanning probes"  
*Appl. Phys. Lett.* **66**, pp. 2585–2587, doi: [10.1063/1.113509](https://doi.org/10.1063/1.113509)
- Mastrangeli M, Abbasi S, Varel C, van Hoof C, Celis J P, Böhringer K F, 2009  
 "Self-assembly from milli- to nanoscales: methods and applications"  
*Journal of Micromechanics and Microengineering* **19**, pp. 1–37, doi: [10.1088/0960-1317/19/8/083001](https://doi.org/10.1088/0960-1317/19/8/083001)
- Mastrangeli M, Martinoli A, Brugger J, 2014  
 "Three-dimensional polymeric microtiles for optically-tracked fluidic self-assembly"  
*Microelectronic Engineering* **124**, pp. 1–7, doi: [10.1016/j.mee.2014.04.017](https://doi.org/10.1016/j.mee.2014.04.017)
- Mathworks, 2010  
*MATLAB version 7.10 (R2010a)*  
 The Mathworks, Inc., Natick, Massachusetts
- McDaniel T W, 2012  
 "Areal density limitation in bit-patterned, heat-assisted magnetic recording using FePtX media"  
*Journal of Applied Physics* **112**, doi: [10.1063/1.4764336](https://doi.org/10.1063/1.4764336)
- McVitie S, Ferrier R P, Scott J, White G S, Gallagher A, 2001  
 "Quantitative field measurements from magnetic force microscope tips and comparison with point and extended charge models"  
*Journal of Applied Physics* **89**, pp. 3656–3661, doi: [10.1063/1.1352031](https://doi.org/10.1063/1.1352031)

- Mirica F KAand Ilievski, Ellerbee A, Shevkoplyas S, Whitesides G, 2011  
“Using magnetic levitation for three dimensional self-assembly”  
*Advanced Materials* **23**, pp. 4134–4140, doi: [10.1002/adma.201101917](https://doi.org/10.1002/adma.201101917)
- Mirica K, Phillips S, Shevkoplyas S, Whitesides G, 2008  
“Using magnetic levitation to distinguish atomic-level differences in chemical composition of polymers, and to monitor chemical reactions on solid supports”  
*Journal of the American Chemical Society* **130**, pp. 17678–17680, doi: [10.1021/ja8074727](https://doi.org/10.1021/ja8074727)
- Mironov V L, Ermolaeva O L, 2009  
“Optimization of a data storage system based on the array of ferromagnetic particles and magnetic force microscope”  
*J. Surf. Invest.* **3**, pp. 840–845, doi: [10.1134/S1027451009050292](https://doi.org/10.1134/S1027451009050292)
- Mironov V L, Gribkov B A, Vdovichev S N, Gusev S A, Fraerman A A, Ermolaeva O L, Shubin A B, Alexeev A M, Zhdan P A, Binns C, 2009  
“Magnetic force microscope tip-induced remagnetization of copt nanodisks with perpendicular anisotropy”  
*J. Appl. Phys.* **106**, p. 053911, doi: [10.1063/1.3202354](https://doi.org/10.1063/1.3202354)
- Mitsuzuka K, Kikuchi N, Shimatsu T, Kitakami O, Aoi H, Muraoka H, Lodder J C, 2007  
“Switching field and thermal stability of CoPt/Ru dot arrays with various thicknesses”  
*IEEE Trans. Magn.* **43**, pp. 2160–2162, doi: [10.1109/TMAG.2007.893129](https://doi.org/10.1109/TMAG.2007.893129)
- Moritz J, Landis S, Toussaint J C, Bayle-Guillemaud P, Rodmacq B, Casali G, Lebib A, Chen Y, Nozières J P, Diény B, 2002  
“Patterned media made from pre-etched wafers: A promising route toward ultrahigh-density magnetic recording”  
*IEEE Transactions on Magnetics* **38**, pp. 1731–1736, doi: [10.1109/TMAG.2002.1017764](https://doi.org/10.1109/TMAG.2002.1017764)
- Moser A, Weller D, Best M E, Doerner M F, 1999  
“Dynamic coercivity measurements in thin film recording media using a contact write/read tester”  
*Journal of Applied Physics* **85**, pp. 5018–5020, doi: [10.1063/1.370077](https://doi.org/10.1063/1.370077)
- Moser A, Takano K, Margulies D T, Albrecht M, Sonobe Y, Ikeda Y, Sun S, Fullerton E E, 2002  
“Magnetic recording: Advancing into the future”  
*J. Phys. D: Appl. Phys.* **35**, pp. R157–R167, doi: [10.1088/0022-3727/35/19/201](https://doi.org/10.1088/0022-3727/35/19/201)
- Murillo Vallejo R, Apr. 2006  
*Magnetic media patterned by laser interference lithography*  
Ph.D. thesis, University of Twente, Enschede, The Netherlands
- Nabavi S, Vijaya Kumar B V K, 2007  
“Two-dimensional generalized partial response equalizer for bit-patterned media”  
*IEEE International Conference on Communications* pp. 6249–6254, doi: [10.1109/ICC.2007.1035](https://doi.org/10.1109/ICC.2007.1035)
- Nabavi S, Kumar B V K V, Bain J A, 2008  
“Two-dimensional pulse response and media noise modeling for bit-patterned media”  
*IEEE Trans. Magn.* **44**, pp. 3789–3792, doi: [10.1109/TMAG.2008.2002387](https://doi.org/10.1109/TMAG.2008.2002387)
- Nabavi S, Kumar B V K V, Bain J A, Hogg C, Majetich S A, 2009  
“Application of image processing to characterize patterning noise in self-assembled nano-masks for bit-patterned media”  
*IEEE Trans. Magn.* **45**, pp. 3523–3526, doi: [10.1109/TMAG.2009.2022493](https://doi.org/10.1109/TMAG.2009.2022493)
- Nair S K, Richard M H, 1998  
“Patterned media recording: noise and channel equalization”  
*IEEE Trans. Magn.* **34**, pp. 1916–1918, doi: [10.1109/20.706742](https://doi.org/10.1109/20.706742)

- Ntokas I T, Nutter P W, Tjhai C J, Ahmed M Z, 2007  
 "Improved data recovery from patterned media with inherent jitter noise using low-density parity-check codes"  
*IEEE Trans. Magn.* **43**, pp. 3925–3929, doi: [10.1109/TMAG.2007.903349](https://doi.org/10.1109/TMAG.2007.903349)
- Nutter P, Shi Y, Belle B, Miles J, 2008  
 "Understanding sources of errors in bit-patterned media to improve read channel performance"  
*IEEE Transactions on Magnetics* **44**, pp. 3797–3800, doi: [10.1109/TMAG.2008.2002516](https://doi.org/10.1109/TMAG.2008.2002516)
- Nutter P W, McKirdy D r, Middleton B K, Wilton D T, Shute H A, 2004  
 "Effect of island geometry on the replay signal in patterned media storage"  
*IEEE Trans. Magn.* **40**, pp. 3551–3558, doi: [10.1109/TMAG.2004.835697](https://doi.org/10.1109/TMAG.2004.835697)
- Nutter P W, Ntokas I T, Middleton B K, 2005  
 "An investigation of the effects of media characteristics on read channel performance for patterned media storage"  
*IEEE Trans. Magn.* **41**, pp. 4327–4334, doi: [10.1109/TMAG.2005.856586](https://doi.org/10.1109/TMAG.2005.856586)
- Okamoto S, Kato T, Kikuchi N, Kitakami O, Tezuka N, Sugimoto S, 2008  
 "Energy barrier and reversal mechanism in (co/pt) multilayer nanodot"  
*J Appl Phys* **103**, doi: [10.1063/1.2831785](https://doi.org/10.1063/1.2831785)
- Panchumarthy R, Karunaratne D K, Sarkar S, Bhanja S, 2013  
 "Magnetic state estimator to characterize the magnetic states of nano-magnetic disks"  
*IEEE Transactions on Magnetics* **49**, pp. 3545–3548, doi: [10.1109/TMAG.2013.2240441](https://doi.org/10.1109/TMAG.2013.2240441)
- Park D, Kim K, Ryu B I, 2004  
 "3-dimensional nano-CMOS transistors to overcome scaling limits"  
*Proceedings of the 7th International Conference on Solid-State and Integrated Circuits Technology* pp. 35–40
- Parkin S S P, Roche K P, Samant M G, Rice P M, Beyers R B, Scheuerlein R E, O'Sullivan E J, Brown S L, Buccigano J, Abraham D W, Lu Y, Rooks M, Trouilloud P L, Wanner R A, Gallagher W J, 1999  
 "Exchange-biased magnetic tunnel junctions and application to nonvolatile magnetic random access memory (invited)"  
*Journal of Applied Physics* **85**, pp. 5828–5833, doi: [10.1063/1.369932](https://doi.org/10.1063/1.369932)
- Parkin S S P, Hayashi M, Thomas L, 2008  
 "Magnetic domain-wall racetrack memory"  
*Science* **320**, pp. 190–194, doi: [10.1126/science.1145799](https://doi.org/10.1126/science.1145799)
- Passeri D, Dong C, Angeloni L, Pantanella F, Natalizi T, Berlutti F, Marianetti C, Ciccarello F, Rossi M, 2014  
 "Thickness measurement of soft thin films on periodically patterned magnetic substrates by phase difference magnetic force microscopy"  
*Ultramicroscopy* **136**, pp. 96–106, doi: [10.1016/j.ultramic.2013.08.001](https://doi.org/10.1016/j.ultramic.2013.08.001)
- Pei W L, Qin G W, Ren Y P, Li S, Wang T, Hasegawa H, Ishio S, Yamane H, 2011  
 "Incoherent magnetization reversal in co-pt nanodots investigated by magnetic force microscopy"  
*Acta Mater.* **59**, pp. 4818–4824, doi: [10.1016/j.actamat.2011.04.024](https://doi.org/10.1016/j.actamat.2011.04.024)
- Pelesko J, 2007  
*Self Assembly: The Science of Things That Put Themselves Together*,  
 Chapman & Hall / CRC Press.

- Pelrine R E, 2004  
“Diamagnetic levitation”  
*Amer. Sci.* **92**, pp. 428–435
- Pfau B, Günther C M, Guehrs E, Hauet T, Yang H, Vinh L, Xu X, Yaney D, Rick R, Eisebitt S, Hellwig O, 2011  
“Origin of magnetic switching field distribution in bit patterned media based on pre-patterned substrates”  
*Applied Physics Letters* **99**, doi: [10.1063/1.3623488](https://doi.org/10.1063/1.3623488)
- Pfau B, Günther C M, Guehrs E, Hauet T, Hennen T, Eisebitt S, Hellwig O, 2014  
“Influence of stray fields on the switching-field distribution for bit-patterned media based on pre-patterned substrates”  
*Applied Physics Letters* **105**, doi: [10.1063/1.4896982](https://doi.org/10.1063/1.4896982)
- Piramanayagam S N, Ranjbar M, Sbiaa R, A T K G, Chong T C, 2012  
“Characterization of high-density bit-patterned media using ultra-high resolution magnetic force microscopy”  
*Phys. Status Solidi RRL* **6**, pp. 141–143, doi: [10.1002/pssr.201105537](https://doi.org/10.1002/pssr.201105537)
- Porthun S, Abelmann L, Lodder C, 1998  
“Magnetic force microscopy of thin film media for high density magnetic recording”  
*Journal of Magnetism and Magnetic Materials* **182**, pp. 238–273
- Proksch R, Kalinin S V, 2010  
“Energy dissipation measurements in frequency-modulated scanning probe microscopy”  
*Nanotechnology* **21**, doi: [10.1088/0957-4484/21/45/455705](https://doi.org/10.1088/0957-4484/21/45/455705)
- Proksch R, Babcock K, Cleveland J, 1999  
“Magnetic dissipation microscopy in ambient conditions”  
*Applied Physics Letters* **74**, pp. 419–421
- Raşa M, Kuipers B W M, Philipse A P, 2002  
“Atomic force microscopy and magnetic force microscopy study of model colloids”  
*Journal of Colloid and Interface Science* **250**, pp. 303–315, doi: [10.1006/jcis.2002.8345](https://doi.org/10.1006/jcis.2002.8345)
- Rastei M V, Abes M, Bucher J P, Dinia A, Pierron-Bohnes V, 2006  
“Field-dependent behavior of a magnetic force microscopy tip probed by means of high coercive nanomagnets”  
*Journal of Applied Physics* **99**, doi: [10.1063/1.2193169](https://doi.org/10.1063/1.2193169)
- Ravaud R, Lemarquand G, Babic S, Lemarquand V, Akyel C, September 2010  
“Cylindrical magnets and coils: Fields, forces, and inductances”  
*IEEE Transactions on Magnetics* **46**, pp. 3585–3590, doi: [10.1109/TMAG.2010.2049026](https://doi.org/10.1109/TMAG.2010.2049026)
- Rawlings C, Durkan C, 2013  
“The inverse problem in magnetic force microscopy - inferring sample magnetization from MFM images”  
*Nanotechnology* **24**, doi: [10.1088/0957-4484/24/30/305705](https://doi.org/10.1088/0957-4484/24/30/305705)
- Richter H J, Dobin A Y, Lynch R T, Weller D, Brockie R M, Heinonen O, Gao K Z, Xue J, Veerdonk R J M V D, Asselin P, Erden M F, 2006  
“Recording potential of bit-patterned media”  
*Appl. Phys. Lett.* **88**, doi: [10.1063/1.2209179](https://doi.org/10.1063/1.2209179)
- Rycenga M, McLellan J M, Xia Y, 2008  
“Controlling the assembly of silver nanocubes through selective functionalization of their faces”  
*Advanced Materials* **20**, pp. 2416–2420, doi: [10.1002/adma.200800360](https://doi.org/10.1002/adma.200800360)

- Sader J E, 1998  
 "Frequency response of cantilever beams immersed in viscous fluids with applications to the atomic force microscope"  
*Journal of Applied Physics* **84**, pp. 64–76
- Sader J E, Jarvis S P, 2004  
 "Accurate formulas for interaction force and energy in frequency modulation force spectroscopy"  
*Applied Physics Letters* **84**, pp. 1801–1803
- Sader J E, Chon J W M, Mulvaney P, 1999  
 "Calibration of rectangular atomic force microscope cantilevers"  
*Rev. Sci. Instrum.* **70**, pp. 3967–3969
- Sader J E, Uchihashi T, Higgins M J, Farrell A, Nakayama Y, Jarvis S P, 2005  
 "Quantitative force measurements using frequency modulation atomic force microscopy - theoretical foundations"  
*Nanotechnology* **16**, pp. S94–S101, doi: [10.1088/0957-4484/16/3/018](https://doi.org/10.1088/0957-4484/16/3/018)
- Saharan L, Morrison C, Miles J J, Thomson T, Schrefl T, Hrkac G, 2011  
 "Angle dependence of the switching field of recording media at finite temperatures"  
*Journal of Applied Physics* **110**, doi: [10.1063/1.3662919](https://doi.org/10.1063/1.3662919)
- Saint Jean M, Hudlet S, Guthmann C, Berger J, 1999  
 "Van der waals and capacitive forces in atomic force microscopies"  
*Journal of Applied Physics* **86**, pp. 5245–5248
- Saito H, Chen J, Ishio S, 1999  
 "Principle of magnetic field analysis by MFM signal transformation and its application to magnetic recording media"  
*IEEE Transactions on Magnetics* **35**, pp. 3992–3994, doi: [10.1109/20.800732](https://doi.org/10.1109/20.800732)
- Schäffer T E, Radmacher M, Proksch R, 2003  
 "Magnetic force gradient mapping"  
*Journal of Applied Physics* **94**, pp. 6525–6532, doi: [10.1063/1.1623926](https://doi.org/10.1063/1.1623926)
- Schumacher F, 1991  
 "On the modification of the Kondorsky function"  
*J. Appl. Phys.* **70**, p. 3184, doi: [10.1063/1.349301](https://doi.org/10.1063/1.349301)
- Shao X, Alink L, Groenland J P J, Abelmann L, Slump C H, October 2011  
 "A simple two-dimensional coding scheme for bit patterned media"  
*IEEE transactions on magnetics* **47**, pp. 2559–2562, doi: [10.1109/TMAG.2011.2157668](https://doi.org/10.1109/TMAG.2011.2157668)
- Shaw J M, Russek S E, Thomson T, Donahue M J, Terris B D, Hellwig O, Dobisz E, Schneider M L, 2008  
 "Reversal mechanisms in perpendicularly magnetized nanostructures"  
*Phys. Rev. B* **78**, pp. 024414–1–5, doi: [10.1103/PhysRevB.78.024414](https://doi.org/10.1103/PhysRevB.78.024414)
- Shaw J M, Olsen M, Lau J W, Schneider M L, Silva T J, Hellwig O, Dobisz E, Terris B D, 2010  
 "Intrinsic defects in perpendicularly magnetized multilayer thin films and nanostructures"  
*Physical Review B: Condensed Matter and Materials Physics* **82**, doi: [10.1103/PhysRevB.82.144437](https://doi.org/10.1103/PhysRevB.82.144437)
- Shetye S, Eskinazi I, Arnold D, 2008  
 "Self-assembly of millimeter-scale components using integrated micromagnets"  
*IEEE Transactions on Magnetics* **44**, pp. 4293–4296, doi: [10.1109/TMAG.2008.2001344](https://doi.org/10.1109/TMAG.2008.2001344)

- Singh G, Chan H, Baskin A, Gelman E, Repnin N, Král P, Klajn R, 2014  
“Self-assembly of magnetite nanocubes into helical superstructures”  
*Science* **345**, p. 1149
- Spencer A, Howson R, 1986  
“The properties of magnetron sputtered CoNi thin films”  
*Vacuum* **36**, pp. 103–105, doi: [10.1016/0042-207X\(86\)90280-0](https://doi.org/10.1016/0042-207X(86)90280-0)
- Springer F, Hellwig O, Dobisz E, Albrecht M, Grobis M, 2011  
“Probing the time-dependent switching probability of individual patterned magnetic islands”  
*Journal of Applied Physics* **109**, doi: [10.1063/1.3540574](https://doi.org/10.1063/1.3540574)
- Stamps R L, Breitkreutz S, Åkerman J, Chumak A V, Otani Y, Bauer G E W, Thiele J U, Bowen M, Majetich S A, Käui M, Prejbeanu I L, Dieny B, Dempsey N M, Hillebrands B, 2014  
“The 2014 magnetism roadmap”  
*J. Phys. D: Appl. Phys.* **47**, doi: [10.1088/0022-3727/47/33/333001](https://doi.org/10.1088/0022-3727/47/33/333001)
- Stoner E, Wohlfarth E, 1991  
“A mechanism of magnetic hysteresis in heterogeneous alloys”  
*IEEE Transactions on Magnetics* **27**, pp. 3475–3518, doi: [10.1109/TMAG.1991.1183750](https://doi.org/10.1109/TMAG.1991.1183750)
- Stoner E C, Wohlfarth E P, May 1948  
“A mechanism of magnetic hysteresis in heterogeneous alloys”  
*Philos. Trans. R. Soc. London A* **240**, pp. 599–642, doi: [10.1098/rsta.1948.0007](https://doi.org/10.1098/rsta.1948.0007)
- Subramaniam A, Yang D, Yu H D, Nemiroski A, Tricard S, Ellerbee A, Soh S, Whitesides G, 2014  
“Noncontact orientation of objects in three-dimensional space using magnetic levitation”  
*Proceedings of the National Academy of Sciences of the United States of America* **111**, pp. 12980–12985, doi: [10.1073/pnas.1408705111](https://doi.org/10.1073/pnas.1408705111)
- Sweetman A, Stannard A, 2014  
“Uncertainties in forces extracted from non-contact atomic force microscopy measurements by fitting of long-range background forces”  
*Beilstein Journal of Nanotechnology* **5**, pp. 386–393, doi: [10.3762/bjnano.5.45](https://doi.org/10.3762/bjnano.5.45)
- Sze S M, Ng K K, 2007  
*Physics of semiconductor devices*,  
John Wiley, Hoboken (NJ), USA, 3rd edition
- Takekuma I, Haseyama M, Sueoka K, Mukasa K, 2002  
“Two-dimensional analysis of magnetic microstructures in the DC-demagnetized state and magnetization fluctuations in the transition region using MFM images”  
*Journal of Magnetism and Magnetic Materials* **239**, pp. 359–362, doi: [10.1016/S0304-8853\(01\)00589-3](https://doi.org/10.1016/S0304-8853(01)00589-3)
- Teo K K, Chan K S, Wong W E, Nov 2009  
“Automated 2-D scanning setup on spinstand for evaluation of ultra-high-density recording data”  
*IEEE Transactions on Magnetics* **45**, pp. 5100–5103, doi: [10.1109/TMAG.2009.2029627](https://doi.org/10.1109/TMAG.2009.2029627)
- Terris B D, Thomson T, 2005  
“Nanofabricated and self-assembled magnetic structures as data storage media”  
*J. Phys. D: Appl. Phys.* **38**, pp. R199–R222, doi: [10.1088/0022-3727/38/12/R01](https://doi.org/10.1088/0022-3727/38/12/R01)
- Thiyagarajah N, Asbahi M, Wong R T J, Low K W M, Yakovlev N L, Yang J K W, Ng V, 2014  
“A facile approach for screening isolated nanomagnetic behavior for bit-patterned media”  
*Nanotechnology* **25**, doi: [10.1088/0957-4484/25/22/225203](https://doi.org/10.1088/0957-4484/25/22/225203)

- Thomson T, Hu G, Terris B D, 2006  
 “Intrinsic distribution of magnetic anisotropy in thin films probed by patterned nanostructures”  
*Phys. Rev. Lett.* **96**, p. 257204, doi: [10.1103/PhysRevLett.96.257204](https://doi.org/10.1103/PhysRevLett.96.257204)
- Thomson T, Abelmann L, Groenland J P J, 2007  
 “Magnetic data storage: past, present and future”  
 In: B Azzerboni, G Asti, L Pareti, M Ghidini, editors, *Magnetic Nanostructures in Modern Technology*, NATO Science for Peace and Security Series Subseries: NATO Science for Peace and Security Series B: Physics and Biophysics, pp. 237–306, Springer Verlag, Berlin
- Tkachenko A, Lu J Q, 2015  
 “Directed self-assembly of mesoscopic electronic components into sparse arrays with controlled orientation using diamagnetic levitation”  
*Journal of Magnetism and Magnetic Materials* **385**, pp. 286–291, doi: [10.1016/j.jmmm.2015.03.022](https://doi.org/10.1016/j.jmmm.2015.03.022)
- Tomlinson S L, Farley A N, 1997  
 “Micromagnetic model for magnetic force microscopy tips”  
*Journal of Applied Physics* **81**, pp. 5029–5031
- Tomlinson S L, Hoon S R, Farley A N, Valera M S, 1995  
 “Flux closure in magnetic force microscope tips”  
*IEEE Transactions on Magnetics* **31**, pp. 3352–3354, doi: [10.1109/20.490379](https://doi.org/10.1109/20.490379)
- Trawick M L, Megens M, Harrison C, Angelescu D E, Vega D A, Chaikin P M, Register R A, Adamson D H, 2003  
 “Correction for piezoelectric creep in scanning probe microscopy images using polynomial mapping”  
*Scanning* **25**, pp. 25–33, doi: [10.1002/sca.4950250106](https://doi.org/10.1002/sca.4950250106)
- Tudosa I, Lubarda M V, Chan K T, Escobar M A, Lomakin V, Fullerton E E, 2012  
 “Thermal stability of patterned co/pd nanodot arrays”  
*Applied Physics Letters* **100**, doi: [10.1063/1.3692574](https://doi.org/10.1063/1.3692574)
- Uesaka Y, Nakatani Y, Hayashi N, 1995  
 “Switching of single hexagonal particles with nonuniform magnetic properties”  
*Jpn. J. Appl. Phys.* **34**, pp. 6056–6062, doi: [10.1109/20.364584](https://doi.org/10.1109/20.364584)
- Uesaka Y, Endo H, Suzuki Y, Nakatani Y, Hayashi N, Fukushima H, 2012  
 “Switching of a particle in inhomogeneous applied field”  
*Journal of Magnetism and Magnetic Materials* **324**, pp. 1272–1276, doi: [10.1016/j.jmmm.2011.07.061](https://doi.org/10.1016/j.jmmm.2011.07.061)
- Van Schendel P J A, Hug H J, Stiefel B, Martin S, Güntherodt H J, 2000  
 “A method for the calibration of magnetic force microscopy tips”  
*Journal of Applied Physics* **88**, pp. 435–445
- Vellekoop B, Abelmann L, Porthun S, Lodder C, 1998  
 “On the determination of the internal magnetic structure by magnetic force microscopy”  
*Journal of Magnetism and Magnetic Materials* **190**, pp. 148–151
- Vellekoop S J L, Abelmann L, Porthun S, Lodder J C, Miles J J, 1999  
 “Calculation of playback signals from MFM images using transfer functions”  
*Journal of Magnetism and Magnetic Materials* **193**, pp. 474–478
- Vlasov Y, Bo X, Sturm J C, Norris D J, 2001  
 “On-chip natural assembly of silicon photonic bandgap crystals”  
*Nature* **414**, pp. 289–293

- Vock S, Sasvári Z, Bran C, Rhein F, Wolff U, Kiselev N S, Bogdanov A N, Schultz L, Hellwig O, Neu V, 2011  
“Quantitative magnetic force microscopy study of the diameter evolution of bubble domains in a (Co/Pd)<sub>80</sub> multilayer”  
*IEEE Transactions on Magnetics* **47**, pp. 2352–2355, doi: [10.1109/TMAG.2011.2155630](https://doi.org/10.1109/TMAG.2011.2155630)
- Vokoun D, Beleggia M, Heller L, Sittner P, 2009  
“Magnetostatic interactions and forces between cylindrical permanent magnets”  
*Journal of Magnetism and Magnetic Materials* **321**, pp. 3758 – 3763, doi:  
DOI:[10.1016/j.jmmm.2009.07.030](https://doi.org/10.1016/j.jmmm.2009.07.030)
- de Vries J, Bolhuis T, Abelmann L, 2013  
“Energy barrier versus switching field for patterned Co<sub>80</sub>Pt<sub>20</sub> alloy and Co/Pt multilayer films”  
*J. Appl. Phys.* **113**, p. 17B910, doi: [10.1063/1.4801399](https://doi.org/10.1063/1.4801399)
- Wallace R L, 1951  
“The reproduction of magnetically recorded signals”  
*Bell System Technical Journal* **30**, pp. 1145–1173, doi: [10.1002/j.1538-7305.1951.tb03699.x](https://doi.org/10.1002/j.1538-7305.1951.tb03699.x)
- Wan H, Hadjipanayis G C, 1991  
“Thickness dependence of coercivity in Co-Ni thin films”  
*Journal of Applied Physics* **70**, pp. 6059–6061, doi: [10.1063/1.350045](https://doi.org/10.1063/1.350045)
- Weibull W, 1951  
“A statistical distribution function of applicability”  
*Journal of Applied Mechanics* **18**, pp. 293–297
- Weis T, Krug I, Engel D, Ehresmann A, Höink V, Schmalhorst J, Reiss G, 2008  
“Characterization of magnetic force microscopy probe tip remagnetization for measurements in external in-plane magnetic fields”  
*Journal of Applied Physics* **104**, doi: [10.1063/1.3040025](https://doi.org/10.1063/1.3040025)
- Whangbo M H, Bar G, Brandsch R, 1998  
“Description of phase imaging in tapping mode atomic force microscopy by harmonic approximation”  
*Surf. Sci.* **411**, pp. L794–L801
- White R L, 1997  
“Patterned media: a viable route to 50 gbit/in<sup>2</sup> and up for magnetic recording?”  
*IEEE Trans. Magn.* **33**, pp. 990–995, doi: [10.1109/20.560144](https://doi.org/10.1109/20.560144)
- Whitesides G M, Grzybowski B, 2002  
“Self-assembly at all scales”  
*Science* **295**, pp. 2418–2421, doi: [10.1126/science.1070821](https://doi.org/10.1126/science.1070821)
- Wilson E B, 1927  
“Probable inference, the law of succession, and statistical inference”  
*Journal of the American Statistical Association* **22**, pp. 209–212, doi: [10.2307/2276774](https://doi.org/10.2307/2276774)
- Wilton D R, Rao S M, Glisson A W, Schaubert D H, Al-Bundak O M, Butler C M, 1984  
“Potential integrals for uniform and linear source distribution on polygonal and polyhedral domains”  
*IEEE Transactions on Antennas and Propagation* **AP-32**, pp. 276–281
- Winkleman A, Perez-Castillejos R, Gudiksen K L, Phillips S T, Prentiss M, Whitesides G M, 2007  
“Density-based diamagnetic separation: Devices for detecting binding events and for collecting unlabeled diamagnetic particles in paramagnetic solutions”  
*Analytical Chemistry* **79**, pp. 6542–6550, doi: [10.1021/ac070500b](https://doi.org/10.1021/ac070500b)

- Woldering L, Abelmann L, Elwenspoek M, 2011  
 "Predicted photonic band gaps in diamond-lattice crystals built from silicon truncated tetrahedrons"  
*Journal of Applied Physics* **110**, doi: [10.1063/1.3624604](https://doi.org/10.1063/1.3624604)
- Woldering L A, Been A, Alink L, Abelmann L, 2014  
 "Diamagnetic levitation and 3D self-assembly of silicon macrocubes in a paramagnetic fluid"  
*Intermag 2014 Digest Book* pp. 3164–3165
- Woldering L A, Been A J, Alink L, Abelmann L, 2015  
 "Using magnetic levitation for 2d and 3d self-assembly of cubic silicon macroparticles"  
*Physica status solidi RRL online pre-publication*, doi: [10.1002/pssr.201510298](https://doi.org/10.1002/pssr.201510298)
- Woldering L A, Been A J, Alink L, Abelmann L, 2016  
 "Using magnetic levitation for 2D and 3D self-assembly of cubic silicon macroparticles"  
*Physica status solidi RRL* **10**, pp. 176–184, doi: [10.1002/pssr.201510298](https://doi.org/10.1002/pssr.201510298)
- Wood R, Williams M, Kavcic A, Miles J, 2009  
 "The feasibility of magnetic recording at 10 terabits per square inch on conventional media"  
*IEEE Trans. Magn.* **45**, pp. 917–921, doi: [10.1109/TMAG.2008.2010676](https://doi.org/10.1109/TMAG.2008.2010676)
- Wu Z, Cioffi J M, Apr 2001  
 "Low-complexity iterative decoding with decision-aided equalization for magnetic recording channels"  
*Selected Areas in Communications, IEEE Journal on* **19**, pp. 699–708, doi: [10.1109/49.920178](https://doi.org/10.1109/49.920178)
- Yacoot A, Koenders L, 2008  
 "Aspects of scanning force microscope probes and their effects on dimensional measurement"  
*J. Phys. D: Appl. Phys.* **41**, doi: [10.1088/0022-3727/41/10/103001](https://doi.org/10.1088/0022-3727/41/10/103001)
- Yang Y, Lopez G P, Yellen B B, 2013  
 "Tunable assembly of colloidal crystal alloys using magnetic nanoparticle fluids"  
*ACS Nano* **7**, pp. 2705–2716
- Yongsunthon R, Williams E D, McCoy J, Pego R, Stanishevsky A, Rous P J, 2002  
 "Test of response linearity for magnetic force microscopy data"  
*Journal of Applied Physics* **92**, pp. 1256–1261, doi: [10.1063/1.1489701](https://doi.org/10.1063/1.1489701)
- Yu J, Ahner J, Weller D, 2003  
 "Direct observation of magnetic bit transition and physical grain boundary in perpendicular recording media"  
*Applied Physics Letters* **83**, pp. 4208–4210, doi: [10.1063/1.1627940](https://doi.org/10.1063/1.1627940)
- Yu J, Ahner J, Weller D, 2004  
 "Magnetic force microscopy with work function compensation"  
*Journal of Applied Physics* **96**, pp. 494–497, doi: [10.1063/1.1757029](https://doi.org/10.1063/1.1757029)
- Zhang F, 2005  
 "Block matrix techniques"  
 In: F Zhang, editor, *The Schur complement and its applications, Numerical methods and algorithms*, volume 4, pp. 83–110, Springer US  
 ISBN 978-0-387-24271-2, doi: [10.1007/0-387-24273-2\\_4](https://doi.org/10.1007/0-387-24273-2_4)
- Zhang L, Bain J A, Zhu J G, Abelmann L, Onoue T, 2006  
 "A model of heat transfer in STM-based magnetic recording on CoNi/Pt multilayers"  
*Physica B* **381**, pp. 204–208, doi: [10.1016/j.physb.2006.01.007](https://doi.org/10.1016/j.physb.2006.01.007)

- Zhong H, Peng W, Tarrach G, Drechsler A, Jiang J, Wei D, Yuan J, 2008  
“Non-contact magnetic force microscopy of recording media by ex situ tip magnetization reversal method”  
*Journal of Physics D: Applied Physics* **41**, doi: [10.1088/0022-3727/41/8/085002](https://doi.org/10.1088/0022-3727/41/8/085002)
- Zhou L, McVitie S, Chapman J N, 1995  
“Magnetic imaging of magnetic force microscope tips”  
*Journal of Magnetism and Magnetic Materials* **148**, pp. 237–238, doi: [10.1016/0304-8853\(95\)00220-0](https://doi.org/10.1016/0304-8853(95)00220-0)
- Zhu X, Grütter P, 2003  
“Magnetic force microscopy studies of patterned magnetic structures”  
*IEEE Transactions on Magnetics* **39**, pp. 3420–3425, doi: [10.1109/TMAG.2003.816170](https://doi.org/10.1109/TMAG.2003.816170)
- Zhu X, Grütter P, Metlushko V, Ilic B, 2002  
“Systematic study of magnetic tip induced magnetization reversal of e-beam patterned permalloy particles”  
*Journal of Applied Physics* **91**, pp. 7340–7342, doi: [10.1063/1.1452683](https://doi.org/10.1063/1.1452683)
- Zhu Y, 2005a  
“Magnetic force microscopy”  
In: Y Zhu, editor, *Modern techniques for characterizing magnetic materials*, pp. 411–451, Springer US  
ISBN 978-1-4020-8007-4, doi: [10.1007/0-387-23395-4\\_11](https://doi.org/10.1007/0-387-23395-4_11)
- Zhu Y, 2005b  
*Modern techniques for characterizing magnetic materials*  
Springer ebook collection / Chemistry and Materials Science 2005–2008, Springer US, doi: [10.1007/b101202](https://doi.org/10.1007/b101202)
- Ziegler D, Stemmer A, 2011  
“Force gradient sensitive detection in lift-mode Kelvin probe force microscopy”  
*Nanotechnology* **22**, doi: [10.1088/0957-4484/22/7/075501](https://doi.org/10.1088/0957-4484/22/7/075501)

# Abstract

Magnetostatic interactions manifest themselves via the fields and forces between and within magnetized bodies. On the nanoscale, the interactions involved in reading and writing 2D patterned arrays of islands were investigated by magnetic force microscopy (MFM), and by modeling and simulations. Such 2D arrays are prototypes for future hard disk drive (HDD) media. On the millimeter scale, interactions were investigated that bind and drive the self-assembly of 2D and 3D arrays. This macro scale self-assembly is aimed at the fabrication of future, 3D, electronics.

The 2D island arrays were patterned out of thin (1.5–6 nm) Co/Pt multilayers with perpendicular anisotropy, by laser interference lithography and (physical and reactive) ion etching. The islands have 70 to 220 nm diameter, and switching fields of  $100 \text{ kA m}^{-1}$  to  $350 \text{ kA m}^{-1}$ .

Due to imperfections in the patterning process, the islands have irregular shapes, which causes media noise in the HDD read back signal. A new model describes the shapes of the islands by their perimeters (chapter 2). The shape fluctuations are modeled by the power spectrum of the Fourier components that describe the island perimeters. Perimeters have been detected in a scanning electron micrograph. A theoretical analysis shows that the shape fluctuation cause distributions in the magnitude and the position of the read back pulses of the islands. The distributions are correlated. As a result, at high areal densities, media noise is not modeled accurately by independent position and size fluctuations.

Besides media noise, 2D inter symbol interference (ISI) inhibits the correct detection of bits. Chapter 3 presents a simple modulation code that avoids the worst case interference patterns at the cost of a 5/6 code rate. The code is tested in simulations on an MFM based channel. The code handles 8.5 % more position jitter than the uncoded case at an acceptable  $10^{-4}$  bit error rate.

In-field MFM was used to determine the remanent switching fields of the 70 nm islands (chapter 5). The angle dependence of the switching fields gives insight into the reversal mechanism of the islands. The identically patterned islands exhibit a distribution in reversal mechanism. The reversal mechanism of weak, easily switching islands is dominated by domain wall propagation, however, the reversal mechanism becomes more coherent rotation-like for increasingly stronger, harder to switch, islands.

Ideally, an MFM senses the vertical gradient in the magnetic force between tip and sample. The force gradients are however corrupted by topographic cross-talk. Chapter 4 discusses their offline corrections. A deconvolution method removes the non-magnetic force gradients. The correction for the scan height variations, due to the MFM liftmode operation, exploits the mathematical relation of the vertical propagation of the magnetic field. The corrections reduce the discrepancy between MFM images acquired in different modes, compared to the case that neglects scan height variations.

The thickness of the magnetic coating on the MFM tip affects the strength of the interactions. The interactions of MFM tips with 35 to 80 nm side-coatings were determined by imaging patterned arrays (chapter 6). Simulations using an approximate tip model explain the experimental read and write interaction qualitatively. Comparing to switching field distributions acquired in uniform fields, the tips have in-contact fields up to  $200 \text{ kA m}^{-1}$ . Some of the 80 nm tips are however irreversibly modified by the islands, which limits the range of practical coating thicknesses. In non-contact, field assisted write experiments the tip field is in effect uniform. The strength of the field is however smaller than the width of the switching field distribution.

Concerning macro scale self-assembly, small assemblies of 3–4 spherical particles equipped with dipole moments were investigated (chapter 7). Like millimeter sized neodymium magnets, such dipolar spherical particles prefer to assemble in 2D configurations. Their behavior has been confirmed by simulating the magnetostatic energy of particle trajectories. According to simulations, particles with indentations that allow for a smaller separation between particles, could lead to a 3D configuration of four dipoles that is energetically favorable over 2D configurations.

In chapter 8, the self-assembly of 3D and 2D arrays is investigated. Cubical, diamagnetic, 0.5 mm-sized Si particles are magnetically levitated in a paramagnetic fluid. Due to a field gradient and external agitation, the particles form clusters approaching the ordered structure of an array. The assembled arrays have a higher quality when the hydrophilicity of the particles is reduced. Moreover, when the bottom of the liquid container is used as a template, the alignment between particles improves. Calculations confirm that the particles indeed minimize the magnetostatic energy in a self-assembly experiment.

# Samenvatting

Dit proefschrift gaat over magnetostatische interacties in geordende 2D en 3D rijstructuren (arrays). Arrays komen van pas in elektronische geheugens, zoals harde schijven, waarin gegevens (enen en nullen) worden onthouden door ze te schrijven op vaste locaties waar ze later teruggevonden en uitgelezen kunnen worden. De wisselwerking tussen magnetische objecten is het resultaat van magnetische velden en de krachten die ze op elkaar uitoefenen. De krachten zetten de magneten in beweging, of beïnvloeden hun magnetisatie.

Op nanometerschaal zijn de interacties die gebruikt worden bij het lezen en schrijven van een nieuw soort opslagmedium voor harde schijven onderzocht met een microscoop die magnetische krachten meet ("magnetic force microscope", MFM). De prototype opslagmedia bestaan uit 2D arrays van magnetische eilandjes met een 70–220 nm diameter. De eilandjes zijn geëtst uit een multilaag van afwisselend kobalt en platina. De multilaag zorgt ervoor dat de eilandjes een loodrechte magnetisatie hebben, óf omhoog óf naar beneden gericht.

Op millimeterschaal zijn de magnetostatische interacties onderzocht die deeltjes bijeen drijven en die deeltjes aan elkaar binden, gericht op self-assembly in grote schaalmodellen. Self-assembly is een proces waarin losse deeltjes vanzelf een functionele structuur vormen, bepaald door de specifieke eigenschappen van de deeltjes (zoals bijvoorbeeld vorm en magnetisatie) en hun omgeving. Het uiteindelijke doel is de microfabricage van 3D elektronica.

**Hoofdstuk 2** Ruis in het leessignaal kan er voor zorgen dat bits fout gedetecteerd worden. Een deel van de ruis ontstaat doordat elk eiland een net iets andere vorm heeft (het lithografie- en het etsproces zijn immers niet perfect) waardoor hun signaal (leespuls) varieert. De fluctuatie in de vorm van de eilandjes is in model gebracht door hun rand wiskundig te beschrijven. De golvende afwijking die de rand heeft ten opzichte van een ideale, perfect cirkel kan gezien worden als een som van sinussen (Fourier componenten). De intensiteit van de Fourier componenten is statistisch bepaald door randen van eilandjes te detecteren in een afbeelding die is gemaakt met een elektronen microscoop. Omdat de randen geleidelijk varieëren zijn er maar een paar deze componenten nodig. Volgens het model veroorzaken de vormfluctuaties variaties in de grootte (van het oppervlak) en het (massa-)middelpunt van de eilandjes. Deze

variaties zijn gekoppeld aan de amplitude en respectievelijk de positie van de leespulsjes van de eilanden. Bovendien zijn de variaties gecorreleerd: eilanden met een groot oppervlak hebben waarschijnlijk ook een grote verschuiving van hun middelpunt. Voor de gemeten array is dit effect klein, maar dit kan significant worden voor arrays met kleinere eilanden.

**Hoofdstuk 3** Het leessignaal is idealiter een reeks van duidelijk gescheiden positieve of negatieve leespulsen (enen en nullen). Echter, als de bits erg dicht op elkaar staan, pikt de leeskop ook signaal op van naastgelegen bits. Vooral de interferentie door de bits in naastgelegen tracks levert makkelijk leesfouten op. Dit komt doordat het nu nog gebruikelijk is om een enkele track (of een stukje ervan) per keer uit te lezen; de leespulsen die de intertrack-interferentie veroorzaken worden zelf niet gedetecteerd. Door de databits te coderen voor dat ze geschreven worden, kan de ergste overspraak worden voorkomen. Een nieuwe 2D codering is getest met behulp van simulaties. De codering zorgt er voor dat de 2D patronen met de grootste interferentie niet voor komen, door op vaste plekken een extra bit toe te voegen. Om 5 bits aan data op te slaan, moeten er wel 6 geschreven worden. De codering kan 8,5 procentpunt meer jitter in bitpositie aan, vergeleken met de situatie zonder codering, waarbij de kans op fouten nog acceptabel is.

**Hoofdstuk 4** Om het leessignaal van de MFM juist te interpreteren moet deze van topografische vervorming worden ontdaan. De vervorming ontstaat doordat de MFM-tip het oppervlak van het sample volgt (op  $\approx 40\text{ nm}$  afstand). Dit oppervlak is niet glad, omdat de eilanden zijn uitgeëetst ( $\approx 15\text{ nm}$  diep). Als de variatie in scanhoogte bekend is, kan het magnetische signaal op een constante hoogte berekend worden. De bewerking lijkt een beetje op het digitaal/achteraf aanpassen van de focus van foto's. Simulaties laten zien dat het zaak is dat de nieuwe, constante hoogte groter is dan hoogte waarop het oorspronkelijke MFM-plaatje genomen is, anders neemt de ruis toe. Daarnaast verstoren niet-magnetische krachten het leessignaal. Dit zijn bijvoorbeeld elektrische krachten. Die zijn van nature aanwezig, omdat de tip en het sample van verschillend materiaal zijn (silicium en kobalt respectievelijk platina). Door de topografie van het sample kan dit niet helemaal met een tegengestelde spanning weggelegd worden. Het kan wel wegerekend worden door middel van deconvolutie. De correcties zijn getest door MFM-signalen te vergelijken die gemeten zijn in verschillende MFM-modi en op verschillende scanhoogten. Als de variaties in scanhoogte correct worden meegenomen, wordt het verschil tussen gecorrigeerde MFM-signalen half zo klein dan wanneer de variaties in scanhoogte worden verwaarloosd.

**Hoofdstuk 5** Voor het schrijven moeten sterke velden worden aangelegd, zodat de magnetisatie van de eilanden ompoolt. De eilanden schakelen niet allemaal bij hetzelfde veld om. Dit komt waarschijnlijk door defecten in de magne-

tische laag en is gerelateerd aan het specifieke fabricageproces. De schakelvelden zijn gemeten door een array met eilandjes stapsgewijs aan steeds sterkere velden bloot te stellen en tussen de stappen door met de MFM te bepalen welke eilandjes van magnetisatie zijn veranderd. De magnetisatie van  $\approx 100\text{ nm}$  grote eilandjes schakelt niet als een geheel, maar in twee stappen. Eerst klapt er een beginnetje om. Dit domein groeit vervolgens en breidt zich uit tot het hele eiland is omgeschakeld. Dit gebeurt razendsnel (enkele nanoseconden) en is met MFM niet direct waarneembaar. Door het veld onder verschillende hoeken aan te leggen, kan er toch inzicht worden verkregen in de manier waarop de eilandjes hun magnetisatie omdraaien. Verrassend blijkt dat er grote verschillen zijn tussen eilandjes, hoewel ze op identieke wijze gefabriceerd zijn. Bovendien valt er een trend op. Voor eilandjes die bij zwakke velden schakelen (zwakke eilandjes), lijkt het uitbreiden van het domein het schakelveld te bepalen. Hoe sterker het eiland des te bepalender wordt het omklappen van het beginnetje voor het schakelveld van het eiland.

**Hoofdstuk 6** Door de dikte van de magnetische coating van de MFM-tip te variëren kan de sterkte van de interacties worden aangepast. Immers, een dikkere coating heeft een groter magnetisch moment en dus een sterker strooiveld (om mee te schrijven) en ervaart sterkere krachten (voor een duidelijker leessignaal). Tips met een 35 tot 80 nm dikke coating, aangebracht op twee zijkanten van de piramide-vormige tip, zijn onderzocht. Simulaties met een vereenvoudigd tipmodel laten zien dat slechts de uiterste 400 nm van de tip actief is bij het lezen. Wat betreft het strooiveld is het actieve deel mogelijk groter ( $\approx 1\mu\text{m}$ ), afhankelijk van de tip-sample afstand. In experimenten is de sterkte van het leessignaal net als in simulaties proportioneel met de dikte van de tipcoating. De sterkte van de tipvelden is bepaald door MFM-plaatjes te scannen. In deze plaatjes is het aantal eilandjes dat schakelt onder invloed van het tipveld geteld en vergeleken met het aantal eilandjes dat schakelt in velden die zijn aangelegd met een grote elektromagneet. In contact met de eilandjes hebben de tips effectief een sterkte tot  $200\text{ kA m}^{-1}$ . Voor sommige 80 nm tips is echter gebleken dat de magnetisatie niet stabiel is. Dikkere coatings lijken daarom niet bruikbaar. Omdat de statistische verdeling van de schakelvelden typisch breder is dan  $200\text{ kA m}^{-1}$ , is het veld van de MFM-tips niet sterk genoeg om arrays te schrijven.

**Hoofdstuk 7** Wat betreft self-assembly is er met behulp van simulaties onderzocht op welke manier een klein aantal magnetische, bolvormige deeltjes zich aan elkaar bindt. Dit zouden bijvoorbeeld 3D geprinte bolletjes kunnen zijn die een permanente magneet bevatten. Doorgaans vormen zulke deeltjes een 2D configuratie waarin alle deeltjes in een vlak liggen. De magnetostatische energie van het systeem van deeltjes is dan minimaal. Met berekeningen van de energie is bepaald welke configuraties van 3–4 deeltjes stabiel zijn. De gesimuleerde configuraties komen overeen met de stabiele configuraties van magnetische balletjes ('neocubes'). Simulaties laten zien dat door inkepingen

te maken in de bolletjes het mogelijk is dat deeltjes met een magnetisch dipool moment in een 3D configuratie self-assembelen.

**Hoofdstuk 8** De self-assembly van 2D en 3D arrays met 0,5 mm silicium kubusjes is onderzocht met behulp van magnetische levitatie. Silicium is diamagnetisch en wordt afgestoten door een magnetisch veld. In een paramagnetische vloeistof wordt dit effect versterkt en kunnen de deeltjes zweven boven een magneet. Een gradiënt in het magnetisch veld zorgt ervoor dat de deeltjes bij elkaar worden gedreven op de plek waar het veld minimaal is. Door (elektromechanisch) te schudden, kunnen de kubusjes hun plaats vinden en vormen ze een array-structuur. De ordening is niet perfect, maar experimenten laten zien dat de kwaliteit van het array verbeterd door de deeltjes (meer) waterafstotend te maken. Ook lijnen de kubusjes hun vlakken beter uit als de bodem van de vloeistofcontainer wordt gebruikt als ondergrond. Berekeningen laten zien dat de deeltjes door hun beweging inderdaad de magnetostatische energie minimaliseren.

# Dankjewels

Ik heb me gedurende mijn promotietraject door veel mensen laten helpen en motiveren. Die wil ik hier graag bedanken.

Laat me eerst de promotiecommissie bedanken. Theo Rasing, Tom Thomson en Harold Zandvliet, bedankt voor het lezen en opponeren van dit dikke boek. Michel de Jong, bedankt dat je dit na mijn afstuderen nog een keer wilde doen. Prof. Thomson, thank you for your thorough reading and commenting on the concept thesis.

Joël en Kodai, fijn dat jullie mij als paranimf bij wilden staan. Ik kijk uit naar de promotie van Hatakeyama-san. (Is dat ook een klusje voor ons geoefende drietal?)

Hans Groenland is de aanleiding tot dit project en een belangrijke spil waar het gaat om motivatie. Tijdens mijn master legde hij me in een wekelijkse sessie één-op-één uit hoe magnetische recording werkte. Boeiend genoeg om later bij Seagate op stage te willen, om nog meer magneetjes te bestuderen bij de nano-electronics groep en vervolgens om weer als AIO verder te gaan, het liefst waar we gebleven waren. Bedankt Hans, voor het starten en het begeleiden van het project. Fijn dat je er altijd goede zin in had en bedankt voor het *niet opjagen*.

Leon, bedankt dat je mijn promotor wilde zijn en bedankt voor het begeleiden. Ik vind het vooral erg fijn dat je het volhield tot ik er een goed boekje van kon maken. Ik heb veel van je geleerd; veel van je ideeën over AIO-en en onderwijs heb ik, denk ik, gaandeweg overgenomen (of ga ik wellicht nog eens overnemen). Toch zijn het meest memorabel wel de goede uitvalsbases die je regelde voor conferentiebezoek, met Jeroen en de heren van SmartTip, of die uit Saarbrücken, of met z'n allen e.g. naar de MME. Bedankt voor het maple-strooppancakeontbijt, Dresdense knussigheid, en toch maar geen Taipese natto (het zou nog steeds in m'n baard zitten).

Jeroen, fijn dat je me te aller ure bijstond. Natuurlijk ook bedankt voor je mooie samples. Jij, en je SMI-genoten Wabe en Johan, bedankt voor het goede voorbeeld (het thesis template, letterlijk en figuurlijk).

Martin, ik bewonder je monikkenwerk en engelengeduld. Bedankt voor al het meten, het mij leren MFM-en, en het vaak toegeven aan mijn gezeur. Gelukkig zaten er nog een hoop *good-days-for-science* tussen. Ook technici Remco/Pino en Henk hebben bijgedragen aan dit boekje. Thijs met zijn wijs-

heid ende senioriteit. Dankjulliewel. MESA<sup>+</sup>-staf bedankt voor het gebruik van het lab en PIN-groep bedankt voor het opereren van jullie mooie microscoop.

Xiaoying, bedankt voor je uitstapje naar magnetische recording, en de vele discussies. Fijn dat je nog een coding-kooltje uit het vuur wist te slepen. STW en gebruikerscommissie Marco de Vos, IBM en Oleg Zaboronski, en prof. Slump bedankt voor het meedenken. René van de Veerdonk, bedankt voor je adviezen aan de gebruikerscommissie en leuk dat ik je in sunny California na mijn stage weer tegen kon komen.

De TST-groep was een prima plek om te AIO-en. Bedankt Gijs en Miko, en via jullie al mijn MicMec-collega's; het was een plezierige en een leuk gevareerde groep.

Susan bedankt dat je alles hebt geregeld. Karen en Satie deden dat in het begin. Dankjulliewel.

Joël, Antoine, Özlem, Léon en Pele, merci en bedankt voor de fijne kamer, gezelligheid en discussies. Joël bedankt dat je me bij wilde staan in de strijd tegen het kleine kwaad. Léon, fijn dat je me altijd wilde helpen als het AIO-en er om vroeg. Leuk dat je meedurfde op conferentie. Bedankt.

Mathijs, Pieter en Auke bedankt voor het ontwikkelen van macro selfassemblies. Garud, bedankt voor het meerekenen en het toffe Brugge avontuur. Ik ben blij dat ik de krenten uit de pap mocht pikken wat betreft jullie projecten. Per en Tijmen, leuk dat er zowaar een self-assembly experiment is gelukt, en bedankt voor het tellen. Meer filmpjes a.u.b.

Tot slot, ouders Han en Wilma, Wouter en Sanne, Robert en Aafke en gezinnetjes, bedankt voor alles.

# Publications

## Journal articles

Alink L., Groenland J.P.J., De Vries J., Abelmann L., 2012

“Determination of bit patterned media noise based on island perimeter fluctuations”

*IEEE Trans. Magn.* **48**, p. 4574, doi: [10.1109/TMAG.2012.2201138](https://doi.org/10.1109/TMAG.2012.2201138)

Woldering L.A., Been A.J., Alink L., Abelmann L., 2016

“Using magnetic levitation for 2D and 3D self-assembly of cubic silicon macroparticles”

*Physica status solidi RRL* **10**, p. 176, doi: [10.1002/pssr.201510298](https://doi.org/10.1002/pssr.201510298)

Shao X., Alink L., Groenland J.P.J., Abelmann L., Slump C.H., 2011

“A simple two-dimensional coding scheme for bit patterned media”

*IEEE Trans. Magn.* **47**, p. 2559, doi: [10.1109/TMAG.2011.2157668](https://doi.org/10.1109/TMAG.2011.2157668)

Three more publications are in preparation: an article based on chapter 4 on the liftmode correction, an article based on chapter 5 on the switching fields of individual islands, and an article based on chapter 6 on tip-sample interactions. The work in chapter 7 on dipolar self-assembly has been submitted for publication.

## Conference contributions

Alink L., Siekman M.H., Groenland J.P.J., Abelmann L., 4-8 May 2014

“Remarkable difference in switching fields of individual  $D = 70\text{ nm}$  CoPt in a patterned array”

In: *Proc. IEEE International Magnetics Conference*, Dresden, Germany

Alink L., Groenland J.P.J., de Vries J., Abelmann L., 7-11 May 2012

“Determination of bit patterned media noise based on island perimeter fluctuations”

In: *Proc. IEEE International Magnetics Conference*, Vancouver, Canada

Alink L., Shao X., Groenland J.P.J., Abelmann L., 18-19 October 2011

“Two dimensional coding and data detection”

Advanced storage technology consortium, Fall 2011, San Jose, USA

Alink L., Marsman G.H., Woldering L.A., Abelmann L., 19-22 June 2011

“Simulating three dimensional self-assembly of shape modified particles using magnetic dipolar forces”

In: *Proc. Micromechanics and Micro systems Europe*, Tonsberg, Norway

Shao X., Alink L., Groenland J.P.J., Abelmann L., Slump C.H., 25-29 May 2011

“A simple two-dimensional coding scheme for bit patterned media”

In: *Proc. IEEE International Magnetics Conference*, Taipei, Taiwan



